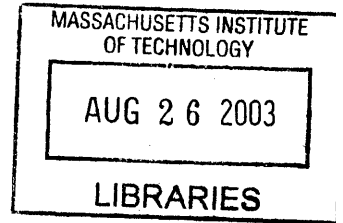# A Three-Dimensional Constitutive Model for the Mechanical Behavior of Cervical Tissue

by

Sébastien Febvay

Ingénieur de l'Ecole Polytechnique
Ecole Polytechnique (2000)

Submitted to the Department of Mechanical Engineering
in partial fulfillment of the requirements for the degree of

Master of Science in Mechanical Engineering

at the

MASSACHUSETTS INSTITUTE OF TECHNOLOGY

June 2003

© Massachusetts Institute of Technology, 2003
All Rights Reserved

The author hereby grants to Massachusetts Institute of Technology
permission to reproduce and
to distribute copies of this thesis document in whole or in part.

Signature of Author ....

Department of Mechanical Engineering
May 10, 2003

Certified by............................

Simona Socrate
Assistant Professor of Mechanical Engineering
Thesis Supervisor

Accepted by ....

Ain A. Sonin
Professor of Mechanical Engineering
Chairman, Department Committee on Graduate Students

A Three-Dimensional Constitutive Model for the Mechanical Behavior of Cervical Tissue

by

Sébastien Febvay

Abstract

The biomechanical integrity of the cervix is critical in maintaining a healthy gestation. In normal pregnancies, the cervix remains firm and closed throughout gestation, while uterine smooth muscle is relaxed. Cervical stroma undergoes substantial restructuring during pregnancy, especially in the final stage nearing delivery, where the balance of the constituent elements of the extracellular matrix (collagen, glycosaminoglycans, elastin, water) is continually evolving. As labor begins (usually near term), the cervix softens and dilates. This "maturation" process occurs over the course of the last week of pregnancy and is a prerequisite for a normal course of labor and delivery. Cervical incompetence is commonly defined as a condition in which gradual, progressive, painless dilation of the cervix leads to spontaneous pregnancy loss between the second and early third trimesters of pregnancy. Despite the introduction of new diagnostic technologies, cervical incompetence continues to be an elusive, often misdiagnosed condition and it remains one of the leading causes of morbidity and mortality in newborn infants. Our aim is to develop a quantitative, biomechanical model that integrates cervical geometry, tissue properties and loading conditions to demonstrate the biomechanical etiology of the premature cervical dilation associated with a diagnosis of cervical incompetence. A critical element of this study is the development of a constitutive model for the cervical tissue. Here we introduce a phenomenological fully three-dimensional constitutive model for the large strain, time dependent mechanical behavior of cervical tissue. The proposed model captures specific aspects of the complex biomechanical response of cervical stroma: it incorporates the ability to account for the contributions of each constituent and for the cooperative nature of the tissue response. In vitro mechanical testing of human cervical samples was performed in several modes of deformation. Finite element simulations were performed using a fully three-dimensional numerical implementation of our model. The model was able to successfully capture the experimentally observed behavior of the tissue in both modes of deformation. Finally, biochemical measurements such as collagen

and glycosaminoglycans content were performed, to enable future correlation between the mechanical constitutive parameters of the model, and the physical parameters of the tissue.

Thesis Supervisor: Simona Socrate
Title: Assistant Professor of Mechanical Engineering

Contents

List of Figures

List of Tables

Acknowledgments

First I would like to thank my advisor Professor Simona Socrate for all the guidance and support she has provided me throughout this project. She has been a tremendous person to work for with her incredible patience and constant enthusiasm. I also want to thank Doctor Michael House, without whom nothing of this project would have been possible.

My gratitude goes to Anastassia Paskaleva and Kristin Myers, who have contributed greatly to this project, especially Kristin who realized a large part of the experimental work presented here. I am also very grateful to Han-Hwa Hung for her patience and kindness in guiding and helping me through the biochemical experiments, Doctor Eliot Frank for his great help in performing the mechanical tests, and Professor Alan Grodzinsky for kindly allowing us to use his facilities.

Also, I want to thank all my friends who have made these past two years at MIT a great time. I cannot list all of you, but I especially wish to mention Thomas Viguier, Hoang-Phong Nguyen, Matteo Salvetti, Franck Billarant, Antoine Guivarch and Dane Miller, with whom great moments were shared. Thank you for all your support and for being such great friends. Without you guys lunch will never be the same. Special mention for Franck who kindly helped me for many of the illustrations.

Finally, my deepest gratitude goes to my family who has constantly supported me throughout all my education, and to whom I owe everything. Thank you for always being there for me.

Chapter 1

Introduction and Clinical Problem

1.1 Introduction

Preterm delivery constitutes the second most important cause of perinatal mortality, after fetal anomalies [1]. Despite substantial research in the field, it remains one of the biggest challenges in obstetrics, as no noticeable reduction in the rate of premature delivery has been achieved in the past 50 years [2]. There is a very broad panel of factors leading to preterm delivery. They can be of very different natures, and among the most common we can mention preterm labor (which corresponds to a premature onset of the uterine contractions normally occurring before delivery), rupture of the fetal membranes, cervical malfunction, bleeding, infection, fetal anomaly or abruptio placentae. Preterm delivery occurs in approximately 10 percent of all pregnancies [2].

Among the most frequent causes of preterm delivery we have cited the existence of a malfunctioning uterine cervix. The cervix acts as the anatomical barrier that retains the fetus inside the uterus during gestation (see Figure 1-1). Its role is dual: it must prevent the conceptus from leaving the uterine cavity during the 40 weeks of gestation, and allow for sufficient dilation during labor to enable delivery. Towards the end of the pregnancy it is subjected to progressive changes in its biochemical composition that cause it to soften, and dilate in response to uterine contractions. Its main function in pregnancy is thus

mechanical in nature, and is of critical importance to a successful outcome.

Cervical dysfunction is one among several factors for preterm delivery. In particular cervical incompetence is a pathological condition in which abnormalities in the cervix functional properties are responsible for preterm delivery in the second trimester of pregnancy. It is characterized by a painless and contraction-free dilation of the cervix in the middle of the second trimester, inevitably leading to the delivery of the baby. It is very often associated to death of the newborn, or irreversible neurological and developmental abnormalities for the infants who survive [3]. This condition is estimated to account for 8% to 15% of all premature deliveries [4], and 20% of all mid-trimester pregnancy losses [5]. However, its real impact is very difficult to estimate, as the diagnosis of this condition is usually very hard to establish for reasons that will be explained, and is typically made when other potential causes have been ruled out.

The etiology of this dysfunction has not yet been clearly established, but cervical incompetences are usually classified in three main categories [6]:

- congenital factors

- physical injury or trauma

- biochemical factors.

In all cases, it is defined by the mechanical inability of the cervix to maintain the fetus inside the uterus until term, leading to spontaneous abortions in the late mid-trimester to early third-trimester of pregnancy.

The aim of the present work is to identify the important factors that take part in the genesis of the pathology, both from a qualitative and quantitative point of view. On account of the mechanical nature of the problem, the study will be realized in the theoretical framework of continuum mechanics. This work is focused on the mechanical behavior of cervical tissue, and is part of a wider project which aims at modeling a large number of critical factors (biochemistry of the cervical tissue, patient-specific anatomical data, constitutive model for the mechanical behavior of the tissue, etc.), and incorporate
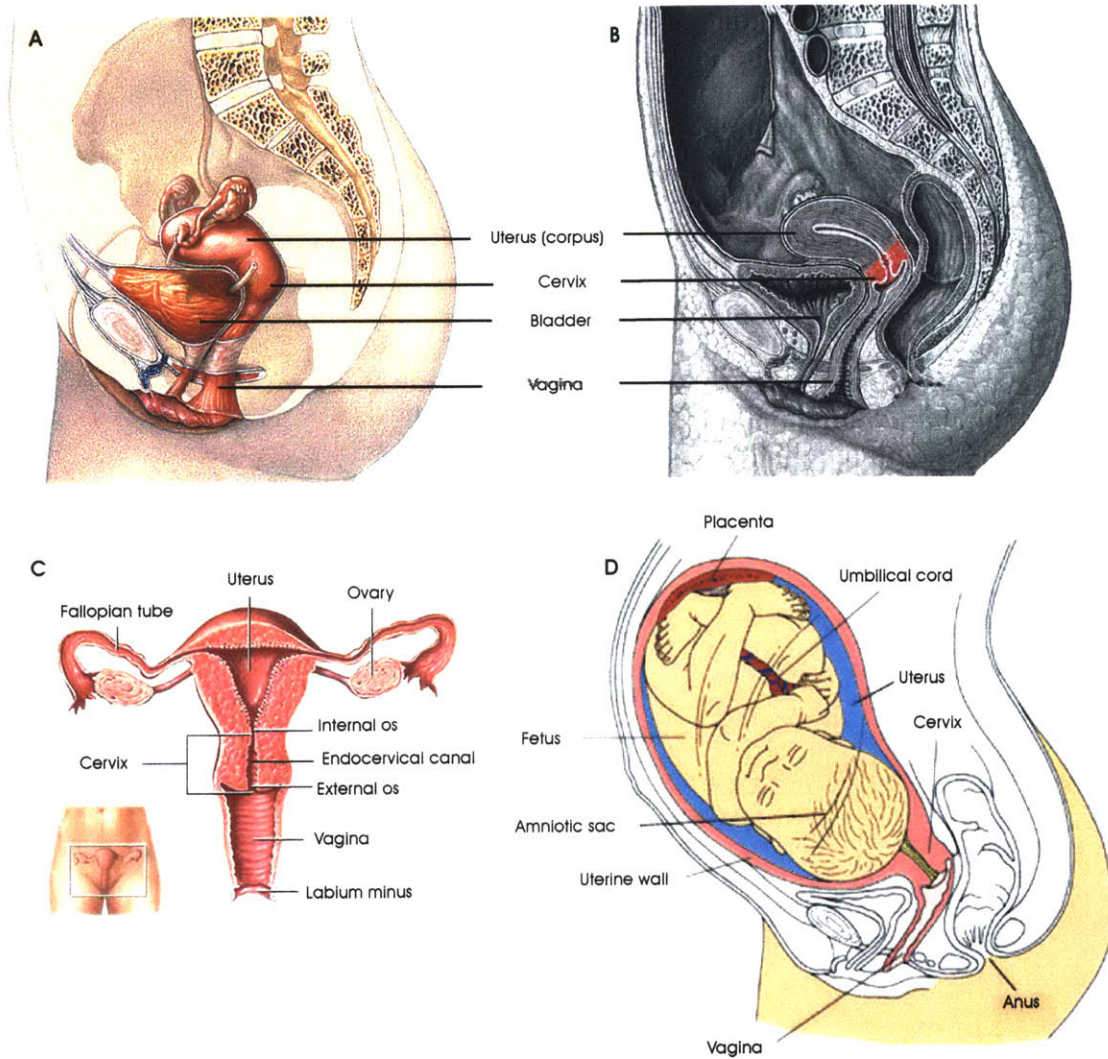
Figure 1-1: Anatomical characteristics of cervix uteri. A. Uterus and surrounding organs. B. Sliced view. C. Female reproductive tract. D. Uterus and cervix in pregnancy. (Modified from www.adam.com).

them in a macroscopic model designed to simulate pregnancy, and bring some insight into the underlying mechanisms of cervical incompetence.

The following sections of this chapter will present more in detail the characteristics of cervical incompetence, the current techniques at hand to establish the diagnosis, and the possible treatments.

1.2 Clinical Definition and Diagnosis of Cervical Incompetence

Cervical incompetence is defined as a "repetitive acute, painless second-trimester evacuation of the uterus without associated bleeding or uterine contraction" [7]. The diagnosis is based on a clinical record of one or more preterm deliveries in the mid-trimester in the absence of other identified causes. This condition is usually very hard to detect in the pregnant patient in the course of a first pregnancy, and there is still some controversy about what criteria exactly define cervical incompetence in such a context. Some specialists agree that a diameter at the internal cervical os superior to 15 mm in the first trimester or 20 mm in the second trimester as measured by transvaginal ultrasonography (see Figure 1-4), or the endocervical canal with a length inferior to 1.5 cm or a diameter larger than 8 mm are sufficient to classify the cervix as incompetent [5]. However, it appears that even under those circumstances most women carry their pregnancy until term. Thus the sensitivity of such factors does not seem to be very high for predicting preterm delivery. Other authors consider that these criteria are not diagnostic of cervical incompetence, and that the only way of establishing the diagnosis in the course of a pregnancy is to actually observe the cervix dilating and the fetal membranes bulging out at the external os [4]. These criteria do not apply to non-pregnant women, and the methods used to establish the diagnosis in those cases include the introduction of Hegar dilators in the cervix, hysterography, the measurement of cervical resistance in response

18

to dilatation, or the use of an intracervical balloon. None of these diagnostic techniques seems to have reached a very high popularity, because they remain inaccurate and still unsubstantiated by large randomized studies ([5], [6]).

It appears that the criteria defining a diagnosis of cervical incompetence are still subject to controversy among the specialists in the field, and it remains extremely difficult to predict cervical incompetence before or during a first pregnancy. The diagnosis is usually based on the clinical obstetric history of the patient, and established after several unexplained spontaneous abortions in the mid-trimester.

Cervical competence has long been considered as an "all or nothing" characteristic, but a recent study [8] suggests the existence of a continuum of cervical competence, and thus incompetence, as measured by cervical length on ultrasonographic images during pregnancy, for women at risk of preterm delivery. In this study, the endocervical canal length was monitored on five groups of pregnant women at different gestational ages by means of transvaginal ultrasonography. The first group was constituted of women diagnosed with cervical incompetence, the second, third and fourth groups were composed of women with a history of a previous preterm delivery before respectively, 26 weeks, 32 weeks, and 35 weeks, while the fifth group was composed of women with prior delivery at term (see Table 1.1).

	Group #1 Incompetent cervix	Group#2 PTD $\leq$ 26	Group#3 $27 \leq$ PTD ≤ 32	Group#4 $33 \leq$ PTD ≤ 35	Group#5 Normal controls
No.	32	98	98	127	106
Age (years)	26.2 $\pm$ 6.2	25.3 $\pm$ 6.3	26.1 $\pm$ 5.5	24.9 $\pm$ 5.4	23.4 $\pm$ 4.7
Parity	1.8 $\pm$ 1.3	1.9 $\pm$ 1.1	2.4 $\pm$ 1.3	2.3 $\pm$ 1.3	0.89 $\pm$ 1.0
Gestational age at first PTD (weeks)	20.9 $\pm$ 2.3	22.9 $\pm$ 2.4	30.0 $\pm$ 1.7	34.2 $\pm$ 0.8	-

Table 1.1: Groups of patients in the study by Iams et al. Mean age, parity and gestational age at the first preterm delivery (PTD) are indicated for each group. Data are expressed as mean $\pm$ 1 SD.

The study demonstrated correlation between the length of the cervix measured during the current pregnancy, and the time of delivery for the previous pregnancy. Shorter cervices corresponded to a higher incidence of previous preterm delivery. These results are

consistent with the existence of a continuum of cervical competence, which in conjunction with other factors controls the outcome of a pregnancy. Thus there does not appear to be a dichotomic state of cervical integrity, the cervix being either fully competent or fully incompetent. For a certain level of cervical integrity, the advanced onset of uterine contractions may be sufficient to induce delivery, causing the cervix to become incompetent, whereas for a more resistant cervix pregnancy might continue until term for the same level of contractions.

A second study by Iams, Goldenberg et al (1996) [9] confirmed these results. 2915 women were examined by transvaginal ultrasonography at approximately 24 weeks gestational age, and 2531 of these patients were examined again at 28 weeks gestation. The gestational age at delivery was recorded for all of them, and spontaneous preterm delivery before 35 weeks was found to correlate with the cervical length measured at 24 and 28 weeks. Shorter cervices were associated with a higher risk for preterm delivery in a continuous fashion, as shown in Figure 1-2. The relative risk of preterm delivery plotted as a function of cervical length appears to follow a progressively decreasing curve, and not a step-like distribution as would be expected in the hypothesis of a cervix being either fully competent or fully incompetent.

This is a very important notion, as it throws light on the multifactorial nature of premature delivery, and in particular cervical incompetence. A wide panel of causes have to be taken into account when trying to predict cervical incompetence, and more generally the outcome of pregnancy:

(i) the mechanical integrity of the cervical tissue;

(ii) the anatomic features of the cervix, such as length, geometry, and the mechanical support provided by the surrounding structures (ligaments, muscles of the pelvic floor);

(iii) the load imposed by the fetus (twins or multiple gestations impose higher loads than singleton gestations).
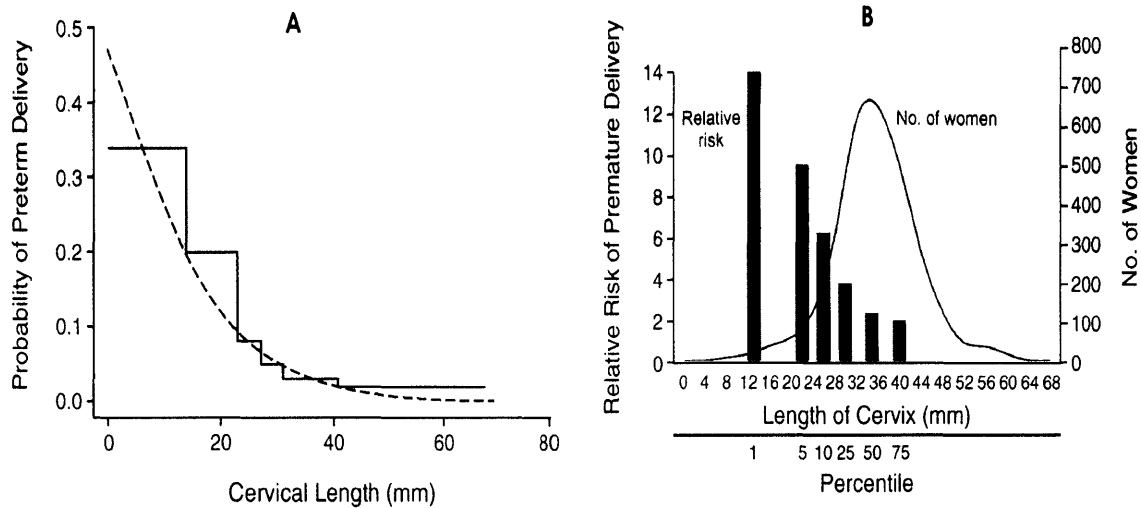
Figure 1-2: A. Estimated probability of preterm delivery before 35 weeks versus cervical length measured by transvaginal ultrasonography at 24 weeks gestation. B. Distribution of subjects among percentiles for cervical length at 24 weeks of gestation and relative risk of spontaneous preterm delivery before 35 weeks according to percentile for cervical length (lower axis). The risk is relative to that for women above the 75th percentile. Reproduced from Iams et al [9].

These findings emphasize the importance of a quantitative model incorporating all these different aspects, to help physicians in the management of patients suspected to be at risk for premature delivery, and especially cervical incompetence. A computer-based model incorporating geometrical and anatomical data from a specific patient, as well as biochemical and mechanical parameters characterizing the cervix, would enable a better identification of the patients who might benefit from different treatment procedures that are available to extend pregnancy. As will be shown in section 1.4, such treatments may be beneficial for only a certain class of patients as they can possibly lead to complications and side effects. A careful selection of the patients to whom they are administered is then necessary.

The next section will focus on identifying the different etiologies, or rather the various factors that come into play in cervical incompetence.

1.3 Etiology of Cervical Incompetence

Multiple factors play a role in cervical incompetence. They can be classified into three main categories:

1. congenital factors,

2. acquired factors such as injury or trauma,

3. biochemical factors.

The different categories will be analyzed in more detail in each of the following subsections.

1.3.1 Congenital Factors

It is clear from the history of numerous patients that cervical incompetence can sometimes be congenital, and sometimes acquired. Indeed a number of patients deliver before term in their first and all subsequent pregnancies, without any history of cervical trauma, whereas others have a history of premature delivery due to cervical dilatation in the second trimester after several previous pregnancies carried until term. The most common congenital causes of cervical incompetence include abnormal Mullerian duct fusion, in utero exposure to diethylstilbestrol, and an inherently short cervix ([6], [10]). Women exposed to diethylstilbestrol (DES) in utero have a high probability of developing cervical and uterine anomalies, that in turn are often the cause of premature delivery.

1.3.2 Acquired Factors

In most cases, cervical incompetence results from acquired factors, mainly cervical lesions. These lesions can be caused by a previous cone biopsy (the risk of subsequent cervical damage being naturally greater with biopsies of increasing size), lacerations, surgical trauma, or previous cervical dilatation as in normal vaginal delivery or procedures of

voluntary abortion. Cervical trauma may also occur in the course of cesarean delivery [10]. Dilatation and curettage performed in cases of spontaneous or induced abortion can also be the source of cervical lesions.

1.3.3 Biochemical Factors

Composition of the Cervical Tissue

Other etiologies have been identified, associated with abnormalities in the biochemical composition of the cervical tissue (see chapter 2 on the biochemical constituents of the cervical stroma). A connection has indeed been established between the risk of preterm delivery and a decreased ratio of collagen to smooth muscle within the cervix. A higher content in smooth muscle and a reduction of collagen content have been showed to increase the risk of preterm delivery [11]. An increased collagenolytic activity in the tissue, responsible for an increase in the collagen turnover associated with a degradation of its elastic properties, has also been demonstrated to be associated with cases of cervical incompetence [12]. In this study, the authors suggested that a high turnover in collagen results in a high proportion of newly synthesized collagen fibers with weak mechanical tensile resistance. Another study by Petersen and Uldbjerg [13] measured the collagen content and extractability of the cervix of non-pregnant woman with a clinical history of cervical incompetence, and no prior cervical trauma. They concluded that cervical incompetence for these patients seemed to be associated with a lower collagen content as measured by hydroxyproline concentration (54.15 $\mu g/mg$ dry tissue vs 72.53 $\mu g/mg$ for normal parous women), as well as a higher extractability in acetic acid and pepsin of the collagen in the non-pregnant state (80.2% vs 49.5%). Finally, a decreased content in cervical elastin has also been suggested as a potential cause of cervical incompetence ([4], [54]).

Hormonal Activity

Some authors also mention abnormal hormonal activity as a possible mechanism for early remodeling and softening of the cervical stroma during pregnancy. Hormonal signals actually trigger remodeling of the cervical tissue in every normal pregnancy just before term, which causes softening of the cervix, and which, accompanied by the development of uterine contractions, causes cervical dilatation and initiates delivery. A precocious hormonal activity might be the critical factor for a class of incompetent cervices. In this case, a condition of cervical incompetence would be impossible to detect outside of pregnancy.

This very broad range of risk factors that contribute to cervical incompetence accounts for its very difficult detection, as it is clear that in most cases a complex association of several of these parameters in various proportions results in the cervical dysfunction. This calls for the establishment of precise criteria leading to a quantification of the risk for cervical incompetence in pregnant women. These criteria can only come from a better understanding of the underlying mechanisms of the pathology, and the importance of the role played by each contributing factor.

Better tools for the clinician to evaluate the risks of preterm delivery due to cervical incompetence would enable better decisions with regards to directions to take in the management of the pregnancy, and in particular whether or not to use a surgical treatment. The different treatment alternatives will be briefly outlined in the next paragraph, followed by a short review of the current tests and criteria at hand to help evaluate cervical competence in pregnancies at risk for preterm delivery.

1.4 Treatments for Cervical Incompetence

Historically, a number of treatments have been proposed to manage cervical incompetence, including medical treatments and surgical procedures, among which one has progressively predominated, and constitutes today the most widely used alternative: cervical

cerclage. Beside surgical procedures, an alternative often prescribed as a preventive measure in high-risk pregnancies is simply bed rest, which is in most cases able to prolong pregnancy by a few days to weeks. The following paragraphs will briefly review the surgical treatment options.

1.4.1   Medical Treatments

Progesterone used to be the most prescribed treatment in cases of cervical incompetence. Progesterone was administered based on studies that suggested it decreases uterine activity [14]. However this treatment has become controversial and it is now widely accepted that progesterone is inappropriate in the treatment of cervical incompetence [5].

1.4.2   Surgical Procedures

In the past 50 years, the major treatment for cervical incompetence has become surgical with the development of a new procedure to keep the cervix closed until term, called cervical cerclage. Cerclage procedures can be executed either transvaginally, or transabdominally. In the latter case, the sutures are permanent and require a subsequent delivery by caesarean section. In transvaginal cerclage, the stitches are removable, and this procedure is much more commonly used than the transabdominal one. There exists two main types of transvaginal cerclage. The first was invented by Shirodkar in 1955 [15], and the second was designed by McDonald in 1957 [16]. They still represent the standard procedures carried out in the management of cervical incompetence nowadays, and the following sections will briefly describe the main features of these two surgical interventions. Then a brief paragraph will be devoted to transabdominal cerclage, and a final section will focus on the rate of success of these different modalities, and their potential complications.

Shirodkar Suture

A small anterior incision is made at the junction between the rugose vagina and the smooth cervix. Then a non absorbable suture is placed under the mucosa, circumferentially, at the level of the internal cervical os [5]. The circumferential suture is knotted, and the vaginal incision is closed with an absorbable suture. The knot can be either anterior or posterior. A posterior knot may be less accessible for removal in certain cases, however an anterior knot needs to be buried submucosally to avoid possible erosion of the bladder, and thus requires dissection to be removed.

The material used to realize the cervical suture can be either a strip of the patient's own fascia lata, as originally performed by Shirodkar, or various other materials such as silk, polyethylene or Mersilene tape, which has now become the standard material.

Mac Donald Suture

This technique involves the placement of a purse-string suture, composed of four bites placed in the cervix as high as possible, roughly at the level of the internal cervical os. The knot is then tied anteriorly to facilitate its removal (Figure 1-3).

The material used for this type of cerclage is most often Mersilene tape. This technique has proved as effective as the Shirodkar technique [10], and presents the advantage to require less dissection. The ease of this procedure tends to make it the method of choice, as it is associated with less potential complications.

Transabdominal Cerclage

In certain cases a permanent suture is placed transabdominally, at the level of the internal cervical os. This method presents more risks though, and requires all subsequent deliveries to be performed via caesarian section. Therefore, it is almost exclusively used after other techniques have failed ([17], [18]). This treatment option can be useful in cases in which transvaginal procedures are not technically possible. Its rate of success in prolonging pregnancy until term proves to be satisfactory, with a low incidence of
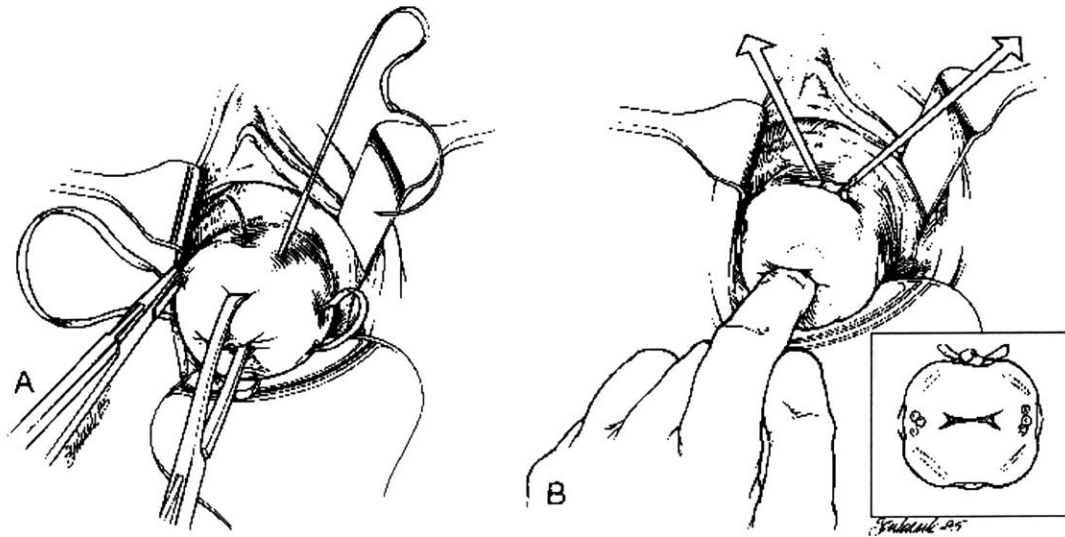
Figure 1-3: Mac Donald suture (from Obstetrics: Normal and Problem Pregnancies, 3rd ed., Churchill Livingstone).

complications for carefully selected patients [19].

The optimal timing for the placement of a cervical cerclage is considered to be around 14 weeks of gestational age [4]. This time is after the first trimester, when spontaneous abortion may occur due to other causes, such as fetus anomalies or bad implantation, for which cervical cerclage would not be appropriate, and early enough so that the procedure can be performed without too many risks of complications.

1.4.3 Success of Cerclage Therapy

Potential Risks and Efficacy of Cervical Cerclage

The most common source of morbidity associated with cervical cerclage is cervical injury at the time of delivery [10]. Fibrous scar tissue may form at the site of the stitch implantation, sometimes leading to an abnormal labor curve. Also such fibrous bands may rupture, or, on the opposite end of the spectrum, never dilate, requiring caesarean section.

Other risks are infection, sometimes leading to chorioamnionitis, hemorrhage, rupture of the membranes, or vaginal discharge [5]. Immediate removal of the suture and delivery are necessary in cases of amniotic fluid leakage, due to the high risk of infection.

Efficacy of Cervical Cerclage

Even half a century after the introduction of cerclage as a treatment for cervical incompetence, it is still not clearly established whether this procedure actually improves the outcome of pregnancy for selected subsets of patients.

It has been emphasized that the success of cerclage procedures strongly depend on the accuracy of the diagnosis of cervical incompetence, and a large part of the failures of this therapy have been attributed to a controversial diagnosis ([20], [21]). Some diagnostic scoring systems to assess cervical competence have been developed, and their performance at detecting women who may receive a cervical cerclage has been assessed. A small study realized in 1989 [22] followed a group of patients who had received Mac Donald cerclage after a diagnosis of cervical incompetence had been established. A specific scoring system was tested in this study (see Table 1.2), and the results revealed that women with a higher score (and thus supposedly a higher degree of cervical incompetence) had less preterm deliveries and neonatal morbidity after the placement of the stitch than the women with a lower score. The qualitative, clinical nature of the proposed criteria emphasize the difficulty of the diagnosis, and of the decision of whether or not a particular patient should receive a cerclage. The scoring system proposed may be helpful in achieving a more careful selection of these patients, but it relies heavily on the clinical history of the patient and strongly suggests the need for more sophisticated and quantitative methods of assessment of cervical competence, especially for women at risk for preterm delivery in their first pregnancy.

The results from several randomized studies have been published recently, and show that the benefits of cerclage therapy strongly depend on the criteria used for patient selection.

28

Criteria	Point Score
(a) Previous premature delivery or mid-trimester abortion without cause	1
(b) Visual evidence of previous surgical or obstetric trauma to the cervix	1
(c) History of painless premature labor or rapid delivery	1
(d) Progressive dilatation or dilatation greater than 2 cm on initial examination during mid-trimester	1
(e) Previous diagnosis of cervical incompetence with previous cerclage	1

Table 1.2: Scoring system for women with suspected cervical incompetence assessed by Ger et al.

A first study conducted in the Netherlands [23] selected 35 patients from three different groups at risk for preterm delivery in the mid-trimester, and randomly assigned half of each group to either cervical cerclage (Mac Donald technique) associated with bed rest, or bed rest only. The patients were included in the three groups according to the following criteria:

- First group: women with a previous preterm delivery before 34 weeks of gestation who met the diagnostic criteria of cervical incompetence (as defined by a progressive and painless dilation of the cervix that would inevitably lead to preterm delivery without treatment), or who had experienced protrusion of the membranes before 32 weeks of gestational age. The women from this group who had a cervical length inferior to 25 mm as measured by transvaginal ultrasonography before 27 weeks of gestation were included in the randomized study.

- Second group: women with one or several commonly accepted risks for cervical incompetence such as uterine anomaly, exposure to DES in utero, or cold knife conization. Only women with a cervical length inferior to 25 mm before 27 weeks of gestation were included in the study, as for the first group.

- Third group: all the patients included in the first two groups had been included before a gestational age of 15 weeks. Women with similar criteria detected after 15

weeks of gestation, as well as women with symptoms of cervical incompetence such as pressure in the lower abdomen or vaginal discharge were included in the study provided they had a cervical length inferior to 25 mm before 27 weeks of gestation.

The cerclages were removed at a mean gestational age of 36.5 ± 0.5 weeks. The study showed a significantly lower rate of preterm delivery in the patients who had received a cerclage compared to the bed rest group. The morbidity was also significantly lower in the cerclage group. There was no preterm delivery before 34 weeks in the cerclage group on a total of 19 patients, and all the infants survived, whereas 7 of the 16 women assigned to the bed rest group had preterm deliveries before 34 weeks, and 3 of the babies died.

This study demonstrates the benefits of cervical cerclage for patients selected based on a clinical history of cervical incompetence or clinical risks for cervical incompetence, combined with ultrasonographic measurements of the cervical length.

However another recent randomized trial to assess the efficacy of cervical cerclage on a certain population of pregnant women led to very different conclusions. In this study conducted between 1998 and 2000 in Pennsylvania [24], 113 pregnant patients were selected based on ultrasonographic data. Patients were included if they had a dilation of the internal os associated with either a prolapse of the membranes through the endocervical canal superior to 25% of the total cervical length, or a distal cervical length of less than 25 mm. The patients were then randomly assigned to receive a Mac Donald cerclage or no cerclage. The management of the patients was the same for both groups before and after the placement of the cerclage.

Cerclage was then considered as an independent variable in the study, and statistical analysis showed no significant correlation between the placement of a cerclage and gestational age at delivery, or neonatal morbidity.

These results emphasize the need for better selection criteria for the patients who might benefit from cerclage therapy. Indeed the ultrasonographic measurements used as inclusion criteria proved to be poor predictors of cervical incompetence, for cases where cerclage would be expected to make a difference. The team that conducted this study

argued that several mechanisms can lead to similar ultrasonographic anomalies, either alone or in combination, such as abnormal implantation, uterine activity, infection, or abruption. This is in line with the multifactorial description of preterm delivery given by Iams et al [8], which considers cervical competence as a continuous variable.

Therefore cerclage therapy should not be indicated only on the basis of ultrasonographic findings, and this observation reinforces the need for a quantitative model taking into account the various factors influencing the outcome of pregnancy. This model would be especially useful to predict the risk for preterm birth in first pregnancies, for which no clinical obstetric history is available.

The surgical procedures like cerclage, although usually helpful to prolong the pregnancy to term, are not successful in some cases, and above all are the source of possible complications such as infection of the genital tract, hemorrhage, or rupture of the fetal membranes. It is therefore of critical importance to improve the criteria used to establish a diagnosis of cervical incompetence, and decide who might benefit or not from a cerclage procedure.

1.5 Current Criteria for the Evaluation of Cervical Incompetence

Although no commonly accepted set of criteria has been established yet to determine whether or not a patient suffers from, or is at risk for, cervical incompetence, a number of parameters and procedures have been identified as potential indicators of this cervical dysfunction. The present section will provide a brief survey of the main techniques currently used to assess cervical function. These techniques and criteria can be classified in three broad categories:

1. Clinical data

2. Imaging techniques

3. Mechanical techniques.

1.5.1 Clinical Data

The most widely accepted criteria to define a diagnosis of cervical incompetence are based on the clinical history of the patient. As stated earlier, cervical incompetence is defined as a "repetitive acute, painless second-trimester evacuation of the uterus without associated bleeding or uterine contraction" [7]. The diagnosis is most often established on the basis of a clinical history of spontaneous abortions in the mid-trimester in the absence of other causes. This clinical history is complemented by examinations performed during the current pregnancy such as repeated digital examination to assess the softness of the cervix, level of dilatation and distensibility at the external os, or even visibility of the fetal membranes.

1.5.2 Imaging Techniques

Ultrasonography

Imaging techniques, and in particular transvaginal ultrasonography are by far the most commonly used technique to assess cervical function in the course of pregnancy (see Figure 1-4). Transvaginal ultrasonography has become very popular in the last decade, and has replaced transabdominal ultrasound imaging in the monitoring of pregnancy. Indeed the transvaginal technique presents the advantage of not requiring an empty bladder, and enables more repeaTable and user-independent measurements than a transabdominal probe ([25], [26]).

A number of parameters can be monitored such as endocervical canal length, diameter at the internal and external cervical os, and also more qualitative parameters such as the presence and shape of "funneling" at the internal os, and the "general aspect" of the cervix. A study by Andersen et al [26] compared the predictive value of cervical length measured by transvaginal ultrasonography with that measured using transabdominal
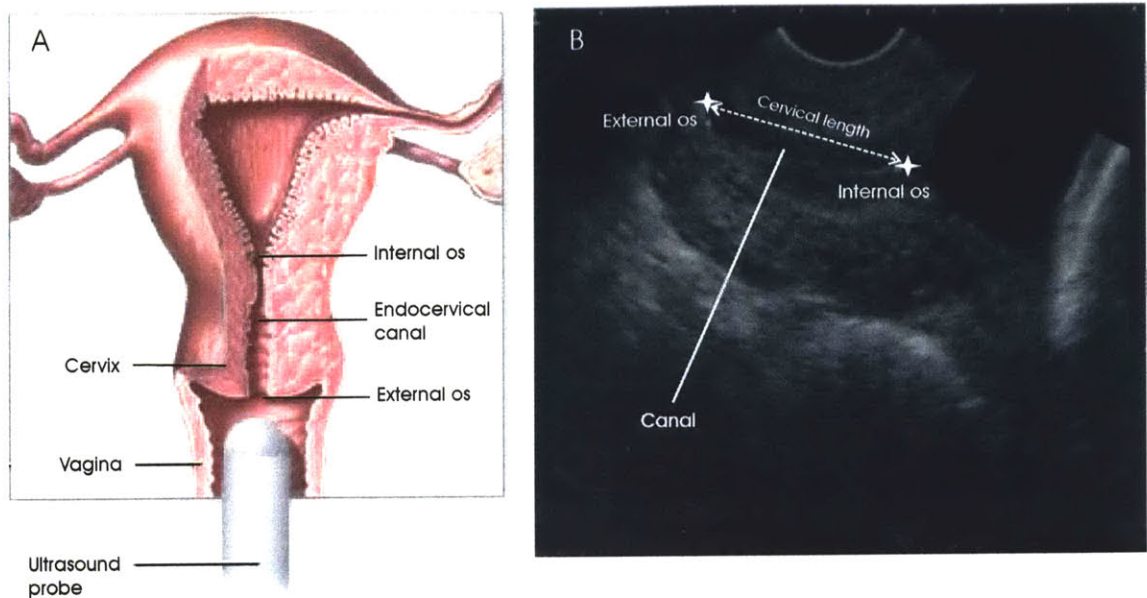
Figure 1-4: Transvaginal ultrasonography. A. Technique: the probe is introduced into the vagina and advanced close to the external os. B. Image obtained for a normal cervix. No funneling is visible at the internal os. (Modified from Iams et al [9]).

imaging, and also cervical effacement as measured by digital examination. The study concluded that transabdominal imaging was not predictive, and that a cervical length inferior to 39 mm measured on transvaginal images could detect 76% of the preterm births, for only 71% for manual examination. The relative risk of preterm delivery was found to correlate positively with the measured cervical length, in agreement with the results of Iams et al [9].

Several other studies have reported transvaginal ultrasonography to be a useful addition to digital examination in the diagnosis of cervical incompetence ([27], [28], [29]), especially as digital examination does not enable the assessment of the distensibility of the upper region of the cervix. Also digital examination requires the placement of the finger close to the fetal membranes, which may increase the risk of infection [30]. A study realized by Nzeh et al [31] compared internal cervical os diameter measured by transvaginal ultrasonography between two groups of pregnant patients: a first group composed

of women with previous cervical incompetence, and a second group composed of women with no prior history of preterm delivery and having had at least one full term pregnancy with normal vaginal delivery. The mean internal os diameters reported were 16.0 mm and 22.5 mm for the cervical incompetence group at 10 and 27 weeks gestation, while the mean values measured for the control group were 7.7 mm and 14.5 mm at 13 and 28 weeks gestation respectively. The internal cervical os diameter as measured thus appears to be a significant marker of cervical incompetence. Another study by Guzman et al [32] used transvaginal ultrasound to monitor the evolution of cervical length between 15 and 24 weeks gestation in patients with and without cervical incompetence. The investigators observed no significant shortening of the endocervical canal length in the control group, while a significant shortening of -0.49 cm/week was reported for the women diagnosed with an incompetent cervix.

The observation of funneling (dilatation of the internal cervical os with protrusion of the fetal membranes in the endocervical canal) on ultrasound images is also frequently associated to cervical incompetence. The sequence of letters T-Y-V-U has been proposed to describe the evolution of the sonographic appearance of an incompetent cervix with progressive funneling ([1], [33]). Figure 1-5 illustrates these stages of cervical effacement as pregnancy progresses.

Variations of traditional transvaginal ultrasonography have been proposed to investigate cervical incompetence, without much success. Recently, three-dimensional transvaginal sonographic imaging has been proposed as an alternative to traditional 2D-imaging to assess cervical function [34]. Two groups of patients, one composed of women with a low risk and one of women with a high risk of cervical incompetence, were monitored using both 2D and 3D-sonography. Cervical length was recorded using the traditional technique, and 3D-volume calculations of the cervix were performed using the 3D-scans. Contrary to the original hypothesis of the investigators that volume measurements may be more sensitive and less user-dependent than traditional 2D cervical length measurements, the values found for the cervical volumes did not show any significant statistical
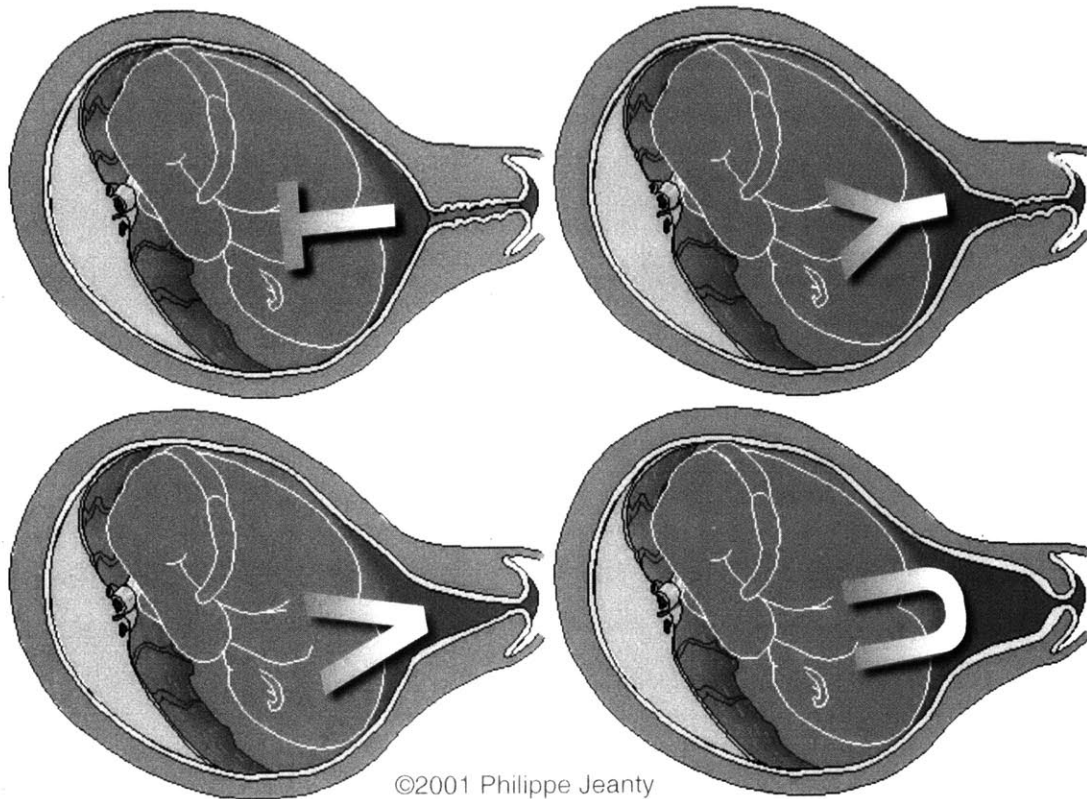
Figure 1-5: Characteristic T-Y-V-U sequence observed on transvaginal ultrasound with evolution of a pregnancy affected by cervical incompetence (modified from www.thefetus.net).

difference between the two groups, whereas cervical length was significantly shorter in the high-risk group.

MRI

Other imaging techniques such as MRI have been proposed to assist in the diagnosis of cervical incompetence. An early study realized by Hricak et al [35] compared the appearance of the cervices of three groups of non-pregnant patients on MR images. The first, second and third groups were composed respectively of 20 women with normal cervices, 11 women with traumatic or congenital cervical incompetence, and 10 women with short cervices due to in utero exposure to diethylstilbestrol (DES). The cervical

length did not significantly differ between the normal patients and the patients with cervical incompetence, but the diameter of the internal cervical os was significantly larger for the latter group (4.5 mm ± 0.3 vs 3.3 mm ± 0.1). Also the MR appearance of the cervical stroma of the cervical incompetence group was associated to a low-to-medium signal on T2-weighed images when compared with patients from the control group. The patients from the DES group were found to have a shorter cervical length (22.9 mm ± 1.7 vs 33.0 mm ± 1.0 for the control group), but normal internal os diameter and signal intensity. The authors concluded that a short cervical length (< 3.1 cm), an increased internal os diameter (>4.2 mm), or altered signal intensity in the cervical stroma are suggestive of cervical incompetence.

Another more recent study [36] used MRI imaging on a pregnant patient to establish a diagnosis of cervical incompetence that previous ultrasonographic imaging had not been able to detect. In this particular case, ultrasonographic imaging had shown fluid in the vagina but no dilatation of the endocervical canal and no bulging of the fetal membranes into the cervix. However MRI imaging performed at the same time demonstrated bulging membranes into the cervical canal and a dilated internal os. This suggests that MRI may be more sensitive than ultrasound imaging to detect cervical incompetence in specific cases.

1.5.3 Mechanical Techniques

Techniques Associated with Ultrasonography

Finally, a number of stress tests have been evaluated in their ability to detect an incompetent cervix. They are often performed in association with transvaginal ultrasonography. The most common tests are the observation of the cervical response to a change in maternal position, or to the application of a transfundal pressure. Wong et al [37] observed the effect of a change from the lying to the upright position on the cervix using transvaginal ultrasonography. The cervical length was measured after 15 minutes in the supine position and again after the patients had been standing for at least 15 minutes. In a group

of 41 patients with high risk for cervical incompetence, 16 showed a decrease greater than 33% in their cervical length in response to the change in position, and among them 14 delivered their infant prematurely. On the opposite, no change was observed for the 24 low-risk patients enrolled in the study, who all delivered their babies at term. The authors also noted that a cervical length $\leq$ 2 cm combined with a positive response to the postural change had a sensitivity of 100% for prediction of preterm delivery.

In a second study, Guzman et al [38] investigated the effect of standing, coughing, and the application of a transfundal pressure on the cervical length. For the patients examined, cervical incompetence was diagnosed by the presence of subsequent progressive cervical changes on ultrasonographic examinations associated to a length $\leq$ 26 mm. The ability of the three different tests to detect cases of cervical incompetence is summarized in Table 1.3. Transfundal pressure was the most reliable and sensitive technique in detecting the patients who experienced progressive shortening of the cervix during the second trimester of pregnancy, and may be more useful than coughing or standing in helping in the assessment of cervical function for patients at risk for preterm delivery.

	Sensitivity	Specificity	Positive predictive value	Negative predictive value
Transfundal Pressure	88.2%	97.2%	88.2%	95.8%
Coughing	16.7%	100%	100%	85.5%
Standing	33.3%	97.2%	75%	85.2%

Table 1.3: Efficacy of coughing, standing, and application of a transfundal pressure in predicting ultrasonographic cervical incompetence, from the study by Guzman et al.

A subsequent study by Guzman, Vintzileos et al [39] examined the evolution of the cervix after a positive response to transfundal pressure between 15 and 22 weeks gestation. In 9 of the 10 patients examined, a significant shortening of the cervical length from 12.2 mm (4 to 20 mm) to 0.0 mm (0.0 to 9.5 mm) was observed between the first and final examination (the values given are median values), and 6 patients had the fetal membranes at the external os. Time intervals between the first and last examination ranged from 2 to 20 days. The 10th patient was lost to follow-up and had a preterm delivery at 23

weeks of gestational age. The authors concluded that the placement of a cervical cerclage was appropriate for patients with a positive response to transfundal pressure.

Cervical Distensibility

Other tests, purely mechanical, have been proposed to evaluate the risk of preterm delivery due to cervical incompetence. A study by Zlatnik et al [40] investigated the efficacy of a scoring system integrating results from catheter traction, hysterography, and Hegar dilator passage tests. 24% of the women with high scores delivered their infant prematurely before 30 weeks in a subsequent pregnancy, compared to only 9% of the women with low scores. Although predictive of preterm delivery, this scoring system had a very low sensitivity, and may only be useful as a complement to obstetric history and other clinical data.

1.6 Conclusion and Project Framework

The techniques to help in the assessment of cervical function, and predict the risk for preterm delivery due to cervical incompetence are numerous. Some of them, such as transvaginal ultrasonography, proved to be of great potential value. However none of these techniques is sufficient by itself to enable a reliable diagnosis of cervical incompetence, and the safe use of therapeutic procedures such as cervical cerclage. Due to the multifactorial nature of preterm delivery, combined with the notion of a continuous scale of cervical competence, quantitative tools integrating the contribution of all the critical factors are necessary in order to improve the reliability and efficacy of the diagnosis. To this day, only simplistic semi-quantitative scoring systems taking into account a very limited number of parameters have been evaluated, and considerable improvements can be achieved.

The present project will try to integrate biochemical parameters and patient-specific anatomical data retrieved from MRI images in a computer-based model designed to

simulate pregnancy. The simulations will be based on a 3-dimensional finite element model, using the patient-specific geometry. The mechanical constitutive equation used to account for the cervix mechanical behavior will integrate biochemical data (such as collagen content, glycosaminoglycans content) as well as mechanical parameters obtained from noninvasive indentation tests performed during routine clinical examination (see Figure 1-6).

This work is focused on the development of the mechanical constitutive model for cervical tissue. Ideally, the model would obey the three following characteristics:

(i) reflect as much as possible the microstructure of cervical tissue, to enable correlation between biochemical data and corresponding constitutive parameters;

(ii) account for tissue orientation, and represent equilibrium as well as transient properties;

(iii) remain reasonably simple in order to achieve the computational efficiency required for large 3D simulations in complex geometries.

The model that will be presented here is still at an early stage of development, and does not presume to satisfy all of these requirements. However preliminary experimental tests realized on tissue samples obtained from hysterectomies have shown encouraging results concerning its ability to accurately model the tissue response.

The presentation of the model will be organized as follows. Chapter 2 will give a brief overview of the composition and microscopic structure of cervical tissue, to provide the necessary basis for the development of the microstructurally based tissue model. Chapter 3 will provide relevant data concerning the mechanical properties of the tissue, and will review previous attempts to model the tissue, before presenting the mathematical model proposed in this study. Chapter 4 will present the results from finite element simulations realized using the proposed model, and experimental data obtained from mechanical and biochemical tests performed on tissue samples obtained from hysterectomies. Finally, chapter 5 will present concluding remarks, as well as recommendations for future work.
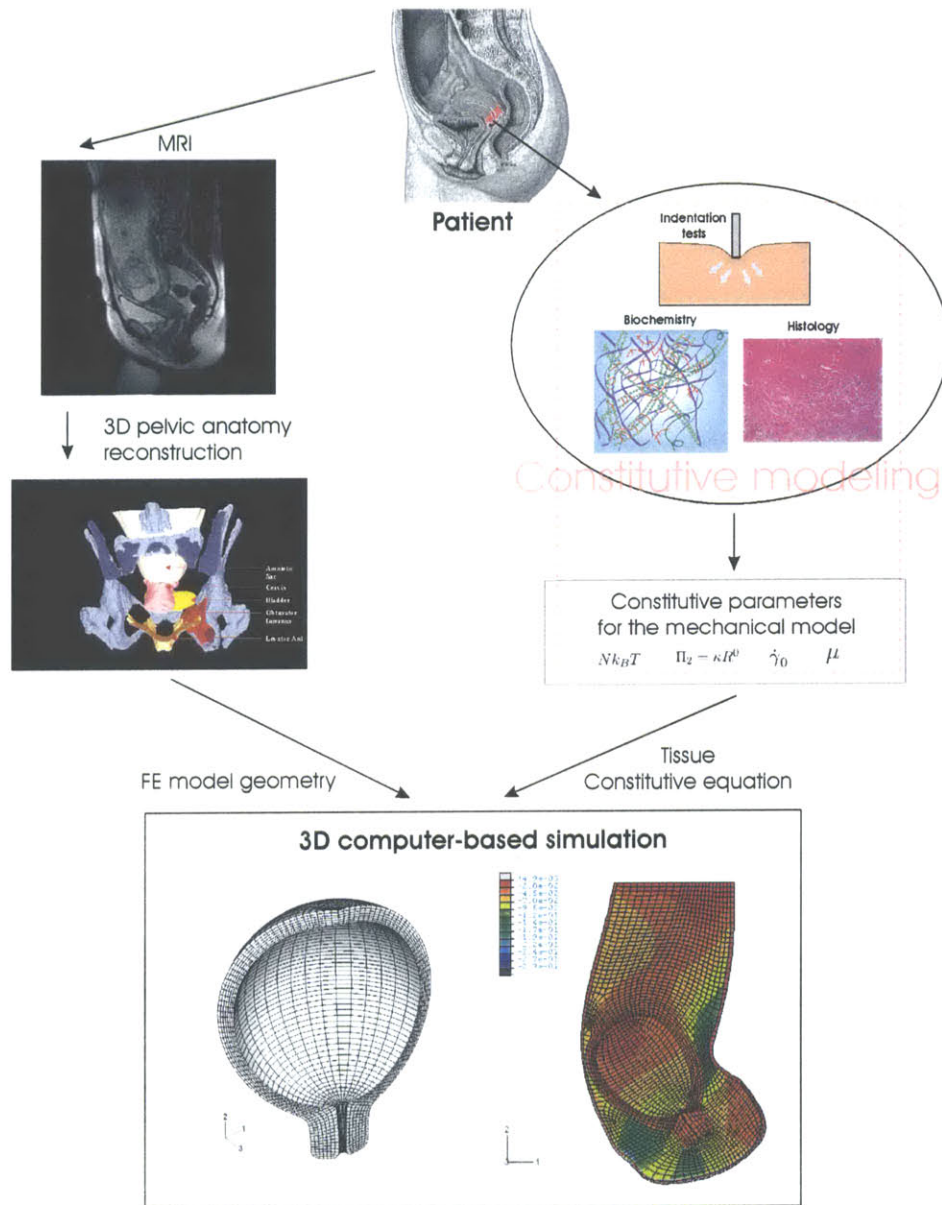
Figure 1-6: Global framework of the project. Computer simulations will be carried out using patient-specific anatomical data, as well as material properties derived from simple biochemical and mechanical tests and integrated into a mechanical model relating microscopic structure to macroscopic tissue properties.

Chapter 2

The Extracellular Matrix of the Cervix

2.1 Introduction

Cervical tissue consists of a sparse distribution of cells, which account for approximately 20% of the total volume [47], embedded in an extracellular matrix. The most represented cell types are smooth muscle cells and fibroblasts. Smooth muscle tissue represents from 6 to 15% of the total cervical tissue ([48], [49], [50]). The other cell types present in the tissue are immune cells, and endothelial cells forming the microvascular network of the tissue.

The extracellular matrix is largely responsible for the mechanical properties of the tissue, and is composed of various types of macromolecules.

The extracellular matrix of the cervix primarily consists of fibers (collagen and elastin) embedded in a ground substance composed of hydrated proteoglycans and glycosamino-glycans. These macromolecules are synthesized by the tissue fibroblasts. The following sections will give a brief overview of these different families of molecules, their basic structural and functional properties, and their distribution among different subtypes in the cervical stroma. Succinct information will then be given concerning the relative vari-

ations of these constituents in the course of normal pregnancy, and in cases of cervical incompetence. Many other different types of molecules are present in the extracellular matrix of the cervix, contributing to the complex organization of the composite structure, however they represent a minor component of the composition and do not give a significant contribution to the measured mechanical response of the tissue.

2.2 Collagen Fibers

2.2.1 Basic Structure

Collagen molecules are glycoproteins consisting of an assembly of repeated aminoacid sequences of the form Gly-X-Y, where X and Y are mostly hydroxyproline and proline. These basic peptide chains can assemble to form sTable triple helical structures, as shown in Figure 2-1. There exists many different types of collagen characterized by different aminoacid sequences and spatial conformations. Nineteen types have been identified until now, and this number is very likely to increase in the near future. Collagen types differ in their triple helical regions, as well as in their capacity to assemble in order to form larger aggregates.

Three types of collagen are found in the cervical extracellular matrix: types I, III and IV [51]. The reader is referred to [41] and [42] for detailed information on the mechanisms involved in their synthesis and degradation. Only their main structural properties will be briefly outlined here.

The basic collagen peptidic chains are called alpha-chains. They form left-handed helical structures. Three of these alpha chains assemble to form procollagen molecules, in which the alpha-chains are supercoiled around a common axis to form the collagen characteristic triple helix (see Figure 2-2.B and 2-2.C). After being released in the extracellular space, the procollagen molecules undergo several modifications of their C and N-terminal regions, leading to new molecules called tropocollagen.

Type I and III collagens are very similar in many aspects. They belong to the fibrillar

Figure 2-1: Molecular structure of collagen. **A**. α-chain, with the repeated Gly-X-Y amino acid sequence, in its left-handed helicoidal conformation. **B**. Right-handed triple helix formed by three individual α-chains supercoiled around the middle axis. (Adapted from Alberts et al, Molecular Biology of the Cell, 3rd ed., Garland Publishing 1994).

collagens, for which fibrils assemble to form higher order fibrous structures. Their respective procollagens have a very long triple helical region, and two short non-helical regions both at the N-terminal and C-terminal ends called telopeptides (see Figure 2-3). The triple helical region is stabilized by disulfide bonds. These tropocollagen molecules spontaneously aggregate in a quarter-stagger arrangement to form collagen fibrils, through the alignment of hydrophilic (charged), and hydrophobic groups of amino acids. The fibrils have a very characteristic cross-striation pattern upon negative staining (see Figure 2-2.D). This parallel arrangement maximizes the resistance of the collagen fibril to tensile forces along their axis. They aggregate to form higher order structures called bundles, that in turn assemble to form collagen fibers (see Figure 2-3). These type I and III fibers are the building chains of the collagen network-like structure described in chapter 3, where the mechanical constitutive model is discussed.

Figure 2-2: Structure of collagen fibrils. A, B, and C show the alpha-chains and procollagen triple helix. D shows collagen fibrils and their characteristic striation pattern.

Type IV collagen is found mainly in basement membranes where it aggregates to from two-dimensional structures. The structure of its tropocollagen is slightly different from that of types I and III. It consists of a long triple helical region, enclosed between a large globular domain at the C-terminal end, and a short telopeptide at the N-terminal end. The triple helical region contains a very characteristic bend near the N-terminus, responsible for the two-dimensional supramolecular arrangement pattern of type IV tropocollagen, as shown in Figure 2-4.

All the different types of collagen supramolecular structures are stabilized by the formation of covalent cross-links, both disulfide and aldehyde-derived bonds.
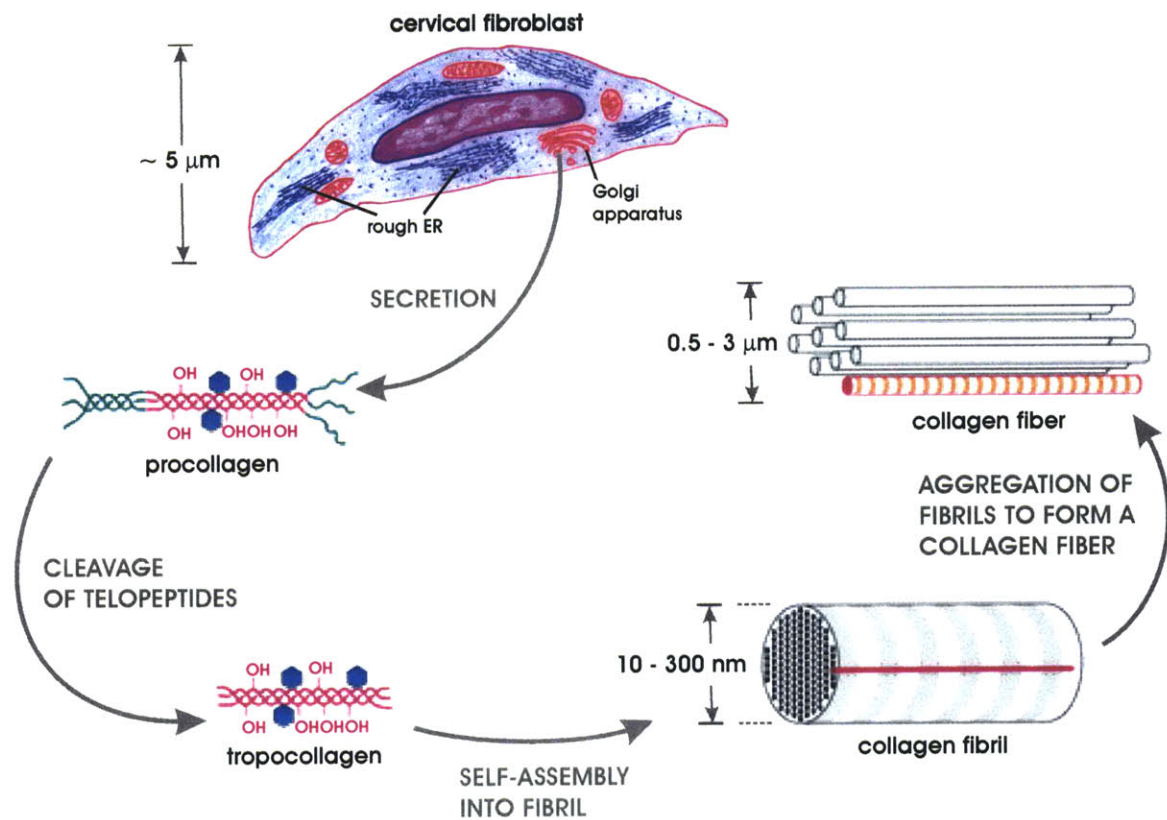
Figure 2-3: Assembly of collagen fibers in the extracellular space. (Adapted from Alberts et al, Molecular Biology of the Cell, 3rd ed., Garland Publishing 1994).

2.2.2 Regulation of Synthesis and Degradation

The concentration of the different collagen types in the tissue is controlled through complex regulation mechanisms of the synthetic and degradative activity. Collagen is renewed through a constant turnover within the extracellular matrix, which is continuously and actively remodeled. Degradation is accomplished through the activity of a number of enzymes (collagenase, proteases), released by the resident fibroblasts, and both transient and permanent populations of immune cells present in the tissue. The mechanisms involved in the regulation of these pathways are very involved, and will not be described here. The reader is referred to [41], [43] and [44] for a detailed presentation of these processes.

2.3 Proteoglycans and Glycosaminoglycans

2.3.1 Structure

Proteoglycans (PGs) are glycoproteins composed of glycosaminoglycan side chains covalently anchored to a core protein. Glycosaminoglycans (GAGs) are linear polymeric assemblies of sulfated disaccharide units. The only exception is hyaluronic acid, a glycosaminoglycan for which the disaccharide units are not sulfated. Hyaluronic acid is not attached to a core protein, and therefore is not considered a member of the proteoglycans family, but is simply referred to as a glycosaminoglycan. The different types of glycosaminoglycans are classified according to the nature of their disaccharide building blocks. Four main categories have been identified, according to their sugar residues, their linkage, and the position and density of sulfated groups (Table 2.1).

Proteoglycans are categorized according to the structure of their core protein, the nature of their glycosaminoglycans side chains, and the length of these polymeric chains. PG molecules can be of very different sizes, ranging from $\simeq 100$ kDa for the smallest PGs such as decorin, up to $\simeq 3000$ kDa for aggrecan, a large proteoglycan found in cartilage
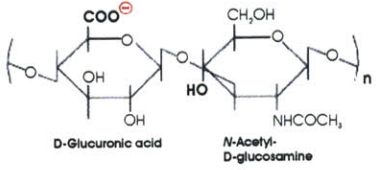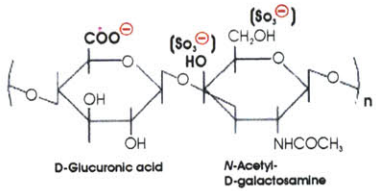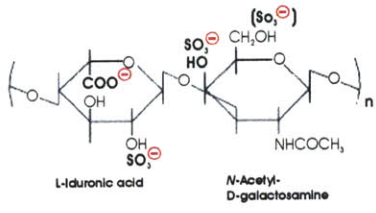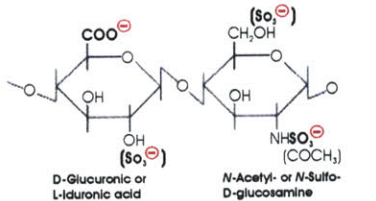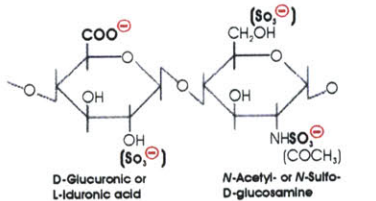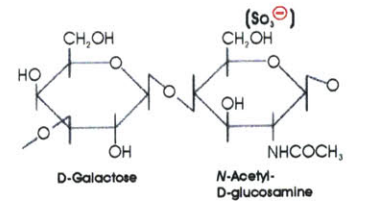
GAG	Molecular weight (Da)	Repeating disaccharide unit	Sulfates per disaccharide unit	Linked to Protein	Present in cervix
Hyaluronic acid	4,000 to 10×10^6	D-Glucuronic acid / N-Acetyl-D-glucosamine	0	-	+
Chondroitin sulfate	5,000-50,000	D-Glucuronic acid / N-Acetyl-D-galactosamine	0.2-2.3	+	±
Dermatan sulfate	15,000-40,000	L-Iduronic acid / N-Acetyl-D-galactosamine	1.0-2.0	+	+++
Heparin	6,000-25,000	D-Glucuronic or L-Iduronic acid / N-Acetyl- or N-Sulfo-D-glucosamine	2.0-3.0	+	-
Heparan sulfate	5,000-12,000	D-Glucuronic or L-Iduronic acid / N-Acetyl- or N-Sulfo-D-glucosamine	0.2-2.0	+	+
Keratan sulfate	4,000-19,000	D-Galactose / N-Acetyl-D-glucosamine	0.9-1.8	+	-

Table 2.1: Classification of glycosaminoglycans. (Modified from Alberts et al, Molecular Biology of the Cell, 3rd edition, Garland Publishing 1994).

tissue. HA molecules can also be very large, with the longest chains up to $\simeq 10000$ kDa (Figure 2-4).

fibrilar collagen [MW ~ 290,000]

hyaluronic acid [MW ~ 8 x 10⁶]

decorin [MW ~ 40,000]

type IV collagen

aggrecan [MW ~ 3 x 10⁶]

100 nm
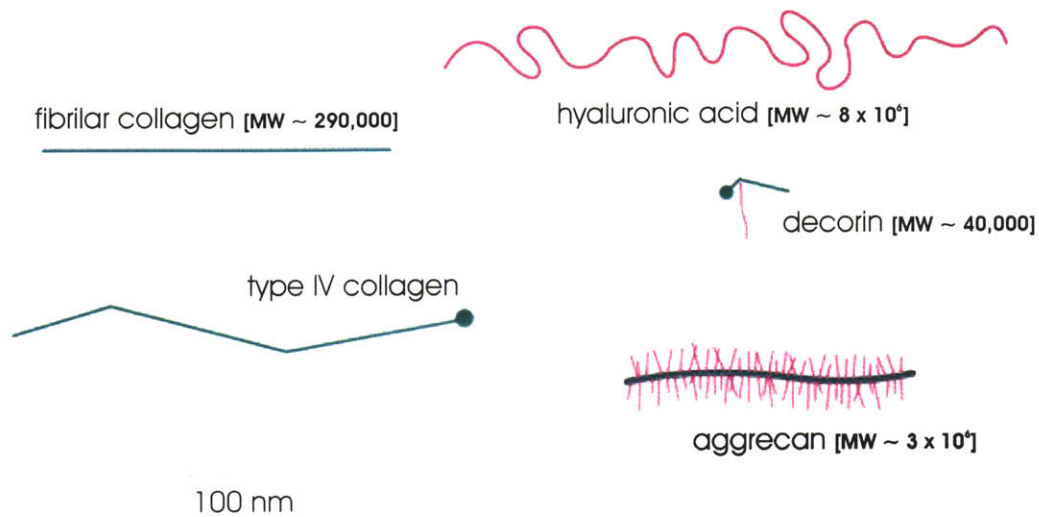
Figure 2-4: Structure and size of different collagens, PGs and GAGs. (Modified from Alberts et al, Molecular Biology of the Cell, 3rd ed., Garland Publishing 1994).

Decorin, shown in Figure 2-5, is the major proteoglycan found in the human cervix, and is composed of a short core protein associated to a single GAG chain, either dermatan sulfate or chondroitin sulfate.

2.3.2 Electrical Properties

All types of glycosaminoglycans contain a large number of highly charged (negative) side groups. These charges correspond to either sulfated hydroxyl groups, or ionized carboxyl groups (Table 2.1). Each disaccharide group possesses between 0 and 4 negative charges depending on the types of hexoses of which it is composed, the degree of sulfation of the hydroxyl groups, or the pH. These fixed electrical charges are responsible for the hydration of the tissue through a Donnan effect. External counterions are attracted to achieve electroneutrality, and the increase in counterion concentration results in an os-
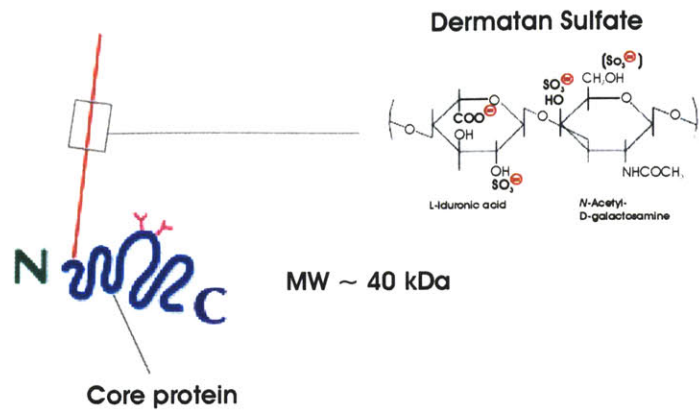
Figure 2-5: Structure of decorin, the major proteoglycan found in the human cervix.

motic swelling pressure with large amounts of water drawn into the tissue. The hydrated proteoglycans take the appearance of swollen sponges, or "brush-like" structures, as can be seen in Figure 2-6. Due to these effects, the PGs and GAGs are highly resistant to compressive deformations, and their free swelling tendency is constrained by the tensile forces developed in the collagen fibers embedded within the matrix.
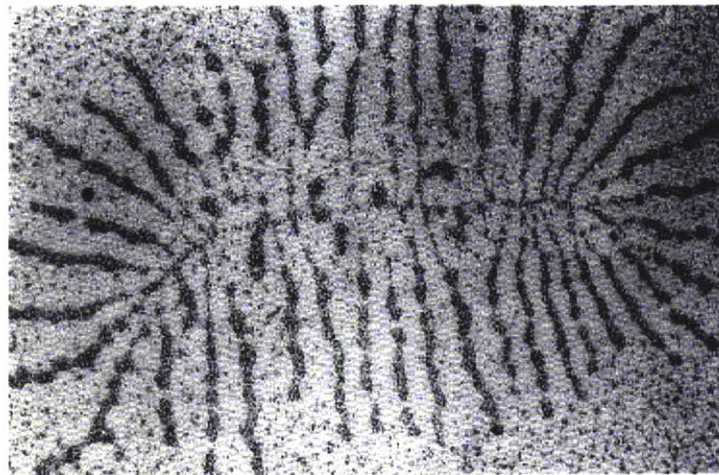
Figure 2-6: Micrograph of a large proteoglycan, displaying the characteristic brush-like structure.

2.3.3   Synthesis and Degradation

The control of the synthesis and degradation of proteoglycans is the result of complex regulatory mechanisms as in the case of collagen. Degradation can occur by two main mechanisms [43]. Either the core protein is degraded extracellularly by secreted enzymes, and the remaining GAG chains are degraded in liver endothelial cells after passing through the blood circulation, or whole molecules are degraded within the local fibroblasts following endocytosis.

2.4   Elastic Fibers

The third main element present in most extracellular matrices is elastic fibers. Elastic fibers are complex structures composed of different types of molecules, including elastin, microfibrillar proteins, lysil oxidase and possibly proteoglycans [52]. Elastic fibers are highly insoluble, and are usually the last constituent of the extracellular matrix remaining after sequential extractions using acids, alkali and protein solvents.

2.4.1   Structure

Elastic fibers assemble in different supramolecular structures depending on the tissue type. They can form two-dimensional sheet-like structure as is the case in the media (central layer) of blood vessel walls. The sheets form parallel concentric layers that are crossed by a few radially oriented fibers to facilitate stress transmission across the layers [52]. In tissues like skin, lung or ligament, they exist at the state of thin rope-like filaments of variable length. In the case of cartilage for example, the fibers are thicker and connected to form a fully three-dimensional network structure. The human cervix contains elastin fibers in a mature and cross-linked state. The cervical elastin content ranges from 0.90% to 2.4% of the dry weight [47], and does not change during pregnancy [53].

2.4.2 Functional and Mechanical Properties

The main functional property of elastic fibers is to provide tissues with elasticity in response to stretching. The distensibility of elastic fibers is highly reversible, and enables tissues to come back to their initial shape by elastic recoil, even after significant extensions. This is particularly important in the case of blood vessels for example, for which the pulsatile blood pressure imposes repeated dilations of the vessel wall. Elastic fibers are also responsible for the elastic properties of skin, or lung tissue, constantly undergoing finite deformations.

The role of elastic fibers in the uterine cervix is believed to be mostly restricted to the postpartum period, in which they enable the tissue to rapidly come back to its original shape after the extensive dilation caused by delivery [71]. Nevertheless some investigators have mentioned a decreased content in elastin to be a potential cause for cervical incompetence [54].

The elastomeric properties of elastic fibers can be partially explained by the same mechanisms as those involved in rubberlike elasticity [52], [55]. Indeed elastic fibers can form three-dimensional crosslinked networks like rubberlike polymers (Figure 2-7). For these polymers the elastic recoil is explained in terms of variations of the configurational entropy of the individual chains, which dominate over changes in internal energy. Stretching the chains towards their maximum extension reduces the number of available configurations and thus decreases their entropy. When the load is released, the chains tend to increase their level of entropy again, and return to their initial highly disordered state [55]. This theory is only partly applicable to explain the properties of elastin, as some degree of order exists along certain regions of the chains, that do not allow for configurational flexibility, and thus changes in entropy. The more complex mechanisms that may be involved in the three-dimensional deformation of elastic fiber networks are yet to be investigated.

The large deformations elastin can sustain can be attained with relatively small forces, compared to those developed in the collagen fibers. Their role is essentially limited to the
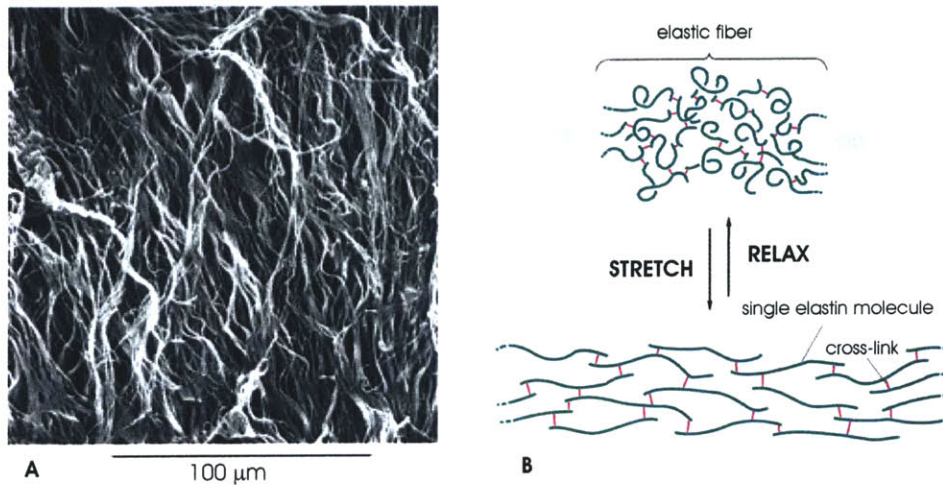
Figure 2-7: Structure of elastic fibers. **A**. Scanning electron micrograph of the dense network of elastic fibers found in the outer layer of a dog's aorta. (Reproduced from Haas K.S., Phillips S.J., Comerota A.J., and White J.W., Anat. Rec. 230:86-96, 1991). **B**. Schematic of an elastic fibers network in uniaxial stretching. (Modified from Alberts et al, Molecular Biology of the Cell, 3rd ed., Garland Publishing 1994).

unloading stages, in which they bring the tissue close to its initial state. Their Young's modulus is estimated to be of order $\simeq 3 \times 10^6$ Pa, compared to a value of $\simeq 1 \times 10^9$ Pa for collagen fibrils ([42], [56]). Based on these remarks, and the limited amount of elastin fibers present in the cervical stroma, their contribution to the total stress developed in the tissue during loading phases will be lumped together with the collagen response in the model exposed in chapter 3.

2.5   Composition and Structure of the Cervical ECM

From a mechanical standpoint, the cervical ECM can be considered essentially as a collection of collagen I and III fibers, embedded in a highly hydrated glycosaminoglycans ground substance. The present section will provide some additional detail about the different subtypes and concentrations of these macromolecules in the cervical stroma, as well as their structural organization, both in the non-pregnant state and during pregnancy.

2.5.1 The Cervical ECM in the Non-Pregnant State

Water accounts for $\simeq 80\%$ of the weight of cervical tissue. This high level of hydration is widely attribuTable to the sulfated proteoglycans and the hyaluronic acid with their negative fixed charge density.

Total collagen represents $\simeq 70\%$ of the dry mass [57]. Type I fibers predominate, accounting for approximately 60-80% of the total collagen, the remaining 20-40% being primarily type III fibers ([58], [59]).

Some degree of macroscopic collagen orientation has been reported by Aspden in the case of human cervices [72], and Leppert et al [73] for rat cervices. However, examination of stained stromal samples from human cervices obtained from hysterectomy specimens did not enable us to identify a substantial degree of anisotropy in the arrangement of the collagen bundles (Figure 2-8).
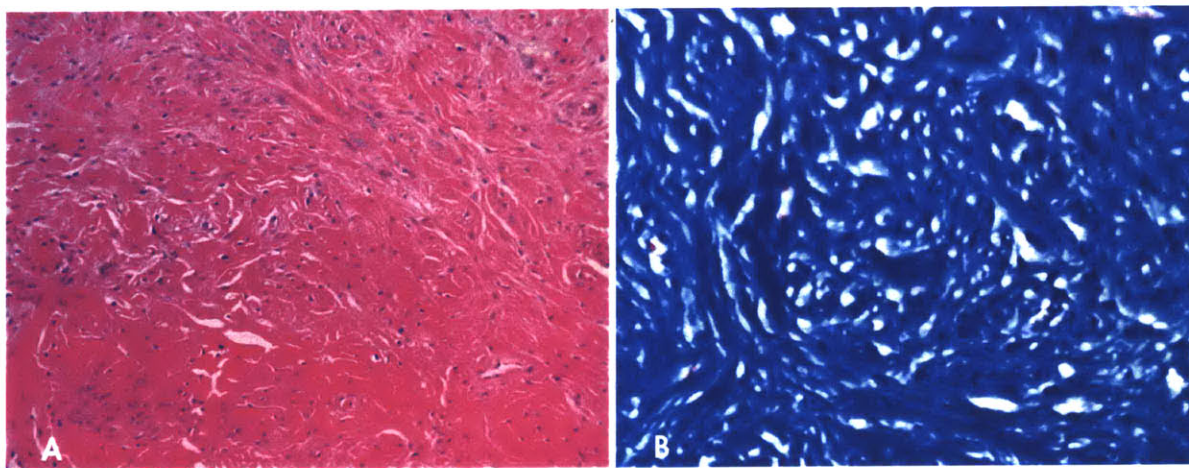
Figure 2-8: Histological preparations of human cervical samples. **A**. H&E stain. **B**. Trichrome for identification of the collagen fibers. No preferred direction of alignment is visible.

The GAGs represent approximately between 0.2% and 1.5% of the dry mass of the tissue ([63], [12], [74]). Even at this relatively low concentration, their contribution to the properties of the tissue is critical. Indeed their level of hydration is such that they occupy a large fraction of the total volume. As an example, a hyaluronic acid molecule of

3000 kDa would have a volume 100,000-fold higher than that of a collagen molecule of the same weight [60] (Figure 2-9). Three major types of glycosaminoglycans are represented in the cervical extracellular matrix. The dominant ones are dermatan sulfate PGs (in particular decorin), accounting for 76% of the total GAGs, while heparan sulfate PGs represent 13%, and hyaluronic acid 11% of the total [61]. However, other studies reported the presence of chondroitin, as well as chondroitin 4 and 6-sulfate GAGs in cervical tissue [62]. These differences might be explained by the variability of the tissue composition from one anatomical location to the other [63]. Nevertheless, quantification of the GAGs in the cervix is difficult and controversial, and many studies report conflicting data [64].

globular protein (MW 50,000)

collagen (MW 290,000)

hyaluronic acid (MW 8 x 10^6)

300 nm
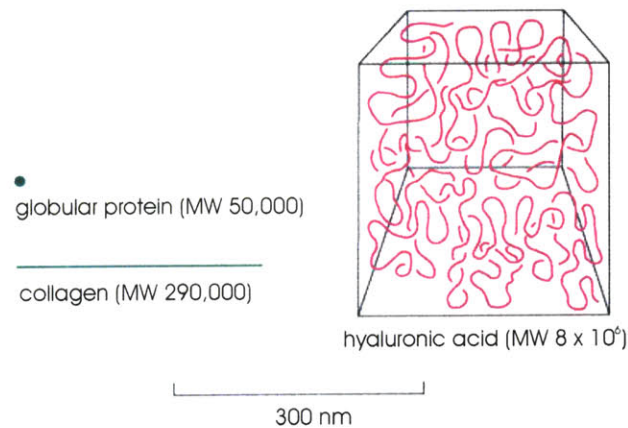
Figure 2-9: Relative volumes occupied by collagen, a typical globular protein, and a hyaluronic acid chain. (Modified from Alberts et al, Molecular Biology of the Cell, 3rd ed., Garland Publishing 1994).

Table 2.2 recapitulates the main components of cervical tissue in the non-pregnant state.

2.5.2 Evolution During Pregnancy

The cervical ECM is subject to tremendous changes in the course of pregnancy, especially in the final stages preceding parturition. A dramatic increase in cervical distensibility is

Water	~80%			
Dry tissue	~20%			
	Collagen ~70% [57] Type I Type III ~70% ~30% ([58], [59])	GAGs ~0.2-1.5% ([12], [63], [74]) Dermatan Heparan Hyaluronic sulfate sulfate acid 76% 13% 11% [61]		Elastin ~2% [47]

Table 2.2: Main constituents of human cervical tissue in non-pregnant women.

observed during the last days before delivery, and this mechanical evolution is associated with changes in the tissue microstructure and biochemical composition. Water content slightly increases towards the end of pregnancy (by $\simeq$ 5% [71]). Collagen content, as determined by hydroxyproline concentration, decreases towards parturition to about 30% of its value in the non-pregnant state [65]. This variation is believed to account for a large proportion of the cervical softening observed prior to labor. Increased collagen extractability in late pregnancy has also been reported by several investigators ([65], [12]). The extractability in pepsin has been found to increase by about 40% of its value in the non-pregnant state. This is most likely due to an increase in the collagen turnover, with a higher degradative activity (a 2-fold increase in collagenase activity was reported), combined with a rate of collagen synthesis about as high as in the non-pregnant state. This increases the proportion of newly synthesized collagen, with fewer cross-links and less mechanical resistance.

Glycosaminoglycans are subject to variations of their concentration as well, although these findings remain controversial. Indeed several studies have reported dermatan sulfate to decrease in the course of pregnancy ([66], [67]), whereas others reported almost no variation [68], or even an increased dermatan sulfate concentration [63]. Hyaluronic acid is also subject to conflicting findings. The graph in Figure 2-10 illustrates the variations in the concentrations of the main GAGs found in the cervix, from measurements taken at different stages of pregnancy, following the data obtained by Rath et al [63]. These plots show the very fast remodeling that occurs in the last days of pregnancy, especially
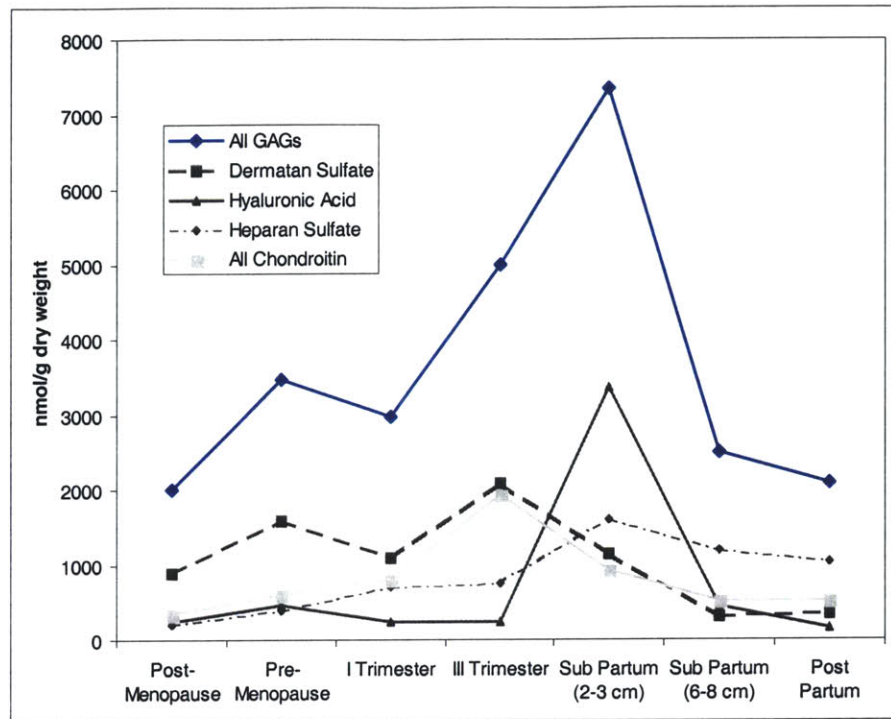
Figure 2-10: Content of the cervix in the different glycosaminoglycans for non-pregnant women, and at various stages of pregnancy, plotted from the data of Rath et al [63]. The concentrations are expressed in nmol of disaccharide per gram of tissue dry weight.

during labor. The very high sensitivity of the measurements to timing may contribute to explain the discrepancy between the different studies.

The increase noted in the total GAGs concentration in this study, and particularly hyaluronic acid, could explain the disorganization of collagen fibers towards the end of pregnancy. The associated absorption of water contributes to increase the spacing between collagen fibrils, and progressively makes them less compact and tightly bound than in the non-pregnant state, thus reducing their load bearing capacity. Moreover, the associated change in the GAGs distribution, with a decrease in dermatan sulfate and particularly decorin, is consistent with a decrease in collagen cross-links, due to the ability of this small PG to bind to collagen and create bridges between collagen fibers.

2.5.3 Relation to Cervical Incompetence

A few studies have characterized the biochemical composition of incompetent cervices. Petersen et al [13] measured the hydroxyproline content and collagen extractability of biopsies from non-pregnant women with congenital cervical incompetence, as diagnosed by a history of spontaneous second trimester abortion with painless dilation of the cervix, in the absence of previous cervical trauma. They obtained similar measurements for parous women without cervical incompetence for comparison. They noted a lower hydroxyproline concentration for women with cervical incompetence (55.4 $\mu g/mg$ dry weight versus 73.6 $\mu g/mg$ dry weight), in addition to a much higher extractability (80.2% versus 49.5%). These results demonstrate that congenital cervical incompetence is most likely related to a defect in the biochemical composition of the cervical extracellular matrix.

In a second study, Rechberger et al [12] performed similar tests on women with, and without cervical incompetence. The investigators reported comparable hydroxyproline concentrations for both groups, but a significantly higher collagen extractability in acetic acid and pepsin for the incompetent cervices. In addition, measurements of sulfated GAGs and hyaluronic acid concentration were also performed, and revealed a lower hyaluronic acid content for the women with cervical incompetence. Finally, the same authors conducted mechanical testing on one biopsy specimen from an 18-weeks-pregnant woman with cervical incompetence, which revealed a much lower stiffness modulus than control cervices, close to the stiffness found for pregnant women near term.

2.6 Idealized Model Proposed for Cervical Tissue

Based on the biochemical and histological characteristics outlined in the previous sections, a simplified structure is proposed to represent the microstructure of cervical tissue, including only those features expected to play a significant role in the mechanical function.

The mechanical response will be modeled as that of the tissue extracellular matrix,

neglecting in a first approximation the contribution of cells. The matrix response will be considered as coming from the cooperative contributions of the collagen fibers and the hydrated GAGs network. Transient effects associated to interstitial fluid flow through the porous solid matrix will also be incorporated in the mathematical formulation presented in chapter 3.

In conclusion, the idealized structure retained to serve as a basis for the development of the constitutive model is illustrated in Figure 2-11. The GAGs network is made up of the dominant small proteoglycans such as decorin, bridging collagen fibers at different locations and increasing their crosslink density, and the long chains of hyaluronic acid.
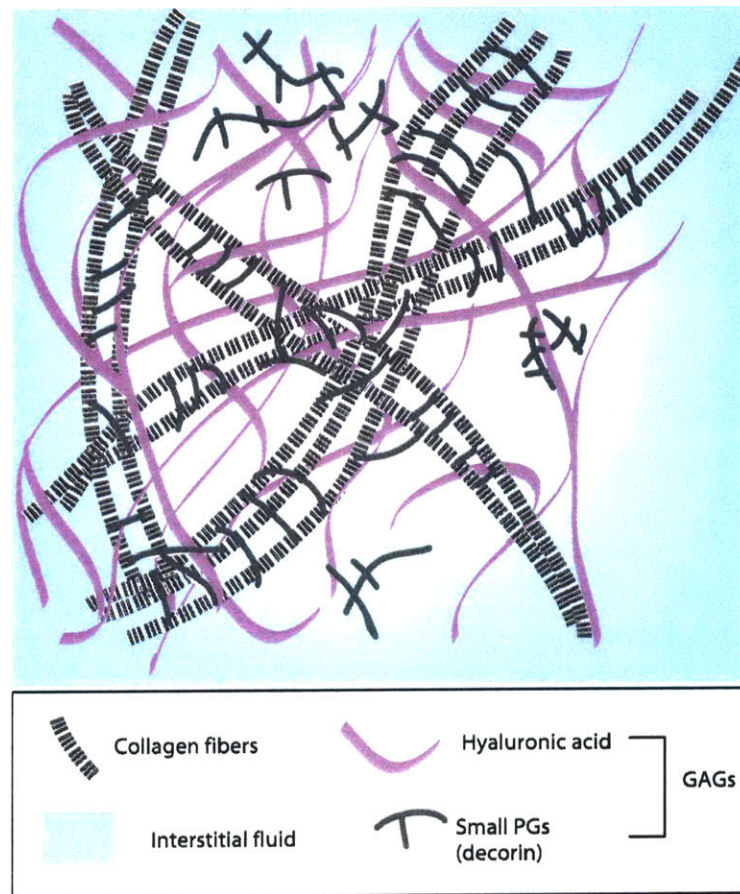
Figure 2-11: Idealized representation of the cervical extracellular matrix.

Chapter 3

Mechanical Constitutive Model for the Cervical Stroma

3.1 Review of the Previous Models

In spite of a number of studies aimed at understanding the complex mechanisms that govern cervical function throughout pregnancy, there has been relatively little work focusing on the mechanical behavior of human cervical tissue over the past few decades. The cervix has the remarkable particularity of being mechanically stiff enough to retain the conceptus in utero for the whole duration of the pregnancy, and constantly remodeling until term to soften and allow for the extreme dilation required during normal delivery. A few investigators have looked at the mechanical behavior of the tissue at various stages of pregnancy, both in animal models such as rats or rabbits, and to a smaller extent in humans.

These studies have shed some light on the behavior of the tissue and its changes throughout pregnancy by the means of simple mechanical tests such as tension, compression, or creep tests of either small tissue samples extracted at different locations, or whole cervices. However the mechanical data obtained from these tests have always been explained in the limits of simple models such as linear elasticity, or linear viscoelasticity.

Often the theories involved are only relevant to simple unidimensional modes of deformation, and very few attempts have been made to account for the full three-dimensional behavior of the tissue. The next section will give a brief review of the mechanical characteristics of cervical stroma, in terms of simple models involving quantities such as a Young's modulus or creep rate, and the following section will describe models in the literature that attempted to derive relationships between its microstructure and mechanical behavior.

3.1.1 Mechanical Properties of the Cervical Stroma

Most of the mechanical data available in the literature for cervical tissue was obtained from animal specimens such as rats and rabbits. Although cervical function is mostly similar in these species and in the case of humans, the biochemical structure of the respective cervical tissues as well as their mechanical properties can differ significantly. Therefore only data obtained from human cervical samples will be briefly presented here.

The work realized by Conrad et al [69] provides results from simple uniaxial tension tests realized on human cervical stripes. The samples were excised from different anatomical locations within the cervix, both axially (at different distances from the internal and external os) and transversely (at different radial distances from the endocervical canal). Also, samples from pregnant patients were tested under the same conditions. Figure 3-1 shows a comparison of the stress/strain curves obtained in uniaxial tension for samples excised from the cervix of a pregnant and a non-pregnant patient. One can note a two to three-fold increase in the stiffness modulus from the pregnant tissue to the non-pregnant tissue. Also, a non-linear stiffening behavior is visible in the non-pregnant case, as the modulus increases with strain, as opposed to the pregnant cervix, for which the stiffness quickly reaches a maximum shortly before yielding.

Figure 3-2 displays a comparison of similar stress/strain plots obtained for cervical samples excised at different radial locations. As can be observed, the stiffness modulus obtained from analysis of the linear portion of the curves decreases with increasing
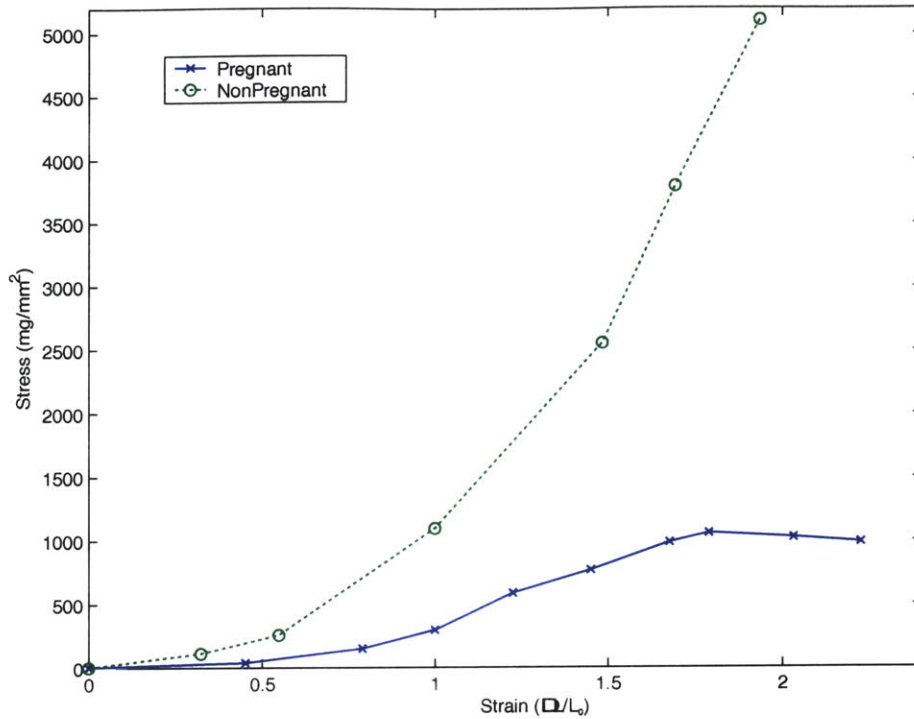
Figure 3-1: Stress-strain curves for human cervical tissue in uniaxial extension. The two curves show data obtained for pregnant (term) and non-pregnant tissue. (Modified from Conrad et al [69]).

distance from the endocervical canal. For the samples tested, the mean values of the measured stiffness modulus were 64.344 kPa, 41.33 kPa, and 24.22 kPa for the inner, middle and outer regions respectively. All the tests were realized at a speed of elongation of 0.1 cm/min.

Another more recent study investigated the biomechanical properties of biopsies of cervical tissue from nonpregnant women [70]. In this study, the authors characterized both the active contractile properties of the tissue, as well as its passive tensile strength. The results of the study revealed a maximum isometric contractile ability of 0.16 ± 0.05 and 0.84 ± 0.47 mN/mm^2 (eq. to kPa), for stripes from the distal and proximal parts of the cervix respectively. These values are significantly lower than those found for the isthmus and fundus of the uterus (4.85 ± 1.0 and 6.50 ± 1.4 mN/mm^2 respectively). The passive tensile tests realized on similar cervical samples demonstrated a mean tensile
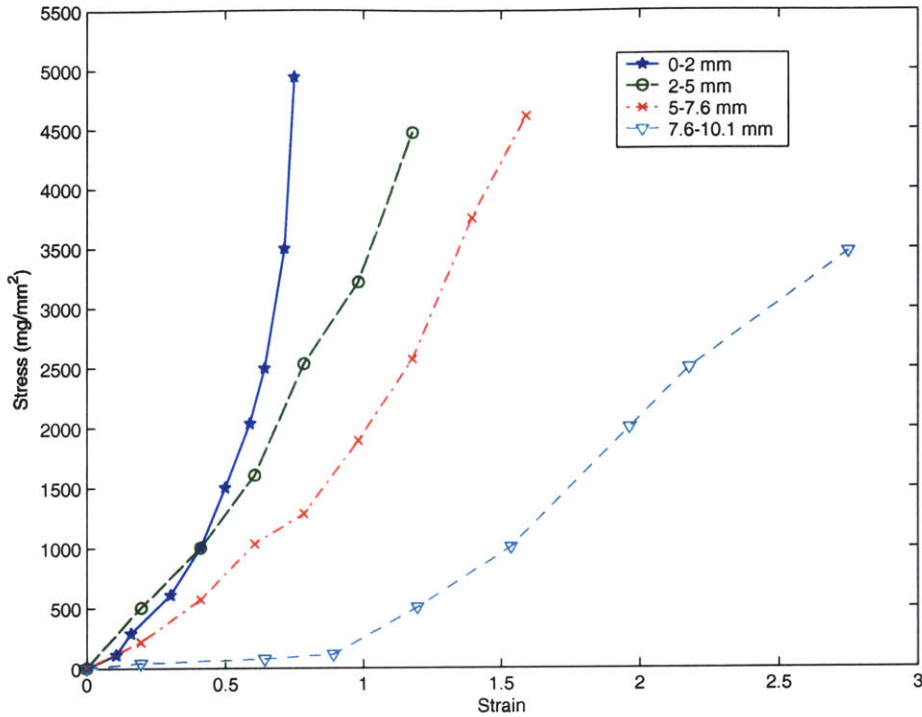
Figure 3-2: Stress-strain curves for human cervical tissue (non-pregnant) in uniaxial extension. The different curves correspond to samples excised at different radial distances from the central canal, in the internal os region, for the same patient. (Modified from Conrad et al [69]).

stiffness of 3.9 MPa and 4.0 MPa for longitudinal and circular stripes from the proximal cervix respectively, and 3.2 MPa and 3.6 MPa for longitudinal and circular stripes from the distal cervix. The tests were realized at a speed of elongation of 1 cm/min. Although the authors claim that these values are comparable with those obtained by Conrad et al [69], they differ by almost two orders of magnitude ($\simeq$3.5 MPa compared with $\simeq$40 kPa). Although the speed of the tests in the latter study was ten times higher than in the previous one, this could certainly not explain such a large variation in the measured tensile moduli. However, even if the data from the two studies seems inconsistent, the results of the study by Petersen et al [70] confirm the hypothesis made in chapter 2, according to which the mechanical properties of cervical tissue can be attributed almost exclusively to its extracellular matrix. Indeed the passive tensile strength of the tissue

was proved to exceed by a 10^4-fold factor its maximum contractile ability, thus proving the contribution of smooth muscle to the global mechanical properties to be very small. Also, no significant difference was noted between the tensile stiffness of circular and longitudinal samples, reinforcing our hypothesis of isotropic mechanical properties.

3.1.2 Existing Constitutive Models

Only one noTable model was developed to relate structural features to mechanical properties for cervical tissue, by R.M. Aspden in 1987 [71]. In this work, Aspden applied the theory of fibre-reinforced composites to cervical tissue, in an attempt to explain the reduction of the stiffness of the tissue by a factor of roughly 10 in the course of pregnancy. The model is based on the assumption that the tissue can be considered mechanically equivalent to a fibrous network (corresponding to the collagen fibers), embedded in a ground substance (matrix, mainly composed of hydrated glycosaminoglycans). The breaking stress of the composite material σ_C is then estimated by the following equation:

$$\sigma_C = \beta\sigma_f + (1 - \beta)\sigma_m, \tag{3.1}$$

where β represents the volume fraction of the collagen fibers in the tissue, σ_f the breaking stress of the fibers, and σ_m the breaking stress of the matrix. As both components are taken to undergo the same level of deformation, the very stiff nature of the fibers with respect to a comparatively soft ground substance makes the second term in equation (3.1) almost negligible, and the breaking stress reduces to

$$\sigma_C \approx \beta\sigma_f. \tag{3.2}$$

A correction is then brought to account for the average orientation of the fibers with respect to the direction of the applied stress, as this strongly influences their ability to carry the load. This is done by means of an "efficiency of reinforcement" η, defined by

$$\eta = \cos^4 \varphi, \tag{3.3}$$

where φ is the average angle between the collagen fibers and the applied stress. This factor is incorporated in equation (3.1) to give the following expression for the limiting stress the tissue can withstand along a given axis:

$$\sigma_C = \beta\eta\sigma_f + (1 - \beta)\sigma_m. \tag{3.4}$$

The same relationship is used to relate the Young's moduli of the different constituents to that of the composite tissue:

$$E_C = \beta\eta E_f + (1 - \beta)E_m \tag{3.5}$$

In a parallel experimental study [72], Aspden determined the average orientation of the collagen fibers in human and rat cervical tissue. For non-pregnant cervices, the same value of $\eta = 0.6$ was found for a load oriented along the axis of the cervix, or circumferentially. An identical analysis for cervices at term showed a decrease in the efficiency to the value of $\eta = 0.2$, which corresponds to a random orientation of the fibers in the matrix. This simple model accounts semi-quantitatively for the decrease of the stiffness of the tissue by roughly a factor of 6 throughout pregnancy, given a decrease of the collagen concentration by approximately 50%, and a factor of 3 contribution resulting from the randomization of the fibers orientation.

In Aspden's model, these mechanisms only account for half of the variation in stiffness. An additional correction factor accounts for the nature of the interactions between the embedded collagen fibers and the surrounding matrix. This effect is represented in terms of the efficiency of the stress transfer between the fibers and the ground substance. If the matrix exerts a shear stress τ on the fibers, these need to exceed a critical length l_c for optimal reinforcement, given by

$$l_c = r\frac{\sigma_f}{\tau},$$ (3.6)

where r is the radius of a collagen fiber. The effect of this critical length can be roughly estimated in terms of the relative strength of interaction between different glycosaminoglycans present in the cervix, and the collagen fibers. Indeed it is known that certain glycosaminoglycans have stronger interactions than others with the collagen, with for example

$$\tau_{Dermatan\ Sulfate} > \tau_{Hyaluronic\ Acid} > \tau_{Keratan\ Sulfate}.$$ (3.7)

The variation in the relative proportions of these glycosaminoglycans in the tissue towards term may contribute to increase the critical length l_c, which might then exceed the actual length of the collagen fibers and reduce the efficiency of reinforcement.

Finally, the increase in water content of $\sim 5\%$ noted towards parturition is discussed as a possible explanation for the remaining decrease in stiffness and creep resistance. The successive gain and loss of water are hypothesized to be responsible for the fast changes in the mechanical properties of the cervix just around delivery, taking effect on a scale of a few hours, whereas biochemical remodeling occurs on a time scale of several days.

In conclusion, this simple fibre-reinforced model attains its objective to explain in a semi-quantitative way the evolution of the stiffness of the cervical tissue in pregnancy, but its underlying assumptions of linearity and small deformations make it restricted to very simple estimates of the material properties. The tissue is inherently non-linear, and can undergo large deformations that are incompatible with the proposed model. Moreover, the model only considers equilibrium properties, and doesn't give any insight in transient phenomena such as interstitial fluid flow, that are crucial in the short time range response of the tissue to various loading conditions, even if this effect is less critical for the cervix under physiological conditions than for a connective tissue like cartilage, for which fluid flow is essential in supporting large instantaneous compressive loads. Also, the connection

between composition and mechanical properties, as illustrated by inequality (3.7), is only very qualitative.

3.2 Global Structure of the Proposed Model

As seen in chapter 2 and in the previous section, the dominant biochemical constituents in terms of mechanical behavior are the collagen fibers and the hydrated network of glycosaminoglycans. The stiffness in tension is provided by the collagen network, whereas the resistance to compressive forces is primarily given by the highly hydrated glycosaminoglycans molecules (proteoglycans and hyaluronic acid). The effects of the cells (smooth muscle and fibroblasts) on the passive biomechanical properties are neglected here, as explained previously, and the contribution of the elastic fibers is integrated within the model used to represent the collagen response. The collagen network is very stiff in tension. The glycosaminoglycans, as seen in chapter 2, due to their high negative fixed charge density, draw water within the tissue and tend to swell by a very significant amount, creating a high osmotic pressure responsible for the compressive stiffness of the ground substance. Finally, free interstitial fluid flows in the tissue according to pressure gradients within the porous network, and is a major contributor to the time-dependent properties of the tissue, such as stress-relaxation and creep characteristic times.

The global mechanical response of the cervical stroma is then evaluated as the combination of the individual responses of these three separate elements. The corresponding rheological model is represented in Figure 3-3. The different networks act in parallel. As the collagen network is loaded, its fibers reorient and stretch following the applied deformation, in a manner similar to that of a polymer network, while the contribution of the glycosaminoglycans matrix is dominated by the changes in volume, and the corresponding variations in fixed charge density that controls osmotic pressure and intermolecular electrostatic repulsive forces. The interstitial fluid contributes to the total stress through a dynamic pressure term, controlled by the local changes in volume of the

porous collagen-glycosaminoglycans network.
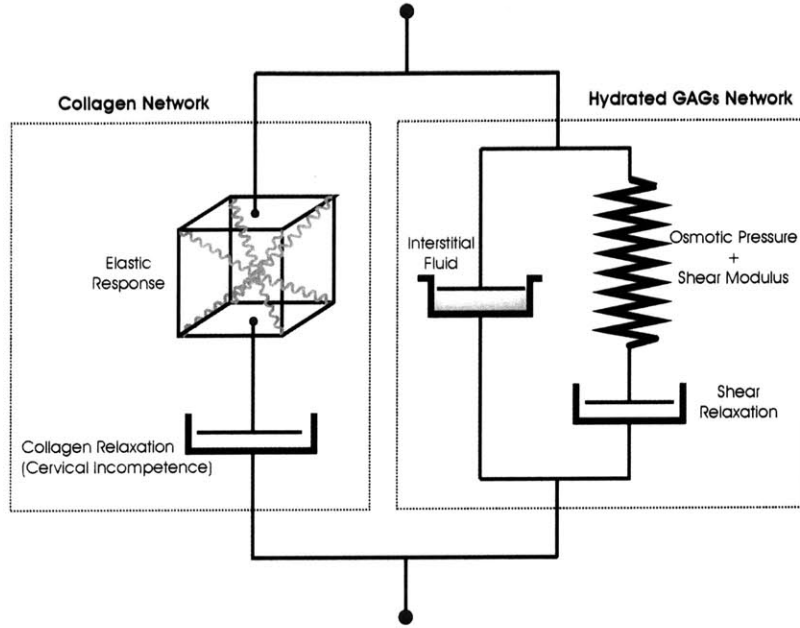
Figure 3-3: Proposed rheological model for the cervical stroma.

The three-dimensional constitutive equations for the model are thus based on the following general assumptions. The deformation gradient is assumed to be the same for both the collagen network and the hydrated GAGs ground substance, and equal to the global deformation experienced by the whole tissue. We have

$$\mathbf{F} = \mathbf{F}_G = \mathbf{F}_C, \tag{3.8}$$

where $\mathbf{F}_G$ is the deformation gradient associated with the glycosaminoglycans network, and $\mathbf{F}_C$ the deformation gradient associated with the collagen network.

The total Cauchy stress developed in the tissue in response to the deformation gradient $\mathbf{F}$ is given by the sum of the stresses developed in each network:

$$\mathbf{T}_{tissue} = \mathbf{T}_C + \mathbf{T}_G - P_{fluid}\mathbf{I}, \tag{3.9}$$

where $\mathbf{T}_C$ and $\mathbf{T}_G$ are the Cauchy stresses in the collagen and glycosaminoglycans networks respectively, P_{fluid} is the interstitial fluid pressure, and $\mathbf{I}$ is the identity tensor.

The proteoglycans network is subject to an osmotic pressure, even when the tissue is not subjected to any exterior loading, and this isotropic pressure stress is balanced by an initial tensile stress in the collagen network. The collagen fibers are thus under a state of isotropic prestretch, even when no external deformation is applied to the tissue (see section 3.3.4).

The following sections will describe the constitutive equations defining the behavior of each network, as well as the equations governing interstitial fluid flow and fluid pressure distribution within the tissue.

3.3   Collagen Network

The collagen ensures the resistance of the tissue in tension. Only the elastic part of its response will be modeled in this first implementation of the model. Figure3-3 shows the presence of a time relaxation component that will be necessary in the modeling of cervical incompetence. However, this first version will only aim at capturing the behavior of healthy, non-pregnant tissue, neglecting time-dependent effects associated with the collagen response.

The assembly of collagen fibers via chemical cross-links give it a network-like structure, as can be seen in Figure 3-4. The fibers of the network deform in response to an externally applied mechanical load in a manner similar as that of a polymer network. Figure 3-4A and 3-4B show the same collagen network respectively in its reference configuration, and under the application of a uniaxial tensile force along the vertical direction. The applied stress results in two distinct effects on the network: individual fibers are stretched, and they rotate to align themselves with the direction of the tensile load, as can be seen for the highlighted fibers in the Figure. These features of the collagen mechanical response will be well captured by classical constitutive models used in rubber elasticity.

Many different types of models have been used to represent the constitutive behavior of rubber-like materials, including continuum mechanics treatments based on the invariants of the deformation, or models derived from statistical mechanics (see [75] for a complete review of the models used in rubber elasticity). A statistically-based model will be used to represent the collagen network of cervical tissue. This type of models for hyperelastic materials rely on two fundamental steps. First, a force-stretch relationship must be defined for the individual chains of the network; second, a simple representative unit structure must be defined to account for the geometry of the network, in order to enable the link between macroscopic deformation variables and the deformation of the individual chains. The following sections will describe in detail the structures adopted for these elements in the case of the cervical collagen.
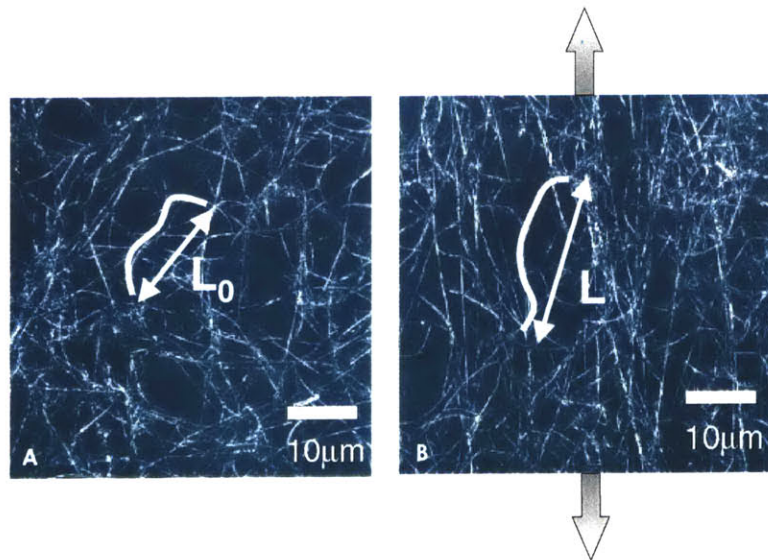
Figure 3-4: Micrograph of a collagen matrix showing stretching and rotation of the fibrils under uniaxial extension. (Modified from Roeder et al [76]).

3.3.1 Individual Chain Force-Stretch Relationship

The force-stretch response of individual collagen fibrils is influenced by their wavy, crimped nature. The initial response to an axial stretching is relatively compliant, dominated by changes in the bending energy associated with the decrimping of the fibril. Further stretching requires stretching of individual covalent bonds, and thus gives rise to a much stiffer response. This type of mechanisms have been investigated by Yannas and Comninou [77], where a sinusoidal waveform about a central axis was adopted to model the geometry of an individual collagen fiber. It appears that the force-extension relationship of a freely jointed molecular chain exhibits the same basic features as that of a collagen fiber, with an initially compliant response followed by a dramatic increase in stiffness after a certain stretch is reached. Although the origin of the stress is different for the two models, the statistical chain model was adopted here to represent the individual collagen fibers, due to its simple formulation and the phenomenological similarities of both responses.

In elastomeric materials, the stress developed in response to deformation primarily originates from the changes in configurational entropy of the individual fibrils [78]. If a fibril is assumed to be constituted by a chain with a certain number of rigid links that can rotate with respect to each other, an increase in length would result in a reduction of the number of possible configurations for the building links of the fibril, and thus lead to a decrease in entropy. This decrease corresponds to an increase of the entropic portion $(-Ts)$ of the free energy, responsible for the observed stress (T is the absolute temperature and s the entropy of the chain). This model leads to simple force-stretch relationships for individual fibrils, based on the number of links per chain, and the statistical model used to represent the possible configurations of a chain at a given length.

Several statistical models have been used to represent chain configurations. The approach adopted by Kuhn and Grühn in 1942 [79] uses Langevin chain statistics, which yields the following expression for the force f developed in a chain in response to a given

stretch λ:

$$f = \frac{k_B T}{b} \mathcal{L}^{-1}\left(\frac{r}{nb}\right) = \frac{k_B T}{b} \mathcal{L}^{-1}\left(\frac{\lambda}{\sqrt{n}}\right), \tag{3.10}$$

where k_B is Boltzmann's constant, T is the temperature, r is the length of the chain, b is the length of a rigid link, n is the number of such links in a chain, and $\mathcal{L}^{-1}$ is the inverse Langevin function defined by

$$\beta = \mathcal{L}^{-1}\left(\frac{r}{nb}\right), \tag{3.11}$$

$$\frac{r}{nb} = \mathcal{L}(\beta) = \coth\beta - \frac{1}{\beta}. \tag{3.12}$$

The fully extended length of a chain is nb, and the average initial length of a chain is given by $\sqrt{n}b = l_0$. The stretch λ is consequently given by $\lambda = \frac{r}{l_0} = \frac{r}{\sqrt{n}b}$. Finally, the limiting or locking stretch corresponds to $\lambda_L = \sqrt{n}$. Figure 3-5 shows the force-stretch relationship defined by equation (3.10) for different values of the locking stretch λ_L.

As can be noticed on the curves, the chains appear to be very stiff in tension, and flexible in compression.

3.3.2 Representative Network Structure

The second step in the modelization consists in defining an average representative structure for the network, in order to establish a link between the individual chains response and the global deformation. The most common approach to this problem is to assume the network to be represented by a unit cell that deforms with the principal stretches of the deformation. The representative chain configuration we assumed in the unit cell is based on the model originally proposed by Arruda and Boyce [80], defined by a cubic unit cell with 8 individual chains connected at the center (see Figure 3-6).

The cell deforms with the principal stretches. The symmetry of the cell is such that the junction point remains at the center during the whole deformation, and all the chains

71
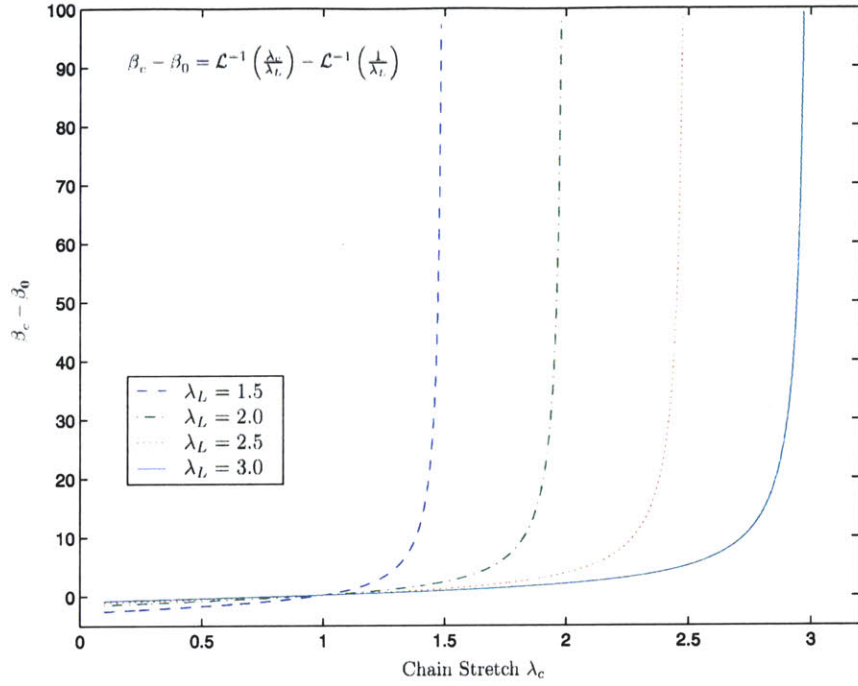
Figure 3-5: Force-stretch relationship for a Langevin chain, for different values of the locking stretch λ_L.

experience the same level of stretch, given by

$$\lambda_c = \sqrt{\frac{\lambda_1^2 + \lambda_2^2 + \lambda_3^2}{3}}, \tag{3.13}$$

where λ_1, λ_2 and λ_3 are the principal stretches. This model was shown to successfully capture the behavior of many different elastomeric materials [80]. In addition to having the same stretch, the chains rotate towards the directions of highest stretch, as can be seen in Figure 3-7. This captures the effect of network orientation produced by the applied deformation.
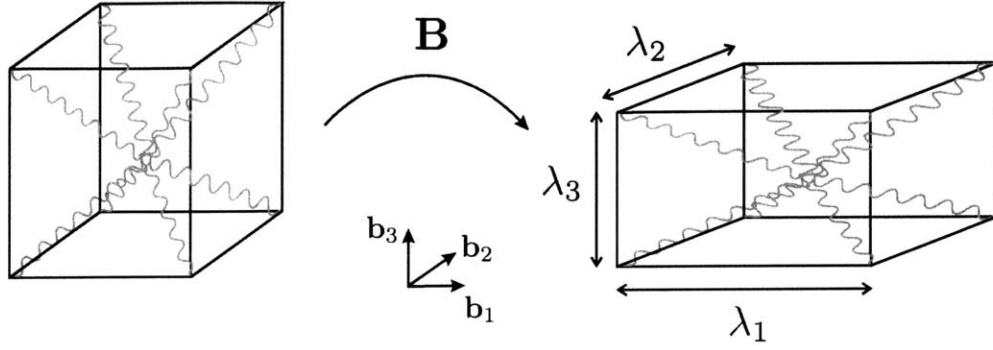
$$\mathbf{B} = \mathbf{F}\mathbf{F^T} = \lambda_1^2 \mathbf{b}_1 \otimes \mathbf{b}_1 + \lambda_2^2 \mathbf{b}_2 \otimes \mathbf{b}_2 + \lambda_3^2 \mathbf{b}_3 \otimes \mathbf{b}_3$$

Figure 3-6: The 8-fibril unit cell. The cell is taken to deform along the principal directions of the left Cauchy-Green stretch , with stretches equal to the principal stretches.

3.3.3 Stress-Strain Constitutive Behavior

The eight-fibril network, together with the force-stretch relationship used to represent the behavior of a collagen fibril, can be integrated to derive a full 3-dimensional stress-strain relationship for the collagen network. This can be done by calculating the strain energy density associated with this representative structure. The hyperelastic strain energy density of the whole network, W_{Col}, can be calculated as the strain energy of a single collagen fibril w_{fibril}, multiplied by the density of fibrils in the network N:

$$W_{Col} = N w_{fibril}, \tag{3.14}$$

with the strain energy of an individual fibril given by

$$w_{fibril} = \int f_{fibril} dl_{fibril} = \int f_{fibril} l_0 d\lambda_{fibril}, \tag{3.15}$$

where the fibril stretch λ_{fibril} is related to the principal stretches λ_i by equation (3.13), and the corresponding fibril force f_{fibril} is defined by equation (3.10). Integration yields
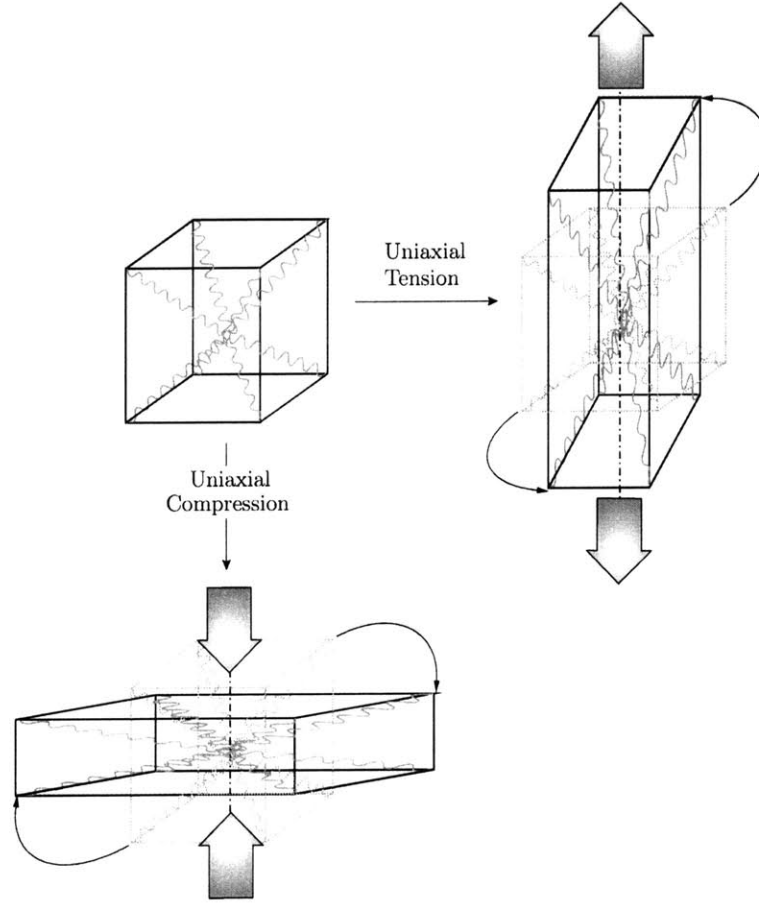
Figure 3-7: Deformation of the 8-fibril unit cell in uniaxial compression and uniaxial extension. The chains rotate towards the direction of stretch in uniaxial extension, and away from the axis in compression.

the following expression for the strain energy density:

$$W_{Col} = Nk_B T\lambda_L \left[\beta_{fibril}\lambda_{fibril} + \lambda_L \ln\left(\frac{\beta_{fibril}}{\sinh\beta_{fibril}}\right) + \frac{\beta_0}{3}\ln\frac{1}{J}\right], \qquad (3.16)$$

where

$$\beta_{fibril} = \mathcal{L}^{-1}\left(\frac{\lambda_{fibril}}{\sqrt{n}}\right) = \mathcal{L}^{-1}\left(\frac{\lambda_{fibril}}{\lambda_L}\right) \qquad ; \qquad \beta_0 = \mathcal{L}^{-1}\left(\frac{1}{\lambda_L}\right)$$

and J is the volumetric Jacobian defined by $J = \lambda_1\lambda_2\lambda_3$. The third term of equation 3.16 $(\beta_0 \ln\frac{1}{J})$ has been introduced to account for the small contribution of internal energy,

which prevents entropic collapse of the network, and ensures zero stress in the absence of deformation.

The associated Cauchy stress $\mathbf{T_C}$ is then obtained by differentiation of the strain energy density with respect to the invariants of the left Cauchy-Green stretch tensor $\mathbf{B}$:

$$\mathbf{T_C} = \frac{2}{J}\frac{\partial W_{Col}}{\partial I_1}\mathbf{B} + \frac{\partial W_{Col}}{\partial J}\mathbf{I} \tag{3.17}$$

$$\mathbf{B} = \mathbf{F}\mathbf{F^T} \qquad I_1 = tr\mathbf{B} = \lambda_1^2 + \lambda_2^2 + \lambda_3^2 \qquad J = det\mathbf{F} = \sqrt{det\mathbf{B}} = \lambda_1\lambda_2\lambda_3$$

as W_{Col} is not taken to depend on the second stretch invariant I_2. By differentiation, the following expression is obtained for the stress $\mathbf{T_C}$:

$$\mathbf{T_C} = \frac{Nk_BT\lambda_L}{3}\frac{1}{J}\left[\frac{\beta_{fibril}}{\lambda_{fibril}}\mathbf{B} - \beta_0\mathbf{I}\right] \tag{3.18}$$

Finally, a linear bulk corrective term can be added to the stress to account for additional energetic contributions to the strain energy density:

$$\mathbf{T_C} = \frac{Nk_BT\lambda_L}{3}\frac{1}{J}\left[\frac{\beta_{fibril}}{\lambda_{fibril}}\mathbf{B} - \beta_0\mathbf{I}\right] + K_C\left(J - 1\right)\mathbf{I} \tag{3.19}$$

The model relies on the three following material constants:

- the quantity $\frac{Nk_BT\lambda_L}{3}$, equivalent to an "initial shear modulus",

- the limiting stretch $\lambda_L = \sqrt{n}$ for the collagen fibrils,

- and the additional linear bulk modulus K_C.

The 8-chain model has been used by several investigators to model the collagen network of other soft tissues such as articular cartilage [81], and skin [82]. In the first study, the constitutive parameters of the model were fit to the data of Basser et al [83], characterizing the isotropic stress-isotropic stretch behavior of the collagen network in human articular cartilage using an osmotic stress technique. The tensile stress in the

75

collagen network could be calculated for different levels of hydration as the difference between the osmotic pressure of the proteoglycans (known from measurements obtained with solutions of proteoglycans extracted from human cartilage), and the applied osmotic stress. The 8-chain model could successfully reproduce the volumetric stress- volumetric stretch behavior of the cartilage collagen network. Unfortunately, such data is not yet available for cervical stroma. The constitutive parameters of the collagen network were thus fit to data obtained from tests realized on cylindrical cervical samples in confined and unconfined compression. One of the long-term objectives of the study is to characterize relationships between the values obtained for these constants, and biochemical measurements on the same samples such as collagen content or extractability.

3.3.4   Influence of the Collagen Prestretch

The study by Basser et al [83] underlined the importance of the initial collagen stretch balancing the GAGs osmotic pressure (in the unloaded equilibrium configuration), that had been noted by different investigators in the past ([84], [85], [86], [87], [88]), but often neglected in the models. The response of cartilage tissue in compression was considered to come primarily from the proteoglycans osmotic pressure. However, this prestretch brings the collagen fibers in the transition zone between the compliant and stiff parts of the fibril response, meaning that the collagen network plays a significant role in the macroscopic response of the tissue to compressive loads, at least in the small stretch range. This also enables to increase the resistance to the tissue in tension, since further stretching of the collagen would give rise to very high fiber tension (see Figure 3-8). Similar findings may be expected for the influence of the collagen pre-stretch on the behavior of cervical tissue.

3.3.5   Effects of Fiber Orientation

The representative 8-fibril network chosen in this preliminary model assumes isotropic properties for the collagen network in cervical tissue. This is certainly an idealization of the real material structure, and several investigators have noted the existence of different
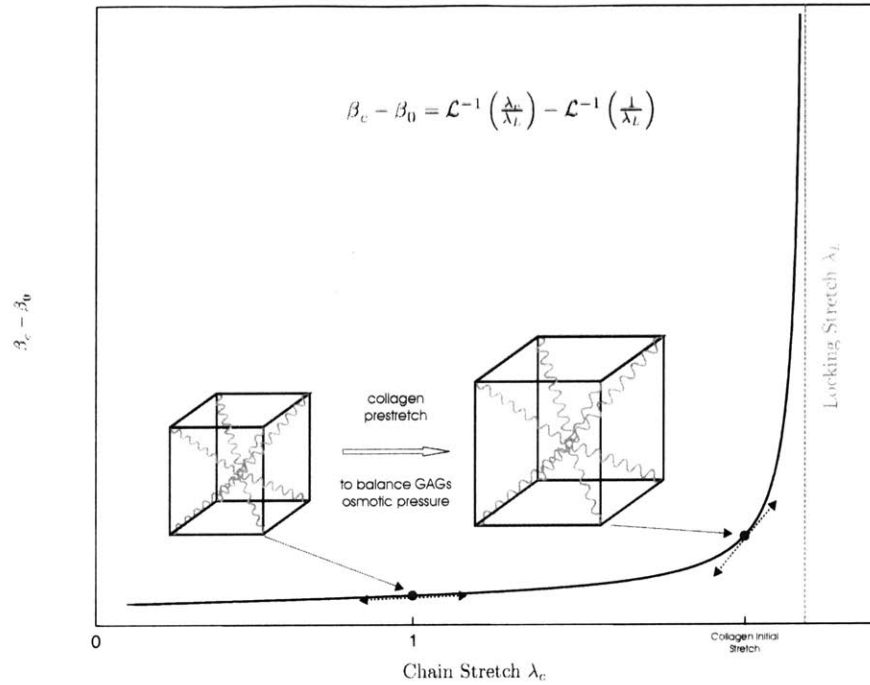
Figure 3-8: Influence of the collagen prestretch on the fibrils force-stretch response.

macroscopic fiber orientations in different zones of the tissue for the rat cervix [89], and also for human tissue [72]. Three main zones are described, going from the endocervical canal to the outer diameter. The fibers are described as being oriented along the axis of the cervix in the inner and outer zones, and circumferentially oriented within the smooth muscle cells layers in the middle zone. However, as mentioned in chapter 2, histologic studies of human non-pregnant specimens have not enabled us to identify marked features of anisotropy for the collagen network. This is also validated by the study from Petersen et al [70], which noted no significant difference in the tensile properties of circumferential and longitudinal specimens.

This justifies the choice of an isotropic unit cell in this first version of the model. Nevertheless, if additional studies revealed specific fiber orientation patterns, these could be incorporated in the model by using unit cells with different aspect ratios according to the different zones of the tissue, but same chain length, in order to model the preferred

orientation of the collagen fibrils. This approach has already been successfully implemented by Bischoff and Arruda [82], in the constitutive model they developed for skin tissue.

3.4 Glycosaminoglycans Network

The equilibrium response of the proteoglycans network is associated with the osmotic pressure resulting from their negative fixed charge density (see chapter 2). The osmotic pressure of the glycosaminoglycans of articular cartilage has been widely investigated over the past few decades, and the amount of experimental data relating GAGs fixed charge density to osmotic pressure is extensive. Most of the expressions obtained to relate these quantities are based on linear regression of experimental measurements, however several investigators have described in detail the electromechanical interactions between GAG chains and ionic species within the tissue, proposing theoretical expressions for the osmotic pressure as a function of tissue volume, fixed charge density, and ionic strength of the bathing fluid ([90], [91]). This approach enables to make the link between equilibrium properties and microstructural features of the proteoglycans network in articular cartilage, and to understand better the mechanisms involved in certain alterations of tissue function. The approach adopted here to model the glycosaminoglycans network of cervical tissue will be mainly based on these results.

The rheological model adopted for the GAGs network is illustrated in Figure 3-9. It is composed of both an elastic part (including the equilibrium osmotic pressure and a shear modulus), and a viscous component accounting for time-dependent non-equilibrium effects of relative sliding between GAG chains.

The association in series of the two elements of the model leads to the following decomposition of the deformation gradient and stress associated with the network. The imposed deformation gradient $\mathbf{F}_G$ is multiplicatively decomposed into a flow part asso-
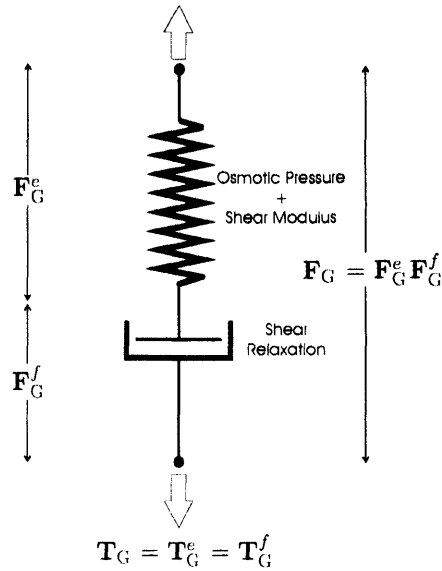
Figure 3-9: Rheological model for the glycosaminoglycans network.

ciated with the viscous element, and an elastic part associated with the elastic element:

$$\mathbf{F}_G = \mathbf{F}_G^e \mathbf{F}_G^f. \tag{3.20}$$

The Cauchy stress is identical in both elements of the model:

$$\mathbf{T}_G = \mathbf{T}_G^e = \mathbf{T}_G^f. \tag{3.21}$$

3.4.1 Osmotic Pressure of the GAGs Matrix

The osmotic pressure of the proteoglycans network is controlled by the intermolecular electrostatic repulsion forces between adjacent GAG chains, and their influence on the ionic distribution within the interstitial fluid. An externally imposed decrease in volume causes an increase in the fixed charge density, thus increasing repulsive forces between GAG molecules. This is the physical origin of the resistance of soft tissues to compres-

sive loads. This effect has been analyzed in terms of a Donnan equilibrium pressure [93], however such a model ignores the details of the microstructure of the tissue, and by that the intimate mechanisms that control osmotic pressure in both functional and dysfunctional tissue. Buschmann and Grodzinsky [90] proposed a different approach to model the dependency of the osmotic pressure of proteoglycans in cartilage on the characteristics of the microstructure, where the Poisson-Boltzmann equation is used to characterize the ionic distribution within the solvent, while GAG molecules are treated as uniformly charged cylinders. Ehrlich et al [94] used an approach similar to the one proposed by Buschmann and Grodzinsky to theoretically model the osmotic pressure of chondroitin sulfate solutions, which compared successfully with their experimental data obtained for solutions of different fixed charge density and ionic strength.

This approach is based on the representation of the tissue as an array of repetitive cylindrical unit cells composed of a central charged rod (corresponding to a GAG chain), and its fluid environment (see Figure 3-10). The dimensions of the cell, as well as the surface charge on the rod and ionic strength of the fluid, are related to the real parameters of the tissue, and the Poisson-Boltzmann equation is then solved numerically to determine the ionic distribution within the fluid as a function of radial distance from the center of the unit cell. The osmotic pressure at the outer boundary of the cell can then be calculated, and provides an estimate of the effective osmotic pressure within the tissue relative to that of the bathing solution. The main steps will be outlined here. The reader is referred to the work by Buschmann and Grodzinsky [90] for a complete description of the PB-cell model.

The equations are written for the case of a 1:1 electrolyte such as sodium chloride NaCl, and ions are assumed to be point charges. The electric field $\mathbf{E}$ within the fluid in the PB-cell is subject to Gauss' law, which in the case of a homogeneous medium is

$$\nabla.\mathbf{E} = \frac{\rho}{\epsilon}, \tag{3.22}$$

where ρ is the charge density, and ϵ is the dielectric permittivity of the fluid. The field
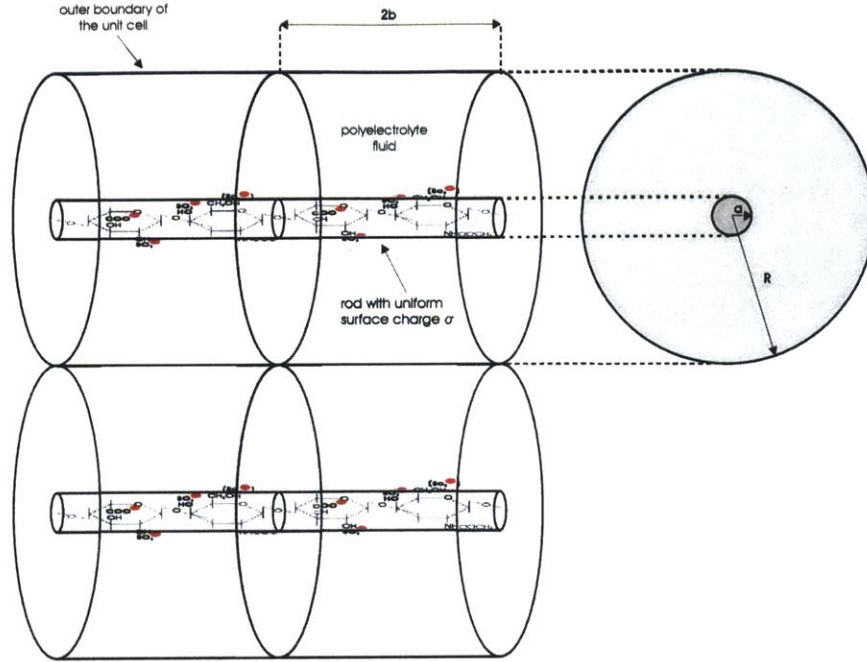
Figure 3-10: Schematic representation of the Poisson-Boltzmann unit cell. The GAG chains are modeled as uniformly charged rods located at the center of a cylindrical fluidic cell. Each cell contains one disaccharide unit (2 charged monomers, here dermatan sulfate).

is conservative in this case, as no time varying magnetic fields are present ($\nabla \times \mathbf{E} = 0$), and can be expressed as the gradient of an electric potential ϕ:

$$\mathbf{E} = -\nabla\phi. \tag{3.23}$$

The combination of equations (3.22) and (3.23) yields Poisson's equation for the electric potential:

$$\nabla^2\phi + \frac{\rho}{\epsilon} = 0. \tag{3.24}$$

The ions are assumed to follow a Boltzmann distribution:

$$C^{\pm}(r) = C_0 \exp\left(\frac{\mp \mathcal{F}\phi(r)}{\mathcal{R}T}\right), \tag{3.25}$$

where $C^{\pm}(r)$ is the concentration of the positive or negative ions as a function of radial

distance, C_0 is the ionic strength of the bath, $\mathcal{F}$ is Faraday's constant and $\mathcal{R}$ is the gas constant. The charge density within the fluid is given by $\rho = \mathcal{F}\left(C^+(r) - C^-(r)\right)$, which combined with (3.24) and (3.25) gives the Poisson-Boltzmann equation for the potential:

$$\nabla^2 \phi(r) - \frac{2\mathcal{F}C_0}{\epsilon}\sinh\left(\frac{\mathcal{F}\phi(r)}{\mathcal{R}T}\right) = 0. \tag{3.26}$$

The associated boundary conditions are

$$\begin{cases} r = a: & \frac{d\phi}{dr} = -\frac{\sigma}{\epsilon} \\ r = R: & \frac{d\phi}{dr} = 0 \end{cases}, \tag{3.27}$$

where σ is the uniform surface charge on the GAG cylinders calculated as

$$\sigma = -\frac{e}{2\pi ab}. \tag{3.28}$$

e is the elementary charge ($e = 1.6 \times 10^{-19}$ C), a and b are geometric parameters related to the unit cell as defined in Figure 3-10 (a being the radius of an individual GAG chain, b the intercharge distance along a chain), and R the radius of the cell based on the concentration of GAGs present in the tissue (following equation (3.33)). This equation is normalized by introducing the variables $\xi = r\kappa$ and $\psi = \frac{\mathcal{F}\phi(r)}{\mathcal{R}T}$, where κ is the inverse Debye length $\kappa = \sqrt{\frac{2\mathcal{F}^2 C_0}{\epsilon \mathcal{R}T}}$:

$$\nabla^2 \psi(\xi) - \sinh\psi = \frac{d^2\psi}{d\xi^2} + \frac{1}{\xi}\frac{d\psi}{d\xi} - \sinh\psi = 0, \tag{3.29}$$

with boundary conditions

$$\begin{cases} \xi = a\kappa: & \frac{d\psi}{d\xi} = -\frac{\mathcal{F}\sigma}{\kappa\mathcal{R}T\epsilon} \\ \xi = R\kappa: & \frac{d\psi}{d\xi} = 0 \end{cases}. \tag{3.30}$$

This equation can then be solved numerically [90], or the potential can be approximated by a hybrid solution as suggested by Katchalsky et al [95]. The equation is approximated

in the short radial distance range $\left(r < \frac{1}{\kappa}\right)$ where the contribution of the negative ions can be neglected, and the long radial distance $\left(r > \frac{1}{\kappa}\right)$, where thermal energy dominate over the electric field-ions interaction energy, and equation (3.29) can be linearized. The details of the derivation are omitted here, and the reader is referred to Katchalsky et al [95] for a complete treatment. The two solutions obtained are then matched for a transition radius in the midrange. Using (3.25), the osmotic pressure can be calculated as

$$\Pi_{os} = \mathcal{R}T\left[C^+(R) + C^-(R) - 2C_0\right] = 2\mathcal{R}TC_0\left[\cosh\psi(R) - 1\right]. \qquad (3.31)$$

Using a transition radius of about two Debye screening lengths $d \approx \frac{2}{\kappa}$, Kovach [91] obtained the following expression for the osmotic pressure of the GAGs:

$$\Pi_{os} = 2\mathcal{R}TC_0\left[\cosh\left(\frac{A\exp\left(-R\kappa\right)}{\sqrt{R\kappa}}\right) - 1\right], \qquad (3.32)$$

where A is an integration constant. The dependence of the osmotic pressure on the changes in volume is encapsulated in the associated variation of the radius R of the PB-unit cell. R is determined from the concentration of glycosaminoglycans in the tissue according to

$$V_{Cell} = 2\pi bR^2 = \frac{M_0}{gN_A}, \qquad (3.33)$$

or equivalently

$$R = \sqrt{\frac{M_0}{2\pi bgN_A}}, \qquad (3.34)$$

where M_0 is the mass of a mole of disaccharide units in g/mol, g is the concentration of GAGs in the tissue in g/m^3, and N_A is Avogadro's number. By fitting equation (3.32) to the data of Maroudas and Bannon [96], and the numerical results of Buschmann and Grodzinsky [90], Kovach found for the constant A an optimal value of $A \approx 9.1$ in both cases [91], for realistic GAG chain structural parameters ($a = 0.55$ nm and $b = 0.64$ nm for chondroitin sulphate). The present model uses equation (3.32) with $A = 9.1$ to account for the variations of glycosaminoglycans osmotic pressure with deformation. The

elastic volumetric Jacobian $J^e = det\mathbf{F}^e$ of the transformation is related to R via:

$$J^e = \frac{V_{Cell}}{V_{Cell}^0} = \left(\frac{R}{R^0}\right)^2,\tag{3.35}$$

with $R^0 = \sqrt{\frac{M_0}{2\pi b g^0 N_A}}$. Equation (3.48) implies $J^e = J = det\mathbf{F}$, and combining (3.32) with (3.35), we obtain for the osmotic pressure the final expression

$$\Pi_{os} = 2\mathcal{R}TC_0 \left[\cosh\left(\frac{A\exp\left(-\kappa R^0 J^{1/2}\right)}{\sqrt{\kappa R^0}J^{1/4}}\right) - 1\right].\tag{3.36}$$

This expression is plotted as a function of the material Jacobian J in Figure 3-11. The constant $\Pi_1 = 2\mathcal{R}TC_0$ was calculated for $C_0 = 154$ mmol/l, which corresponds to the concentration of the NaCl buffer used in the experiments described in chapter 5. The different curves correspond to different values of the adjusTable parameter $\Pi_2 = \kappa R^0$, which depends on the initial GAGs concentration in the tissue, g^0.

3.4.2 Shear Resistance

Recent experimental data from cartilage tissue [97] demonstrate a contribution of the proteoglycans network to the dynamic shear stiffness of the composite tissue. In this study, Grodzinsky and Jin propose a molecular model to account for this contribution, based on the same Poisson-Boltzmann unit cell concept described in the previous section. The effect of the shear deformation on the unit cells is modeled as a transformation of the circular section of the cylindrical unit cells to an elliptic section. Such a deformation affects the solution for the electric potential, and consequently the ionic concentrations and the osmotic pressure at the cell outer boundary, which loses its cylindrical symmetry. This effect generates a force opposed in direction to the shear deformation.

This molecular approach was not incorporated in the present constitutive model, to keep it reasonably simple and avoid the multiplication of constitutive parameters. The shear resistance was accounted for in terms of a simple linear elastic shear modulus μ_G,
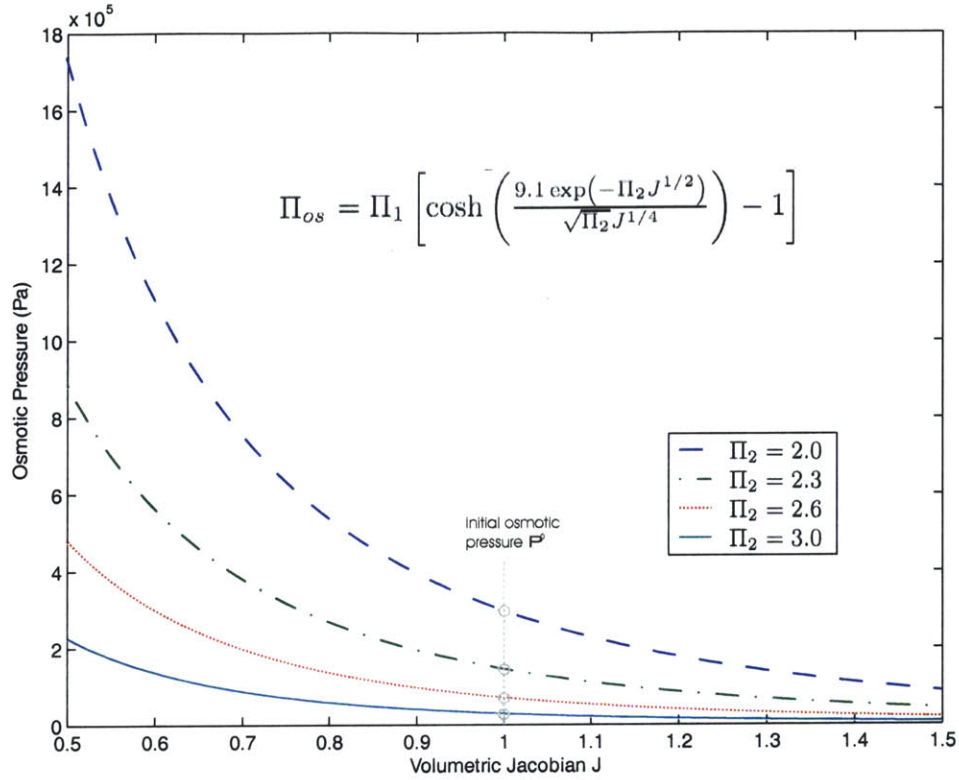
Figure 3-11: Osmotic pressure Π_{os} versus volumetric Jacobian J (3.36), for different values of the initial GAGs concentration g^0 (in NaCl, $C_0 = 154$ mmol/l).

and a linear viscous term described in section 3.4.3. The elastic response of the GAGs network is thus modeled by the osmotic pressure term together with a linear elastic shear modulus, such that the associated Cauchy stress can be written as

$$\mathbf{T}_G = \frac{1}{J}\left[2\mu_G \mathbf{E}_G^e - \frac{2\mu_G}{3}(tr\mathbf{E}_G^e)\mathbf{I}\right] - \Pi_{os}\mathbf{I}, \tag{3.37}$$

where the value for the second elastic modulus $\lambda_G = -\frac{2\mu_G}{3}$ corresponds to a bulk modulus $K_G = 0$, consistent with the assumption that the volumetric part of the response is fully accommodated by the osmotic pressure. $\mathbf{E}_G^e$ is the Henky strain associated with the

85

elastic deformation gradient, defined by

$$\mathbf{E}_G^e = \ln \mathbf{V}_G^e = \frac{1}{2} \ln \mathbf{B}_G^e = \frac{1}{2} \ln \mathbf{F}_G^e \mathbf{F}_G^{e\mathbf{T}}, \tag{3.38}$$

where $\mathbf{B}_G^e$ is the left Cauchy-Green stretch associated with the elastic deformation gradient $\mathbf{F}_G^e$.

Equation (3.37) together with (3.36) fully characterize the elastic response of the glycosaminoglycans network.

3.4.3 Shear Relaxation

The viscous element of the GAGs network corresponds to time-dependent viscous forces developed as GAG chains slide past one another in shear motion, therefore the deformation associated with flow is constrained to remain isochoric ($det\mathbf{F}_G^f = 1$ throughout the whole deformation process).

The velocity gradient corresponding to the imposed deformation on the GAGs network is

$$\mathbf{L} = \dot{\mathbf{F}}\mathbf{F}^{-1} = (\overset{\bullet}{\widehat{\mathbf{F}_G^e \mathbf{F}_G^f}})(\mathbf{F}_G^e \mathbf{F}_G^f)^{-1} = (\dot{\mathbf{F}}_G^e \mathbf{F}_G^f + \mathbf{F}_G^e \dot{\mathbf{F}}_G^f)\mathbf{F}_G^{f-1}\mathbf{F}_G^{e-1}, \tag{3.39}$$

The contributions of the elastic and flow parts of the deformation can then be separated as

$$\mathbf{L} = \underbrace{\dot{\mathbf{F}}_G^e \mathbf{F}_G^{e-1}}_{\mathbf{L}_G^e} + \underbrace{\mathbf{F}_G^e \dot{\mathbf{F}}_G^f \mathbf{F}_G^{f-1} \mathbf{F}_G^{e-1}}_{\tilde{\mathbf{L}}_G^f} = \mathbf{L}_G^e + \tilde{\mathbf{L}}_G^f. \tag{3.40}$$

The flow contribution to the velocity gradient is separated in its skew and symmetric parts, which need to be constitutively prescribed:

$$\tilde{\mathbf{L}}_G^f = \tilde{\mathbf{D}}_G^f + \tilde{\mathbf{W}}_G^f. \tag{3.41}$$

The plastic spin can be prescribed to be zero to ensure uniqueness of the decomposition as proposed by Boyce et al in the case of a constitutive model for polyethylene terephtalate

[92]. The plastic rate of stretching is prescribed as being proportional to the deviatoric stress $\mathbf{T}'_G$ in the GAGs network:

$$\begin{cases} \tilde{\mathbf{W}}^f_G & = & 0 \text{ (no spin)} \\ \tilde{\mathbf{D}}^f_G & = & \dot{\gamma}^f \mathbf{N}_G \end{cases} \tag{3.42}$$

where $\mathbf{N}_G$ is the tensorial direction of $\mathbf{T}'_G$, given by

$$\mathbf{N}_G = \frac{1}{\sqrt{2}\tau_G} \mathbf{T}'_G \qquad \tau_G = \sqrt{\frac{1}{2}\mathbf{T}'_G : \mathbf{T}'_G}, \tag{3.43}$$

and $\mathbf{T}'_G$ is the deviatoric Cauchy stress

$$\mathbf{T}'_G = \mathbf{T}_G - \frac{1}{3}(tr\mathbf{T}_G)\mathbf{I}. \tag{3.44}$$

The flow strain rate coefficient $\dot{\gamma}^f$ needs to be constitutively prescribed for the response of the viscous element of the model to be fully characterized. The underlying physical mechanisms involved in the plastic flow are frictional in nature, coming from interactions between adjacent GAG chains as well as from friction forces between GAG chains and collagen fibrils or interstitial water. In a first attempt to model this time dependent behavior, we adopted a linear relationship between the deviatoric stress $\mathbf{T}'_G$ and the rate of stretching associated with the flow. This leads to an expression for $\dot{\gamma}^f$ of the form

$$\dot{\gamma}^f = \dot{\gamma}_0 \tau_G, \tag{3.45}$$

where $\dot{\gamma}_0$ is a constant parameter to be fit to the data.

This formulation automatically satisfies the isochoric constraint on the flow part of the deformation gradient, where $det\mathbf{F}^f_G = 1$. Indeed this is due to the deviatoric nature

of the flow velocity gradient $\tilde{\mathbf{D}}_G^f$:

$$\begin{cases} det\mathbf{F}_{G|t=0}^f = det\mathbf{I} = 1 \\ \frac{\partial det\mathbf{F}_G^f}{\partial t} = tr\left(\dot{\mathbf{F}}_G^f \mathbf{F}_G^{f-1}\right) det\mathbf{F}_G^f \end{cases}, \tag{3.46}$$

but we have

$$tr\left(\dot{\mathbf{F}}_G^f \mathbf{F}_G^{f-1}\right) = tr\tilde{\mathbf{D}}_G^f = \frac{\dot{\gamma}_0}{\sqrt{2}}tr\mathbf{T}_G' = 0, \tag{3.47}$$

thus implying

$$\forall t, \qquad det\mathbf{F}_{G|t}^f = 1. \tag{3.48}$$

All the volumetric effects of deformation are accommodated by the elastic component of the two-element model, which include osmotic pressure effects.

3.5 Interstitial Fluid Flow

3.5.1 Darcy's Law

The last component of the response relates to the modelization of the interstitial fluid flow, which accounts for a large portion of the time-dependent effects in the tissue mechanical response. The framework adopted here is based on the simple assumption of a flow governed according to a linear Darcy's law [98]. The origin of the viscous effects lies in the frictional drag between the flowing fluid and the hydrated porous matrix (composed of the PGs, HA, and collagen). These fluid-fibrillar matrix interactions are the physical source of the pressure drop developed in the fluid in response to flow, as represented by the proportionality between pressure gradient and macroscopic flow rate in Darcy's law:

$$\mathbf{q} = -k_D \boldsymbol{\nabla} P_{fluid}, \tag{3.49}$$

where $\mathbf{q}$ is the macroscopic volume flow rate, k_D is Darcy's hydraulic permeability coefficient, and P_{fluid} is the dynamic interstitial fluid pressure. Equation (3.49) corresponds

to the simple case of an isotropic material in which no particular orientation within the matrix facilitates or prevents flow relatively to the others. This law is linear, and doesn't account for any variations of the permeability coefficient with the pressure gradient, or the state of deformation. Nevertheless, it enables a simple three dimensional treatment of the transient flow and associated pressure variations, and has been shown to satisfactorily model the interstitial flow of articular cartilage or other connective tissues under physiological loading conditions.

3.5.2 Governing Equation for the Dynamic Fluid Pressure

To establish the equations governing the time variations of the dynamic interstitial pressure, let us consider a small material volume V in the current configuration of the tissue, and its deformation over a short increment of time Δt (see Figure 3-12). The volume
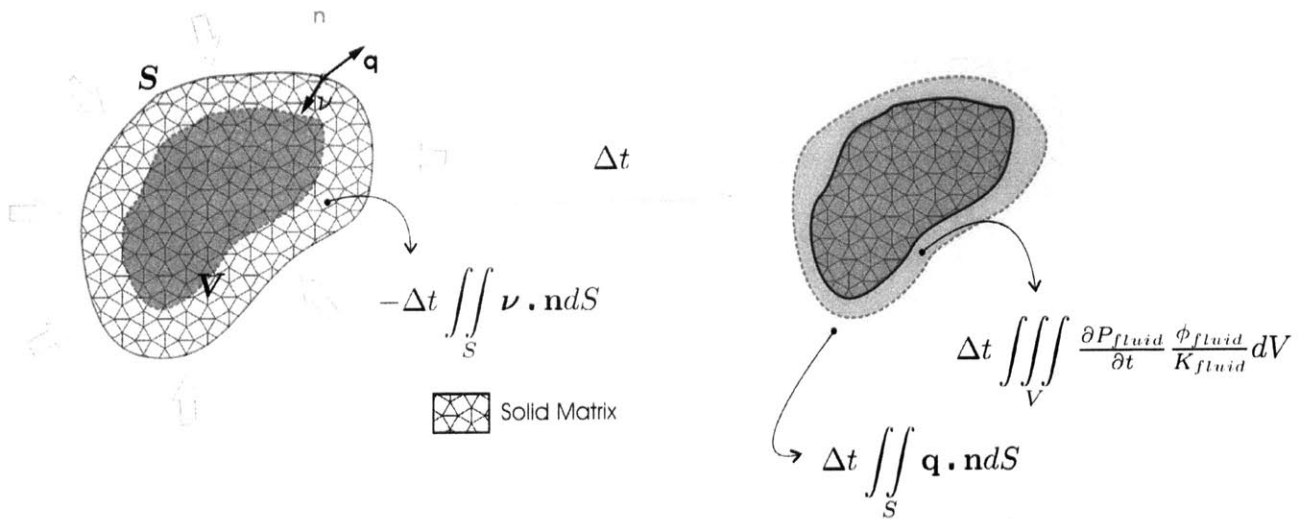
Figure 3-12: Evolution of a volume of tissue in the current configuration over a short time interval Δt, and associated interstitial fluid balance.

of fluid coming in per unit time must be equal to the total increase in volume of V per unit time, plus a second term accounting for the volume reduction of the fluid previously contained in V, governing the increase in the local dynamic pressure. This balance is

expressed by equation (3.50), where ν is the velocity of the solid matrix, ϕ_{fluid} is the fluid volume fraction, and K_{fluid} its bulk modulus:

$$-\underbrace{\iint_S \mathbf{q} \cdot \mathbf{n}dS}_{\substack{\text{1.Volume of fluid} \\ \text{coming in per unit time}}} = \underbrace{\iint_S \boldsymbol{\nu} \cdot \mathbf{n}dS}_{\substack{\text{2.Total increase in volume per unit} \\ \text{time characterized by the} \\ \text{expansion of the porous matrix}}} + \underbrace{\iiint_V \frac{\partial P_{fluid}}{\partial t} \frac{\phi_{fluid}}{K_{fluid}} dV}_{\substack{\text{3.Variation of fluid volume per unit} \\ \text{time accommodated through its} \\ \text{bulk modulus } K_{fluid}}}, \qquad (3.50)$$

where the bulk response of the molecular network is neglected.

(i) Using Darcy's law (3.49) in integral 1 to express the fluid volume flow rate at the outer boundary of the material volume, and using the divergence theorem, we obtain

$$-\iint_S \mathbf{q} \cdot \mathbf{n}dS = \iint_S k_D \boldsymbol{\nabla} P_{fluid} \cdot \mathbf{n}dS = k_D \iiint_V \nabla^2 P_{fluid} dV, \qquad (3.51)$$

assuming a uniform Darcy's hydraulic permeability k_D.

(ii) Using the divergence theorem, integral 2 can be expressed as

$$\iint_S \boldsymbol{\nu} \cdot \mathbf{n}dS = \iiint_V \boldsymbol{\nabla} \cdot \boldsymbol{\nu}dV = \iiint_V tr\mathbf{L}dV = \iiint_V tr\mathbf{D}dV, \qquad (3.52)$$

where $\mathbf{L}$ is the velocity gradient tensor associated with the solid matrix, related to the global deformation gradient $\mathbf{F}$ through $\mathbf{L} = \dot{\mathbf{F}}\mathbf{F}^{-1}$. $\mathbf{D}$ is the global rate of stretching, equal to the symmetric part of $\mathbf{L}$.

Finally, using (3.51) and (3.52) in (3.50), we obtain the following integral equation:

$$\iiint_V \left[k_D \nabla^2 P_{fluid} - tr\mathbf{D} - \frac{\phi_{fluid}}{K_{fluid}} \frac{\partial P_{fluid}}{\partial t} \right] dV = 0. \qquad (3.53)$$

Introducing the coefficient $\chi_{fluid} = \frac{\phi_{fluid}}{K_{fluid}}$, we obtain the following local equation for the time evolution of the interstitial fluid pressure:

$$\chi_{fluid}\frac{\partial P_{fluid}}{\partial t} = k_D \nabla^2 P_{fluid} - tr\mathbf{D}. \tag{3.54}$$

This equation is analogous to a heat diffusion equation, although the corrected compressibility χ_{fluid} accounts for local changes in the fluid volume fraction of the tissue, and varies with time. This variation has been neglected in this preliminary model, and we used the analogy with the heat transfer problem using a constant and uniform thermal conductivity in the numerical implementation.

This completes the set of constitutive equations characterizing the tissue. Figure 3-13 summarizes the main equations and constitutive parameters associated with each part of the model.

Complete details about the finite element implementation of the equations can be found in Appendix A. The next chapter will provide results from experimental testing of cervical samples, and comparison of these experimental findings with results of numerical simulations using our model.

$$\mathbf{F} = \mathbf{F}_G = \mathbf{F}_C$$
$$\mathbf{T}_{tissue} = \mathbf{T}_C + \mathbf{T}_G - P_{fluid}\mathbf{I}$$

$\mathbf{T}_{tissue}$

$\mathbf{T}_C$

$- P_{fluid}\mathbf{I}$ $\mathbf{T}_G$

$[\Pi_2, \mu_G]$

$\mathbf{F}_G^e$

$\mathbf{F}_C$

$[k_D, \chi_{fluid}]$

$\left[\frac{Nk_BT}{3}, \lambda_L, K_C\right]$

$\mathbf{F}_G$

$\mathbf{F}_G^f$

$[\dot{\gamma}_0]$

Collagen Network

Hydrated GAGs Network

$$\mathbf{T}_C = \frac{Nk_\mu T\lambda_L}{3}\frac{1}{J}\left[\frac{\beta_{fibril}}{\lambda_{fibril}}\mathbf{B}_C - \beta_0\mathbf{I}\right] + K_C(J-1)\mathbf{I}$$

$$\mathbf{F}_G = \mathbf{F}_G^e\mathbf{F}_G^f$$
$$\mathbf{T}_G = \mathbf{T}_G^f = \mathbf{T}_G^e$$
$$\mathbf{T}_G^e = \frac{1}{J}\left[2\mu_G\mathbf{E}_G^e - \frac{2\mu_G}{3}(tr\mathbf{E}_G^e)\mathbf{I}\right] - \Pi_{os}(J)\mathbf{I}$$
$$\tilde{\mathbf{D}}_G^f = \mathbf{F}_G^e\dot{\mathbf{F}}_G^f\mathbf{F}_G^{f-1}\mathbf{F}_G^{e-1} = \dot{\gamma}^f\mathbf{N}_G = \frac{\dot{\gamma}_0}{\sqrt{2}}\mathbf{T}_G'$$
$$\frac{1}{\chi_{fluid}}\frac{\partial P_{fluid}}{\partial t} = k_D\nabla^2 P_{fluid} - tr\mathbf{D}$$
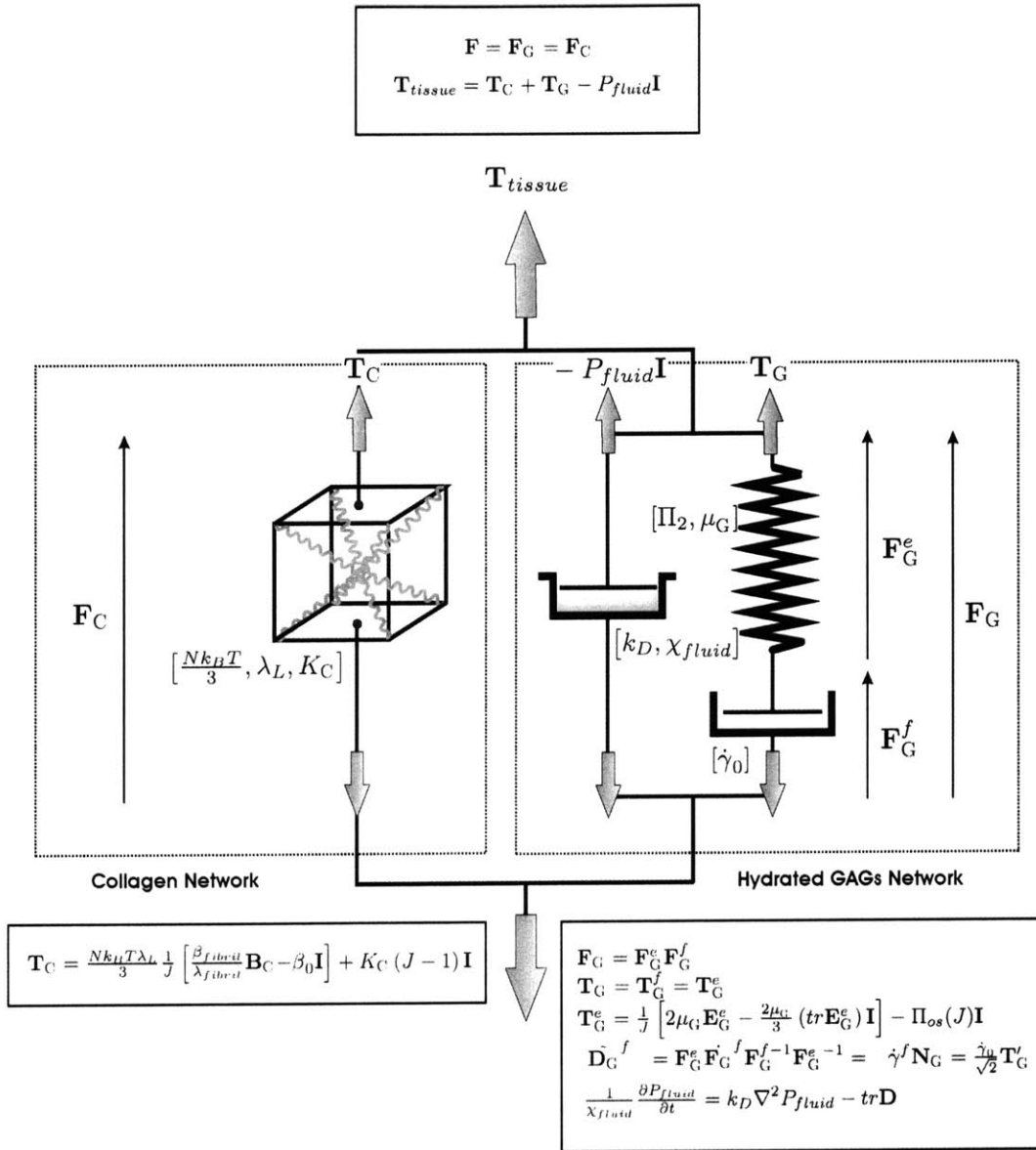
Figure 3-13: Global rheological model proposed for cervical tissue. The main equations are indicated. The square brackets contain the constitutive parameters associated with each part of the model.

Chapter 4

Results from Mechanical Testing and Comparison with the Predictions of the Model

The present chapter will present experimental findings obtained from tests on human cervical samples. Mechanical testing in different configurations was performed on the samples, as well as biochemical tests including collagen and GAGs content assessment. The first section of the chapter will describe the protocol used to prepare and test the samples, and present typical stress-strain curves obtained in confined and unconfined compression tests. The following section will present the results obtained from finite element simulations of these experiments using our constitutive model, and discuss its ability to capture the behavior of the tissue as observed experimentally.

4.1 Experimental Testing of Human Cervical Samples

Human cervical samples were obtained in cooperation with the Tufts-New England Medical Center, from non-pregnant women undergoing hysterectomy. The samples were transported to MIT in saline containers during the 24 hours following surgery. Small cylindrical samples were then prepared, and tested mechanically following the protocol detailed in section 4.1.1. The remaining samples were then frozen, and biochemical tests were carried out over the following days. The protocols used for biochemical measurements are described in appendix B.

4.1.1 Materials and Methods

The hysterectomy specimens were cut into slices of 4 mm of thickness at the hospital, following surgery. These cylindrical slices were not frozen, and transported to the laboratory for mechanical testing in a saline container. The saline used for transport and testing of the samples was 0.9% sodium chloride irrigation (154 mmol/l NaCl, pH 5.5, Baxter, IL).

Preparation of the Samples

For the earliest tests we performed on hysterectomy specimens, the cervices were transported whole to the laboratory where small cylinders were excised using a scalpel blade. However, this technique resulted in low repeatability and accuracy for specimen thickness and shape, due to the compliance and toughness of the tissue, which results in excessive deformation under the required cutting load. A new slicer tool was then designed in order to obtain better results. The slicer is represented in Figure 4-1. It was designed to hold the whole uterus and cervix longitudinally, while bringing down a set of stainless steel blades to cut 4 mm thick transverse slices. The cylindrical slices obtained were then transferred into a saline container prior to mechanical testing.
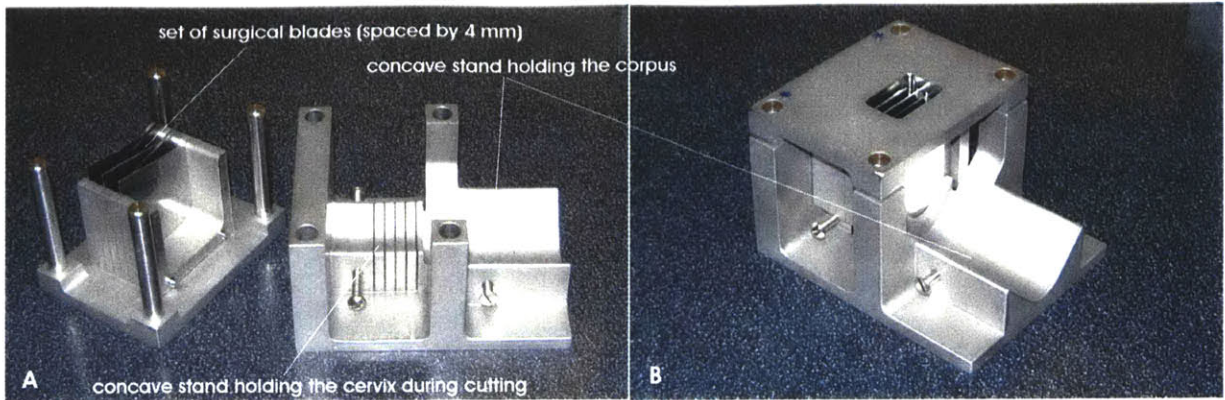
Figure 4-1: Slicing tool designed to cut the cervix samples in 4 mm thick slices. A. Open view. B. Closed view.

The slices obtained using this new cutting tool were flatter, and much more uniform in thickness than the ones previously obtained by hand. An average of four slices were obtained from each cervix. Small cylinders were then cored out of the slices using a standard 8 mm diameter dermal punch. The cylinders were excised in the central region of the cervix, approximately at an equal distance from both the endocervical canal and the outer radius (see Figure 4-2). Coring the specimens with an 8mm punch resulted in an average specimen diameter of 7.6mm. The cylinders were transferred into individual saline containers, and allowed to equilibrate in saline overnight in the refrigerator before testing. This procedure allows us to obtain approximately 4 sets of 3 samples at anatomically equivalent sites for testing.

Part of the samples was used for mechanical testing. For the remaining samples, wet weight was recorded, and they were frozen at -20° C prior to biochemical testing.

Mechanical Testing

Confined Compression The prepared cylinders were tested mechanically in either confined or unconfined compression. Only one single test was carried out on each sample. For the confined compression tests, the samples were loaded into a 7.3 mm diameter
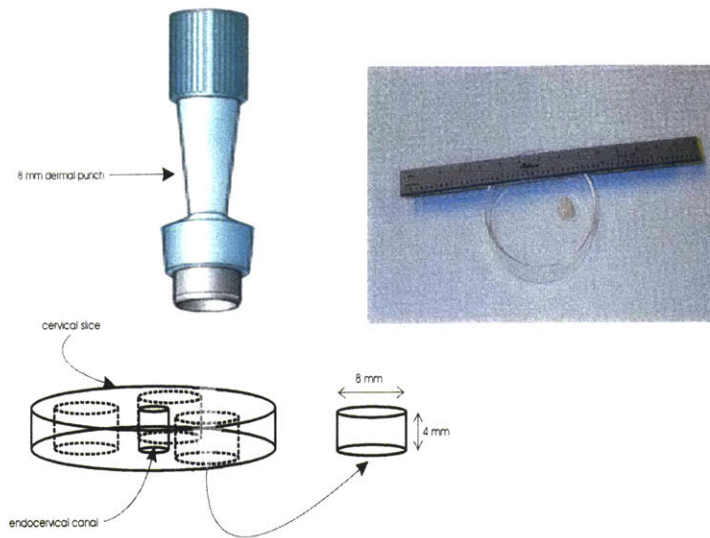
Figure 4-2: Coring of 8mm cylindrical samples from the cervical slices using a standard dermal punch.

acrylic chamber. The diameter was slightly smaller than the actual diameter of the samples to ensure radial confinement from the beginning of the experiment. A rigid porous platen was placed on top of each sample to transmit the compressive load from the plunger to the sample, and allow for interstitial fluid to flow freely from the sample to the surrounding bath. The chamber was mounted on a Dynastat, and 3 to 4 displacement-controlled compression ramps were imposed on the samples, each followed by 10 minutes of stress relaxation at their final strain level. Figure 4-3 illustrates the experimental setup used for the confined compression tests. The tests consisted of three successive ramps of -5% true (logarithmic) strain at a rate of -0.02% per second, each followed by 600 seconds at constant strain to allow for stress relaxation. A preload of 50g (corresponding to a compressive stress of -12 kPa) was imposed on each sample prior to testing in order to accurately determine the sample thickness, and improve confinement as well as flatness of the top surface of the tissue cylinders.
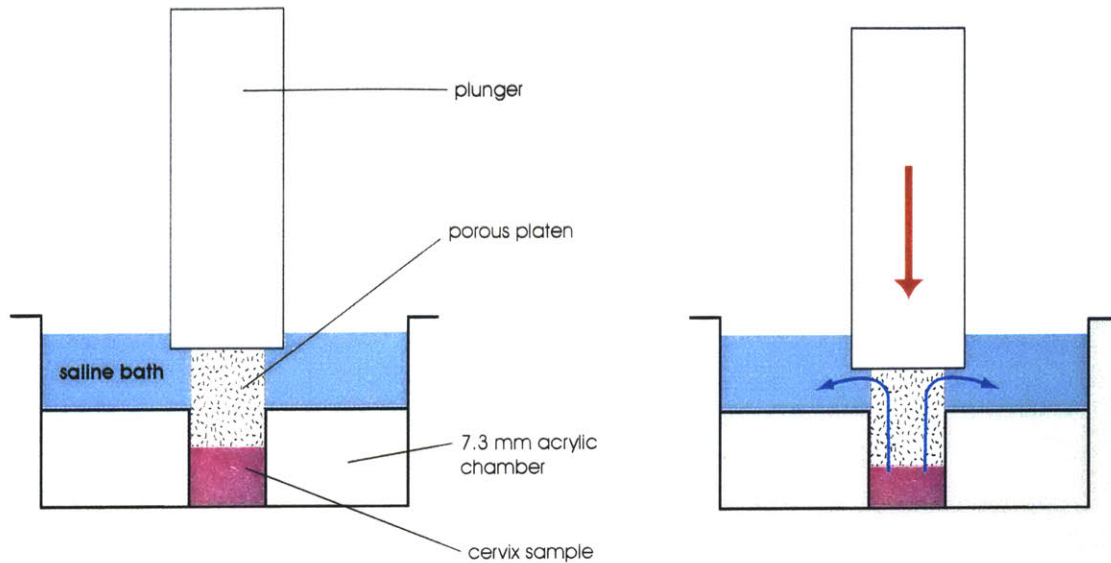
Figure 4-3: Experimental setup for the confined compression tests.

Unconfined Compression   Unconfined compression tests were also performed on some of the samples. For these tests, the samples were in direct contact with a non-porous plunger, immersed in a saline bath. The setup is illustrated in Figure 4-4. The tests consisted of three or four ramps of -10% logarithmic strain each, at a strain rate of -0.1% per second. Again, each ramp was followed by 600 seconds of stress relaxation at constant strain. As for confined compression tests, a preload of 15 grams (corresponding to an initial compressive stress of 3.6 kPa) was imposed on every sample to determine sample thickness and improve flatness of the top surface.

Biochemical Testing

For each hysterectomy specimen, the samples that were not used for mechanical testing were subject to several biochemical assays, including measurement of collagen content after extractability in proteinase K and hydrochloric acid, and total GAGs content. Wet weight was recorded for each sample before freezing. The frozen samples were then freeze-dried. Dry weight was recorded for each sample. The dry samples were dissected
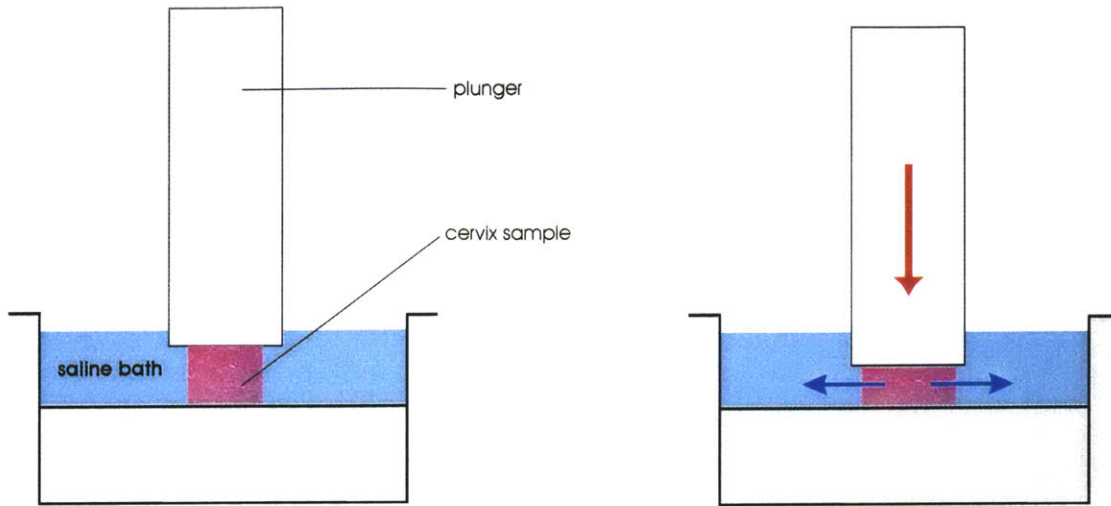
Figure 4-4: Experimental setup for the unconfined compression tests.

into very small pieces, and 1 to 5 mg were used to perform the biochemical assays. The protocols followed to measure collagen and GAGs content are detailed in appendix B.

4.1.2 Results

Mechanical Testing

Confined Compression Typical curves obtained for cervical samples in confined compression are showed in Figure 4-5. The first compression ramp is usually associated to a relatively low peak stress, with a stiffness increasing with strain. The second ramp is associated to a much higher peak stress, still displaying this strain hardening response, but less marked than for the first ramp. The third and final compression ramp is associated with a higher peak stress, but the difference between second and third peaks is usually less marked than between the first and second peaks. Finally, a change in the concavity of the stress curve can be observed in most cases in the course of the third ramp. The curve evolves from a concave-up to a concave-down shape, showing a stiffness decreasing with increasing strain. The relaxation seems to be only partially attained at the end of
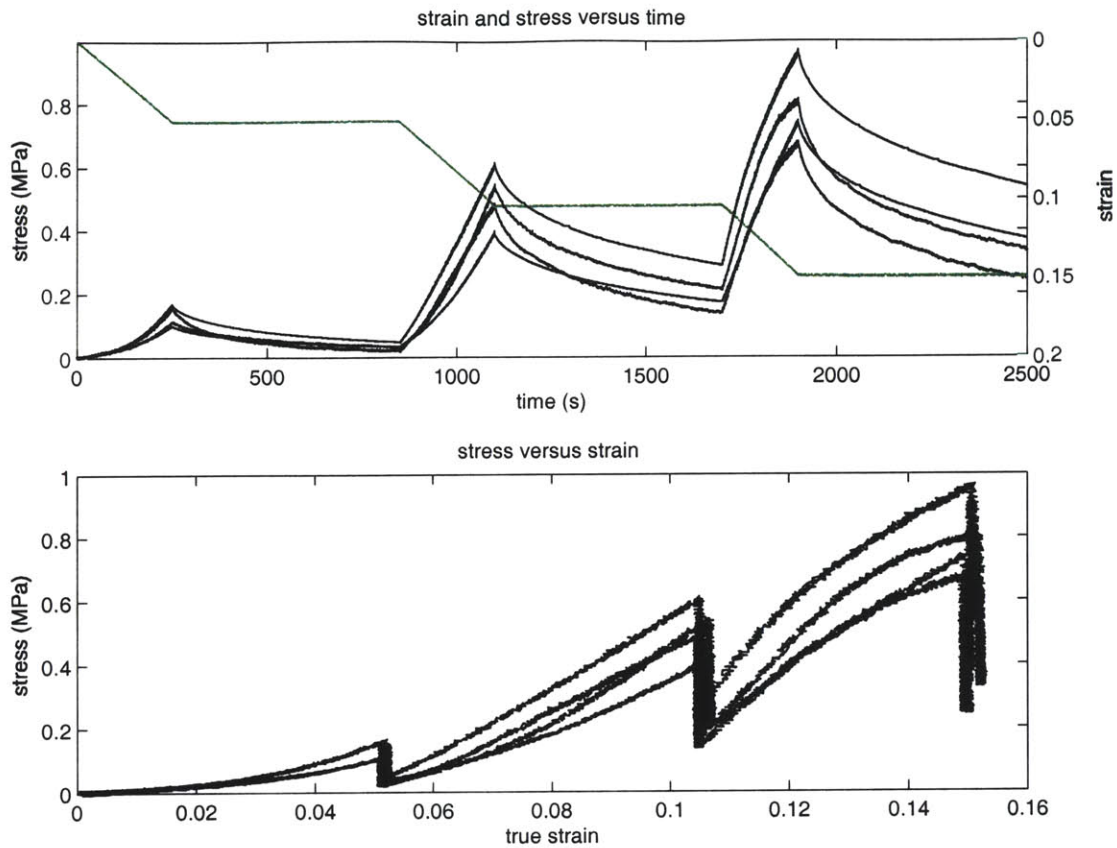
Figure 4-5: Stress versus time and corresponding stress-strain curves obtained in ramp-confined compression tests for representative human cervical samples.

the 600 seconds at constant strain following each ramp. The slope is relatively small, but non-zero. The pseudo-equilibrium stresses reached at the end of the relaxation periods increase non-linearly with strain.

Figure 4-6 represents the stress-strain data obtained by averaging six representative samples tested in the above conditions. This mean behavior in confined compression will be used as the experimental basis to reproduce for the numerical simulations presented in section 4.2.

Unconfined Compression Typical curves obtained for cervical samples in confined compression are showed in Figure 4-7. The response observed in unconfined compression
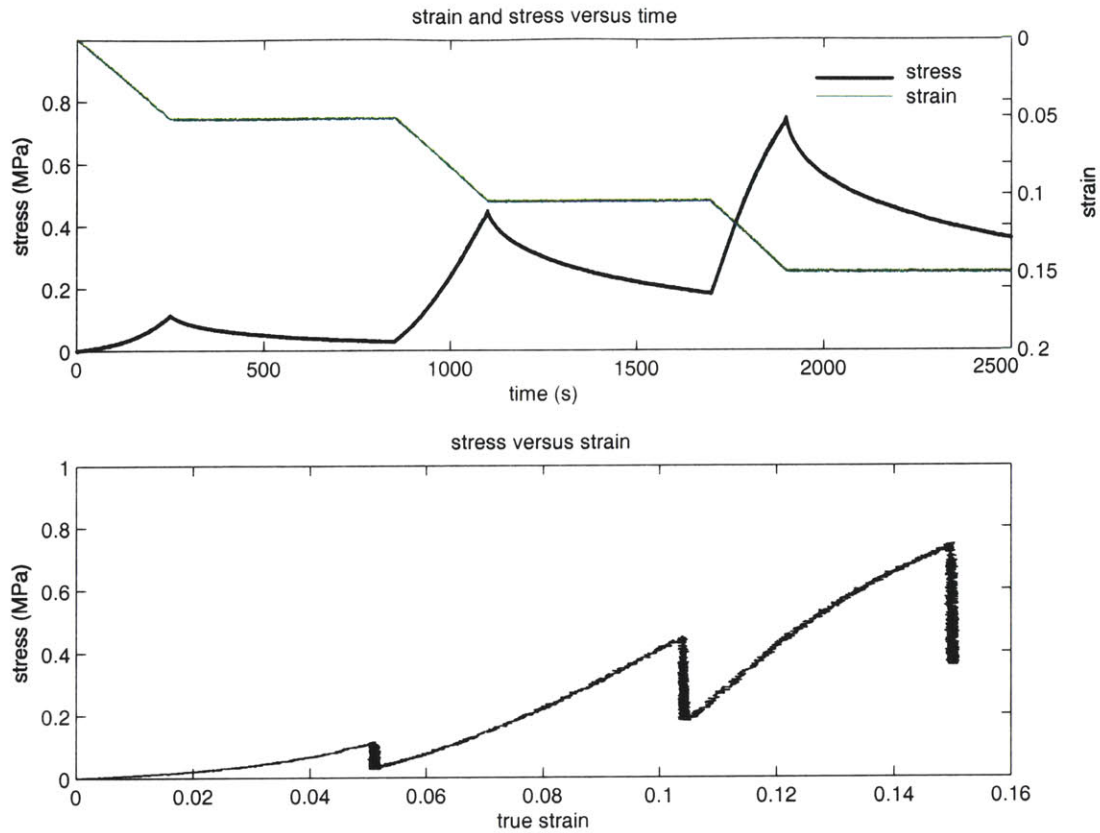
Figure 4-6: Mean stress-time curve and corresponding stress-strain curve for 6 representative human cervical samples in confined compression.

differs significantly from the confined compression behavior. Indeed stress-relaxation still occurs during the periods at constant strain following the compression ramps, but the peak stresses reached at the end of each ramp are over an order of magnitude smaller than those attained in confined compression for the same level of axial strain. This difference may be explained in terms of different deformation mechanisms. In unconfined compression, the volume of the sample is essentially conserved, and minor quantities of interstitial fluid flow out of the sample during relaxation periods. In addition, the sample area in contact with the bathing solution is almost doubled in this setup (sample radius and thickness are approximately equal), which allows for faster outflow. The observed peak-relaxation character of the stress response originates from the shear relaxation com-

100
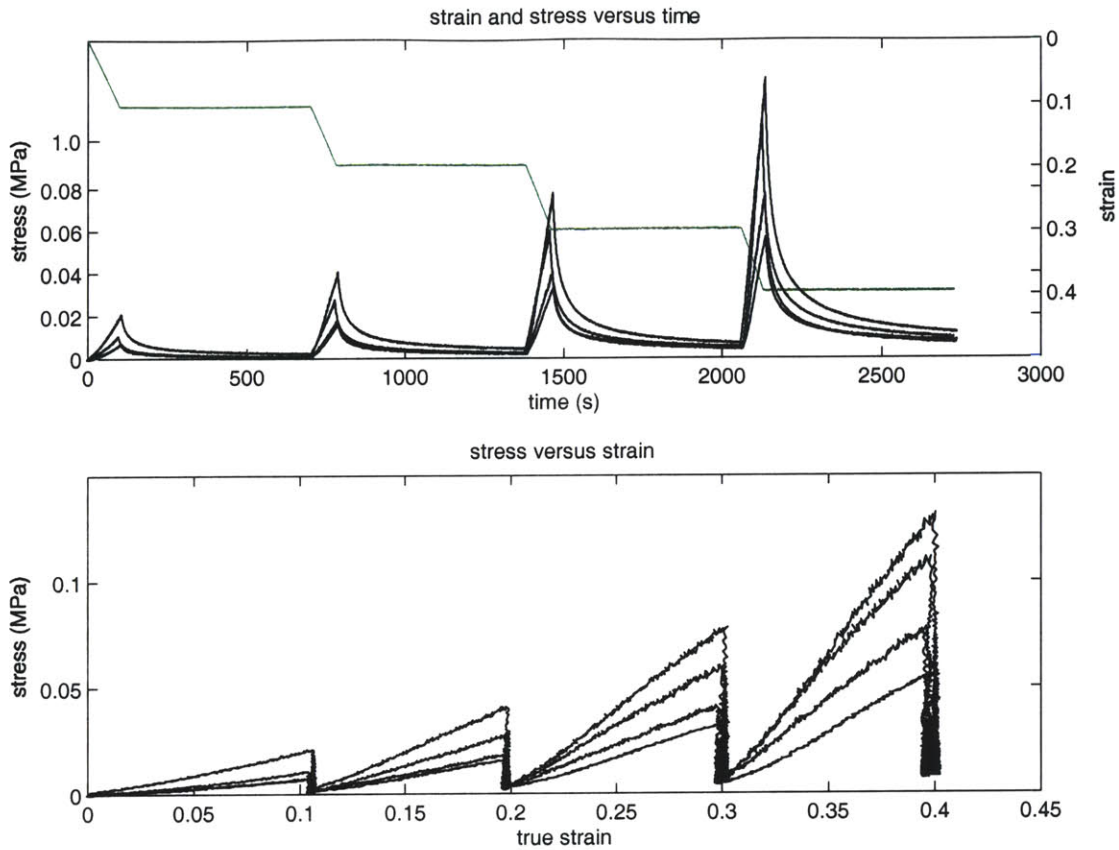
Figure 4-7: Stress versus time and corresponding stress-strain curves obtained in ramp-unconfined compression tests for representative human cervical samples.

ponent of the GAGs network. This quasi-isochoric deformation is indeed equivalent to pure shear in a rotated referential frame. Conversely, in confined compression the volume of the sample is decreased with each ramp and the transient response of the material is controlled by the resulting interstitial fluid flow.

Figure 4-8 represents the stress-strain data obtained by averaging six representative samples tested in the same conditions. This mean behavior in unconfined compression will be used as the experimental basis to reproduce for the numerical simulations presented in section 4.2. It is important to note the large variability in the tissue response as observed on the curves in Figure 4-7. This variability exists between specimens from different patients, as well as between specimens from a single patient, indicating that the

101
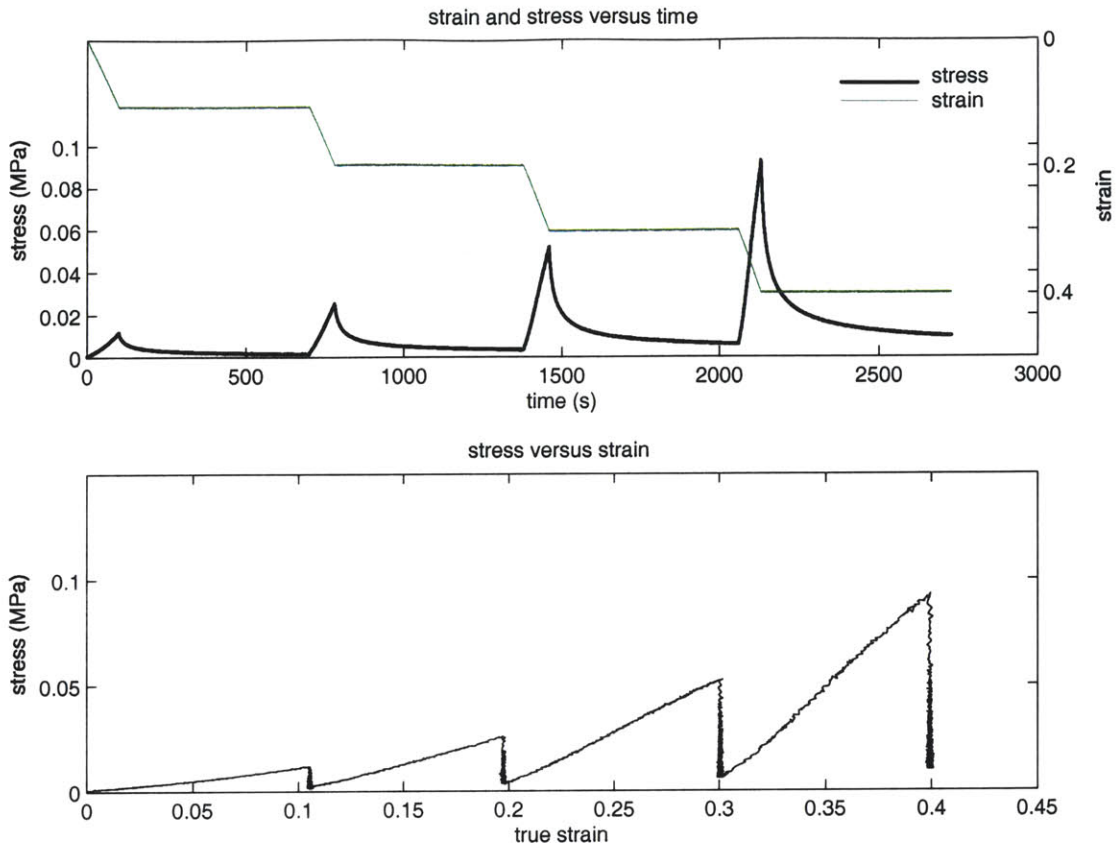
Figure 4-8: Mean stress-time curve and corresponding stress-strain curve for 6 representative human cervical samples in unconfined compression.

protocols used to perform the testing will need to be perfected in the future in order to obtain more repeaTable and reliable results.

Biochemical Testing

The results from the biochemical tests carried out on the tissue samples are reported in Table 4.1. The only variables analyzed were water content, collagen content after extraction in proteinase kinase and hydrochloric acid, and total glycosaminoglycans content. Due to the restricted amount of data available at this stage of the project, no statistical correlation has been investigated yet between the biochemical characteristics of a particular sample and the mechanical constitutive parameters used in the simulation to

fit its experimental mechanical behavior. These first results from the biochemical tests are presented for comparison with the data available in the literature and summarized in chapter 2.

Water	85.2 ± 1.7 % of total mass	
Dry tissue	14.8 ± 2.0 % of total mass	
	ExtracTable collagen content (proteinase K + hydrochloric acid)	Total GAGs
	31.41 ± 6.52 % of dry mass	1.08 ± 0.24 % of dry mass

Table 4.1: Water content, extractable collagen (proteinase K and chlorhydric acid) and total glycosaminoglycans content measured on 15 cervical specimens from non-pregnant women.

The samples tested were obtained from 5 different patients, and span the whole range of anatomical locations within the cervix from where samples have been tested mechanically. These samples were obtained from the same specimens for which the mechanical data was presented above. These results are in agreement with the values found in the literature and summarized in Table 2.2 of chapter 2. Using an approximate value of 50% for extractability of collagen in hydrochloric acid and proteinase K (a similar value is reported in the literature for acetic acid and pepsin [13]) would give an estimate total collagen content of about 63%, also in the range of values found in the literature.

4.2 Finite Element Simulations of the Compression Tests

Finite element simulations were carried out attempting to reproduce the qualitative behavior observed experimentally in confined and unconfined compression tests, presented in section 4.1. As previously outlined, we do not have yet sufficient data available to establish correlations between experimental and simulation parameters for individual samples. Therefore, in this first evaluation of the model, only its ability to capture the mean behavior observed experimentally for the tissue in the two modes of deformation tested was assessed. The results of these simulations are presented in this section.

4.2.1   Finite Element Discretization

The simulations were realized using the commercially available finite element code ABAQUS 6.3. The material constitutive behavior detailed in chapter 3 was coded as a fully three-dimensional user material subroutine UMAT. The implementation also enables two-dimensional simulations in plane strain and axisymmetric modes. The reader is referred to appendix A for the details of the numerical implementation of the model. As detailed in section 3.5 and appendix A, the coupled matrix-fluid flow problem was treated as a coupled thermal-mechanical analysis. The simulations presented in this section were realized using axisymmetric elements, taking advantage of the problem symmetry, to improve computational efficiency. Thus, continuum 4-node linear axisymmetric elements for coupled thermo-mechanical analysis CAX4T were used.

Confined Compression Simulations

The boundary conditions for the confined compression simulations are illustrated in Figure 4-9, and reflect the experimental setup illustrated in Figure 4-3. The sample is confined in the well and displacement is allowed in the axial direction along the outer circumference, while the bottom is constrained along the radial (1) and axial (2) directions. The displacement ramps are imposed on the top surface, along the 2-direction. No heat flux (fluid flow) is allowed on the sides and at the bottom, and free heat flux is allowed on the top surface (porous platen), where the temperature is maintained constant at 0 (corresponding to the reference bath pressure). Also, it is important to note that friction between the sample and the surface of the confinement well was neglected and not modeled in the simulations.

Unconfined Compression Simulations

The boundary conditions for the unconfined compression simulations are illustrated in Figure 4-10, and reflect the experimental setup illustrated in Figure 4-4. In this configuration, the displacement ramps are imposed on the top surface, and axial displacement is
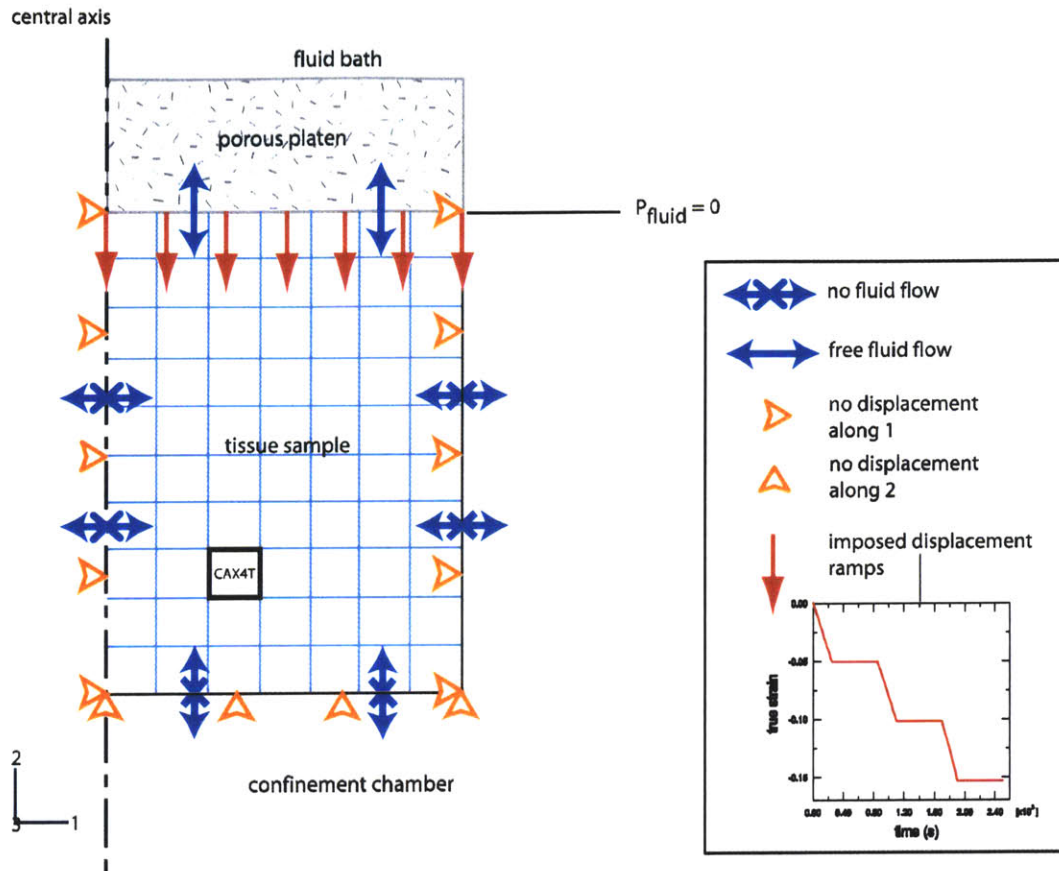
Figure 4-9: Boundary conditions used for the confined compression FE simulations.

constrained on the bottom surface. Free heat flux is allowed on the sides of the sample, where the temperature is maintained constant at 0 (reference bath pressure). No heat flux is allowed through the top and bottom surfaces (the plunger in contact with the top surface is not permeable, as is the case for the bottom of the compression chamber) . Friction between the chamber bottom surface and the expanding sample was neglected in the simulations.

4.2.2 Mesh Size and Convergence

The influence of the mesh resolution on the results was studied, and the conclusions are illustrated in Figure 4-11 in the case of the confined compression simulation. The graph
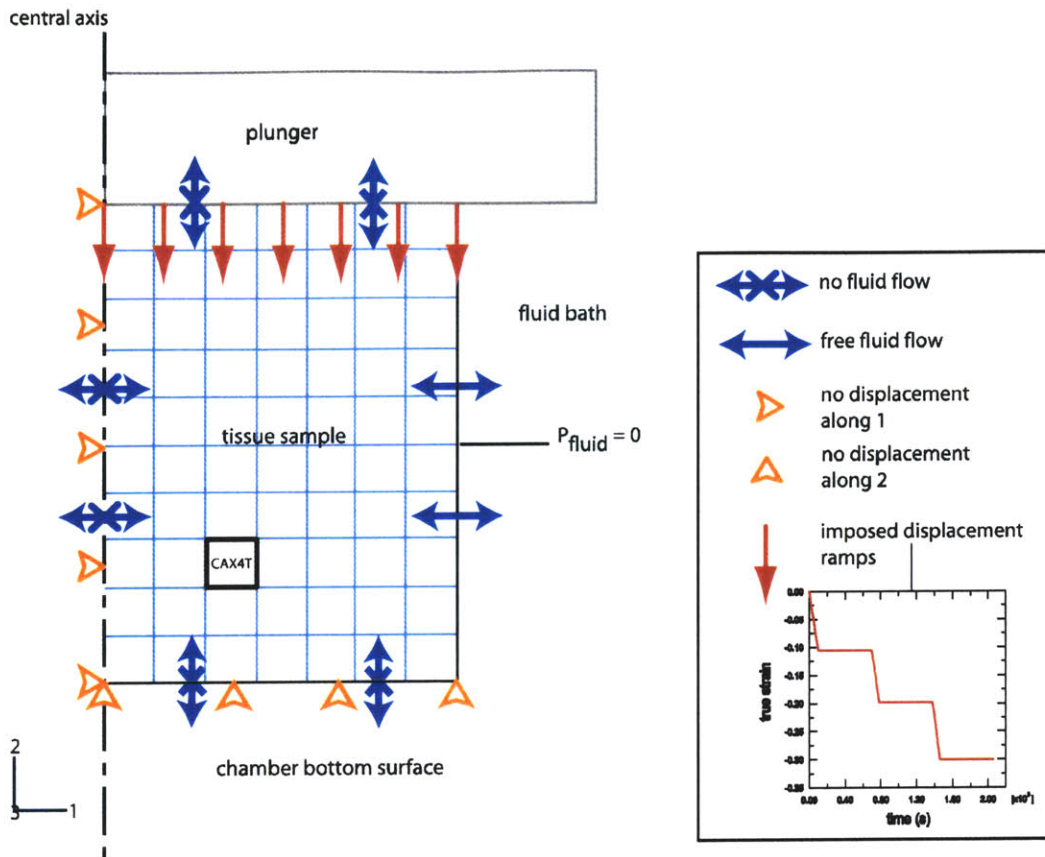
Figure 4-10: Boundary conditions used for the unconfined compression FE simulations.

plots the computed axial stress on the top surface of the sample as a function of time for the different mesh resolutions. Convergence is reached for a mesh of 432 (18x24) elements. In order to ensure accurate results and computational efficiency, this mesh size was used for all the simulations presented in the following, including both confined and unconfined compression setups.

4.2.3 Results

The constitutive parameters of the model described in chapter 3 were fit to the data presented in Figs. 4-6 and 4-8 according to the following procedure. The relaxation ramps of both curves were extrapolated to obtain an estimate of the corresponding equilibrium
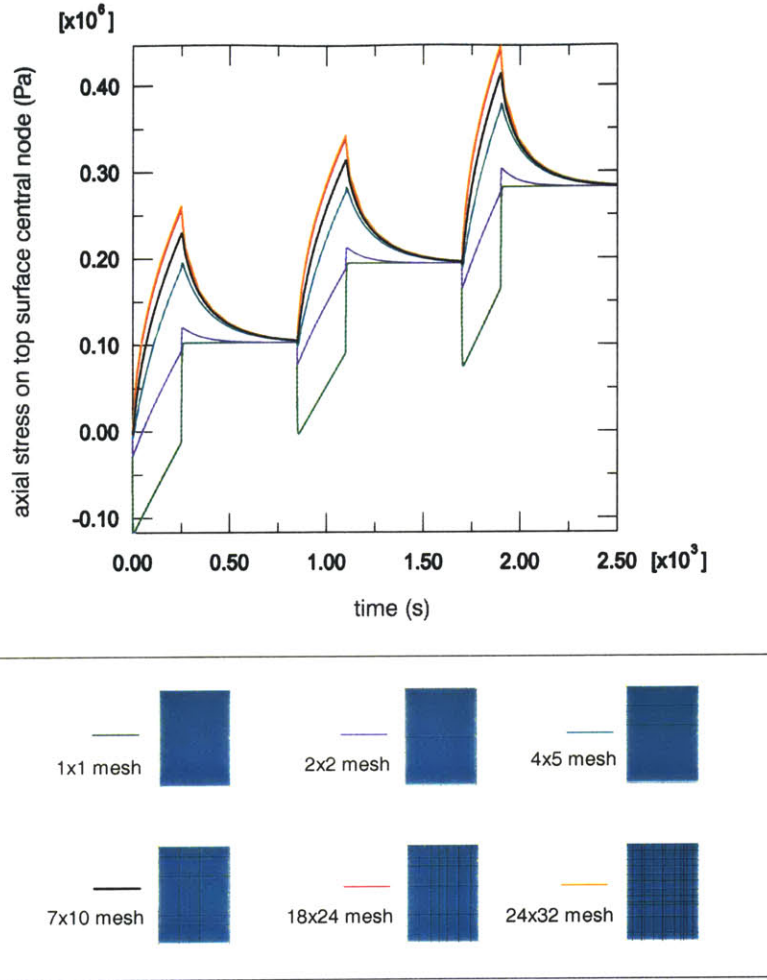
Figure 4-11: Influence of the size of the mesh on the computed axial stress.

stresses (see Table 4.2).

These equilibrium stresses only depend on the parameters $\frac{Nk_BT\lambda_L}{3}$ (initial shear modulus) and $\lambda_L = \sqrt{n}$ (locking stretch) for the collagen network, and the parameter $\Pi_2 = \kappa R^0$ for the GAGs network. Indeed, as stated in chapter 3, the second quantity $\Pi_1 = 2\mathcal{R}TC_0$ determining the osmotic pressure function was not considered as an adjusTable parameter. The collagen bulk modulus K_C introduced in chapter 3 to account for additional effects of compressibility was not used, and was set to zero in the simulations presented here. The shear modulus and shear relaxation coefficient of the GAGs network, as well

	1st equilibrium stress (kPa)	2nd equilibrium stress (kPa)	3rd equilibrium stress (kPa)
confined compression	27	152	240
unconfined compression	3	6	10

Table 4.2: Extrapolated equilibrium stresses for the averaged confined and unconfined compression curves.

as Darcy's permeability k_D, only influence the transient stress variations, and do not affect the equilibrium properties. As the state of deformation at the end of each ramp is completely determined in the case of confined compression, the equilibrium stresses can be obtained as the sum of the equilibrium collagen stress and the equilibrium osmotic pressure, completely determined by the three constants $\frac{Nk_BT\lambda_L}{3}$, λ_L, and Π_2. We note that Π_2 also determines the initial osmotic pressure, so that the collagen prestretch necessary to balance the initial osmotic pressure can be computed from the two constants ($\frac{Nk_BT\lambda_L}{3}$, λ_L) for the collagen network. The initial collagen stretch together with the known stretches at the end of each ramp determine the collagen equilibrium stresses. Variation of these three parameters was performed in order to obtain the best fit between the predicted and experimental equilibrium stresses following a least square differences criterion. These values were then used to perform an unconfined compression simulation, and obtain the corresponding radial stretches at the end of each relaxation period. These values along with the known axial stretches at the end of the relaxation periods give a good estimate of the end of relaxation state of deformation in the sample, and were used to calculate predicted equilibrium stresses given a triplet ($\frac{Nk_BT\lambda_L}{3}$, λ_L, Π_2). Another fit was performed using this method based on the three estimated equilibrium stresses for the unconfined compression experiment, once again following a least square differences criterion. Two different triplets ($\frac{Nk_BT\lambda_L}{3}$, λ_L, Π_2) were thus obtained that best adjusted respectively to the equilibrium stresses of the two experiments. These parameters were used in the simulations of the two modes of deformation, and the other parameters were adjusted to best fit the transient stress variations. The Darcy's hydraulic permeability k_D was adjusted to best match the stress peaks and relaxation patterns in the confined com-

pression tests, as interstitial fluid flow constitutes the predominant mechanism generating the observed transient behavior, while the GAGs shear modulus and shear relaxation coefficient were subsequently adjusted to improve the fitting. However, the impact of these parameters is only significant in the unconfined compression case, for which a significant amount of shear deformation is present. The interstitial fluid compressibility coefficient χ_{fluid} was not adjusted and kept constant at 0.5×10^{-9} Pa^{-1}, which corresponds to the bulk modulus of pure water. The stress output in the case of unconfined compression was nominal axial stress, as defined by the load divided by the initial area of the sample, in accordance with the data obtained experimentally. For confined compression, nominal axial stress and true (Cauchy) axial stress are identical. The sample dimensions used in the simulations were taken equal to the averaged experimental dimensions. Sample thickness plays an important role due to the specific length scales associated with diffusion processes.

The resulting stress/time curves along with the parameters used are presented in Figure 4-12. For the confined compression simulations, the value used for Darcy's permeability was adjusted to account for the effect of increasing levels of compressive strain. The value was decreased linearly in the course of each compression ramp. The four values indicated in the Table enclosed with the graph correspond to the initial value (zero strain), and the values reached at the end of each of the three subsequent compression ramps following a linear decrease. k_D was kept constant during the relaxation periods. Although the maximum strain reached is -15%, a significant decrease in the hydraulic conductivity can be expected. The deformation experienced by the tissue sample is highly non-homogeneous across the thickness, and a strain wave propagates from the top to the bottom of the sample during compression. This propagation is only very limited during the compressive ramps, and strain homogenization mainly occurs during relaxation, along with fluid flow from bottom to top. This phenomenon is illustrated on the contour plots presented in Figure 4-13.A. These plots show the distribution of axial true strain within the sample at the different stages of the simulation. One can easily note the high strain

Figure 4-12: Simulation results for confined compression (top frame), and unconfined compression (bottom frame) using a distinct sets of constitutive parameters. The parameters are indicated in the enclosed tables.

concentration in the very top layer of the sample, through which all fluid flow leading to stress relaxation must occur. Despite an average strain of -15% over the thickness, the axial strain on the top surface reaches a level of approximately -40% at the end of the third compression ramp, as illustrated in Figure4-13.B, while the bottom zone of the sample is subjected to much lower and progressive strain variations. Fluid flow is thus impeded by these locally high levels of deformation, significantly affecting the hydraulic conductivity. The conductivity decrease imposed during the simulations was homogeneous over the sample thickness, although a future implementation of the model should adapt k_D to the local level of deformation, as a function of the volumetric Jacobian. As
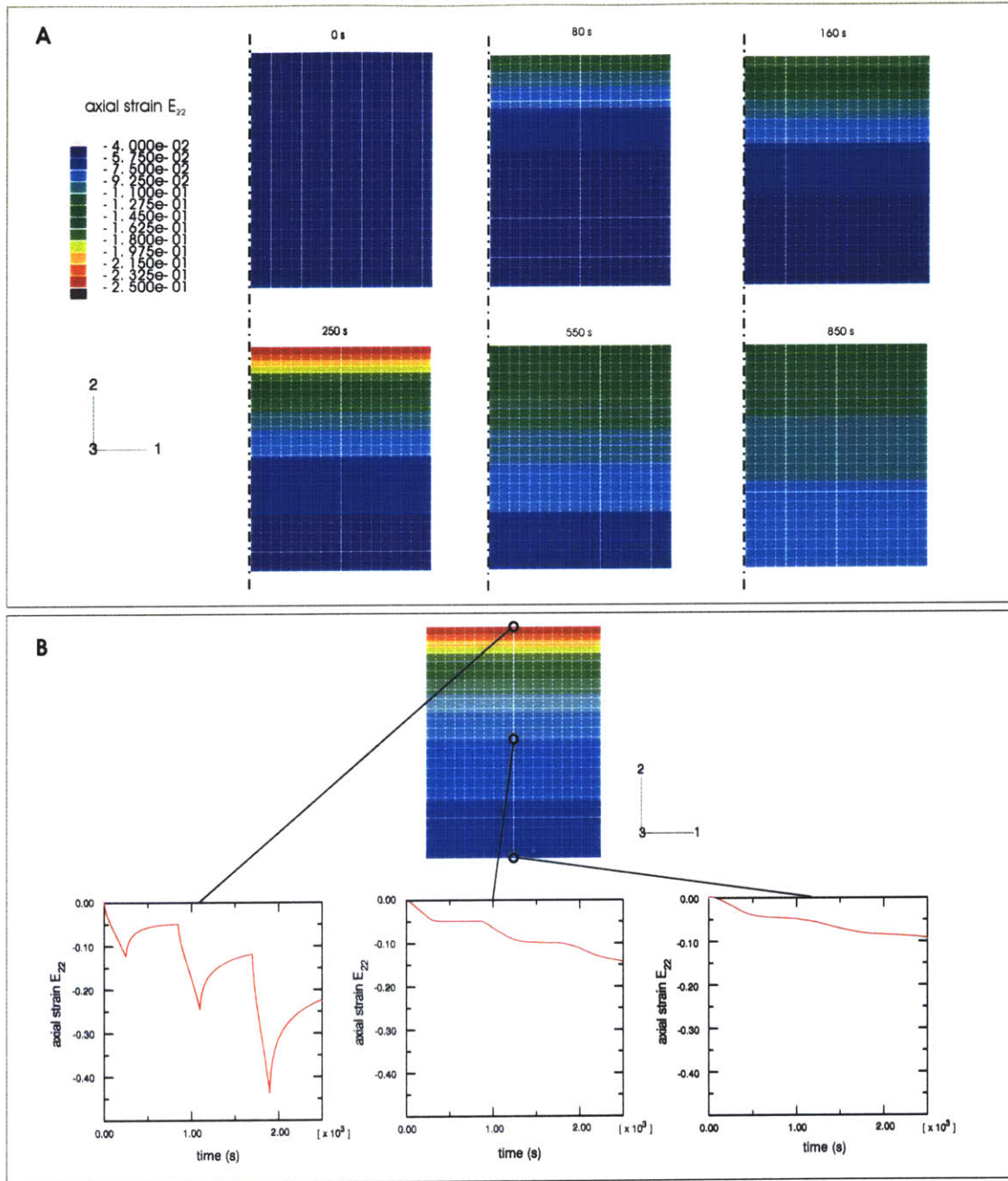
Figure 4-13: A. Contour plots of axial logarithmic strain for the confined compression simulation from Fig. 4-12, over the first compression ramp and relaxation period. B. Corresponding axial strain history at different locations within the thickness.

opposed to the confined compression simulations, the value used for k_D in the unconfined case was kept constant at its initial value over the whole deformation. Indeed, axial strain is homogeneous over the thickness of the sample due to the different geometry of the simulation, flow occurring only at the external circumference of the sample. Also as the sample is left free to expand laterally, volume reduction is very limited, and the final volumetric Jacobian at -30% compressive strain is approximately 95%. Figure 4-14 shows the interstitial fluid flow distributions for the confined and unconfined simulations, over the course of the second compression ramp and subsequent relaxation period. One can note the restriction of flow to the very top surface of the sample in the confined setup during compression, and its progressive extension to the deeper tissue layers as compression is stopped and relaxation takes place. For the unconfined simulation, flow occurs predominantly at the outer edge during compression, the pore pressure rising progressively at the center of the cylindrical sample, while during relaxation the flow extends radially towards the central axis. The corresponding contour plots for interstitial fluid pressure are given in Figure 4-15.

As mentioned above, the parameters used to fit the experimental data for the two modes of deformation are different. If the experimental data had been obtained on specimens from a single patient, the constants used to fit the two behaviors should have been the same. However, this is not the case for these curves, and even if they represent an averaged behavior, the number of samples included to obtain these averages is not high enough at this point to expect a single set of parameters to accurately model both sets of data. Indeed, the equilibrium stresses observed and reported in Table 4.2 are separated by approximately one order of magnitude, while the strain levels in the confined experiments are half of those in the unconfined ones. This mismatch between the two sets of data cannot be well captured by a single set of constants. These differences may arise from the huge variability observed in the mechanical properties of samples corresponding to different patients. This variability can be observed on Figs. 4-5 and 4-7, which demonstrate important variations from sample to sample, both for the peak
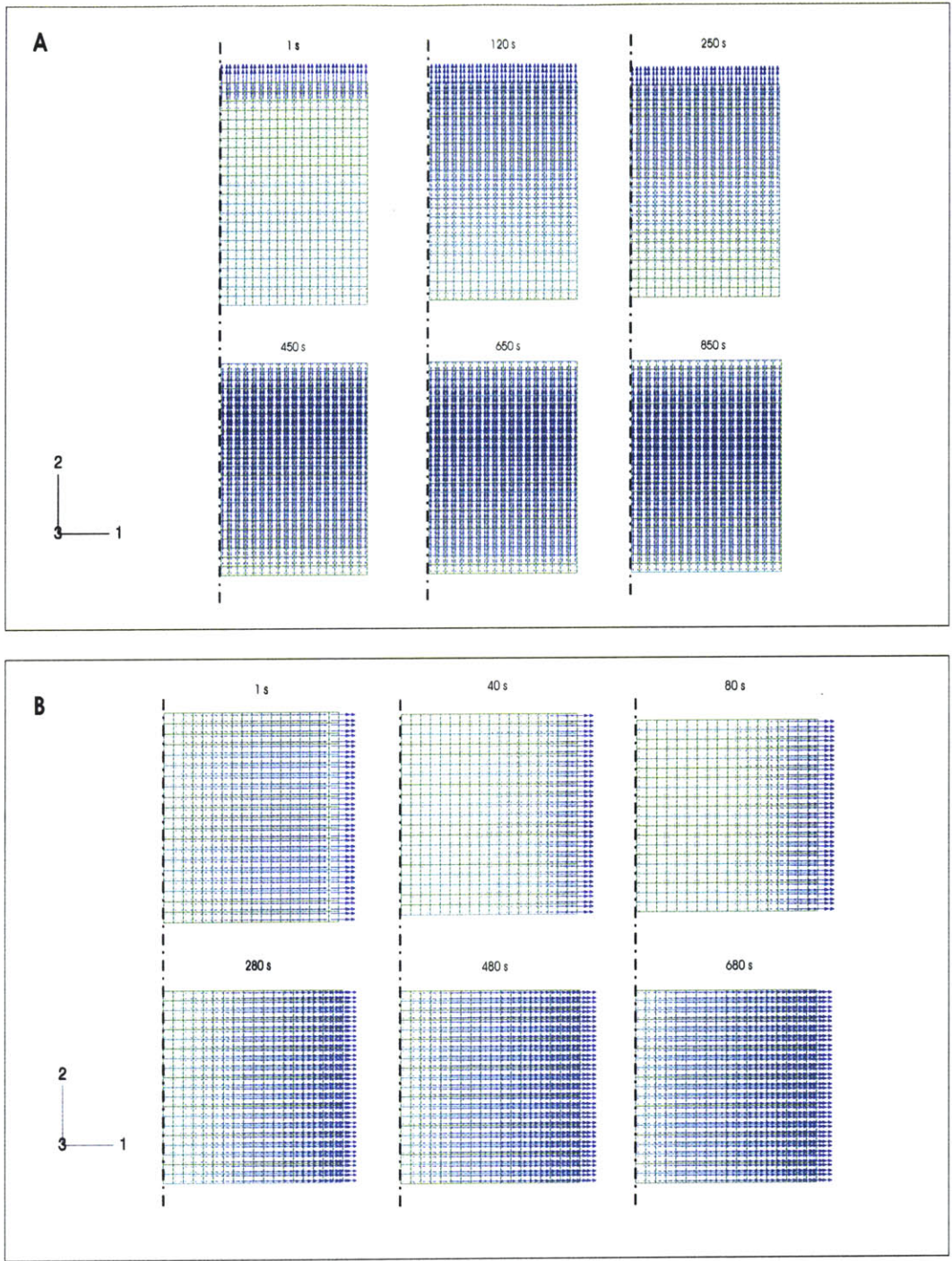
Figure 4-14: Interstitial fluid flux distribution for the confined simulation (A), and the unconfined simulation (B), over the middle compression ramp, and subsequent relaxation. Time 0 corresponds to the beginning of the second ramp.

113
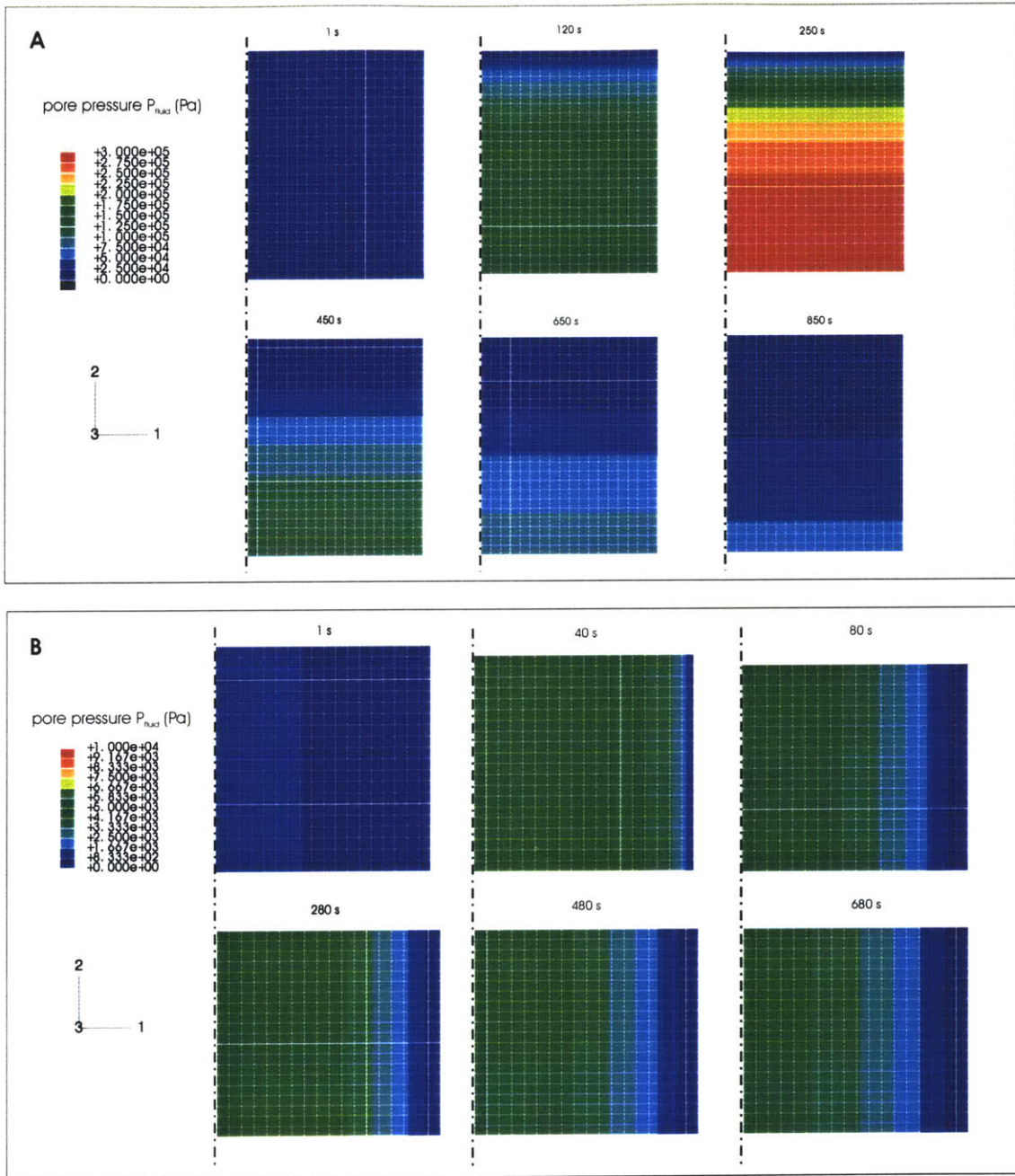
Figure 4-15: Pore pressure contour plots for the confined simulation (A), and the unconfined simulation (B), over the middle compression ramp, and subsequent relaxation. Time 0 corresponds to the beginning of the second ramp.

and equilibrium stresses. The data used in the average behaviors from Figs. 4-6 and 4-8 each included samples from two different patients, while the mechanical moduli presented in the literature for cervical tissue can vary by as much as an order of magnitude from one patient to the other. Other factors contributing to the observed differences between the two behaviors may be the difference in the levels of imposed preload (12 kPa for confined compression tests compared to 3.6 kPa for unconfined compression), and the transverse and axial prestrains imposed on the samples in confined compression when deformed to fit inside the well and ensure confinement, which may contribute to stiffen the response observed for this mode of deformation.

To provide an order of comparison with the previous simulations, the best fit obtained by adapting a single set of constants simultaneously to the six equilibrium stresses of Table 4.2 is presented in Figure 4-16. One can note that the fit is far from perfect, especially for the confined case. However, the trends observed experimentally for each mode of deformation are reproduced by the simulations. The relative heights of the different stress peaks are well captured by the model, and the large difference between the levels of stress experienced in the two modes of deformation is reflected in the simulations. This first attempt emphasizes the necessity of performing the different tests to be fitted on samples from a single patient. The average curves are only able to represent qualitative trends of the stress history, rather than actual values of peak and equilibrium stresses.

The simulations from Figure 4-12 provide a good approximation of the average experimental behavior for both settings, satisfactorily capturing the respective peak and equilibrium stresses. The relative proportions of the peaks are well captured by the model in the two cases. Figs. 4-17.A and 4-17.B detail the individual contributions of the model components (collagen network, GAGs network, interstitial fluid) to the total axial stress, in the confined and unconfined simulations respectively. These contributions are plotted for several locations within the sample for each mode of deformation. In confined compression, the contribution of interstitial fluid pressure to the total stress naturally increases with increasing distance from the top surface (porous platen), while similar ef-
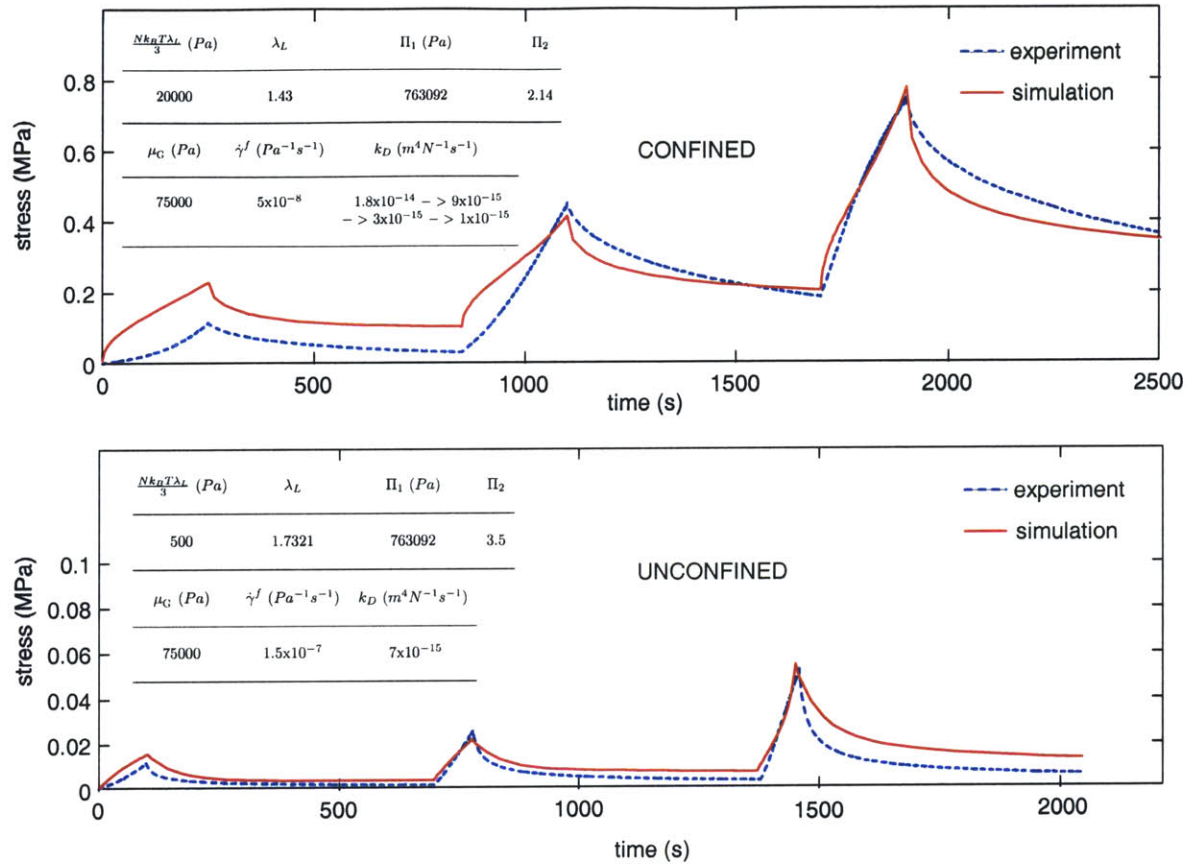
115
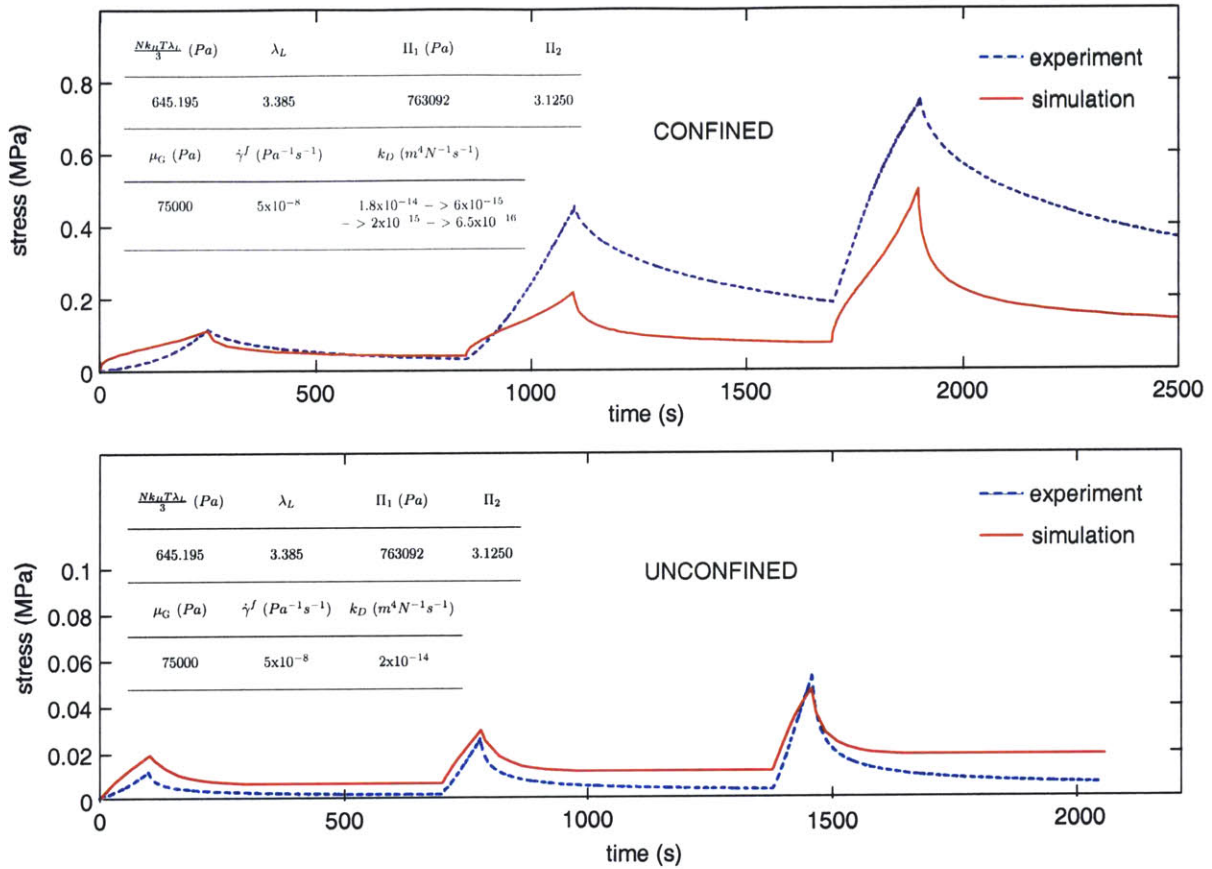
Figure 4-16: Simulation results for confined compression (top frame), and unconfined compression (bottom frame) using a common set of parameters.

fects (although much lower in magnitude) can be noted in unconfined compression with increasing distance from the outer edge (where outflow occurs freely). Another point of interest is the different behavior found for the collagen network in the two modes of deformation. Although significantly prestretched in both cases, the collagen progressively unstretches with compression in the confined case, increasing the total compressive stress within the tissue. Interestingly, the collagen response significantly differs from that in unconfined compression, where the tensile stress initially present in the collagen to balance the osmotic pressure increases with the level of compression, and is partially responsible for the low levels of equilibrium stress observed experimentally. This phenomenon is due

116

to the lateral expansion associated with the incompressible response of the interstitial fluid.

Although the fit is satisfactory for both modes of deformation, one can note the higher equilibrium stress after the last relaxation period in the unconfined setting compared to the measured value, which points again to the very low equilibrium stresses associated to unconfined compression when compared to confined compression (see Table 4.2), differing by approximately one order of magnitude. A second point of concern may be the difficulty of the simulations to capture the low value of the first peak stress relatively to the others in the confined configuration. Fitting the first peak gives too low stresses for the two subsequent ones, while fitting the latter closely would be associated with a higher first peak. This may be due to a non-perfectly flat top surface for the sample. Indeed, when deformed to fit into the confinement chamber (see Figure 4-3), the sample develops transverse stresses and stretches axially to adapt to this smaller diameter, which might result in a slightly concave top surface, lifted on the outer edge. The preload imposed on the tissue sample might not be sufficient to suppress this artefact, due to the very stiff tissue response in this setting. The prestress of 12 kPa imposed on the sample is almost an order of magnitude smaller than the first peak stress of about 100 kPa noted on the average curve.

To investigate this hypothesis, a confined compression simulation on a tissue cylinder with a non-flat top surface, corresponding to a maximum central deflection of 8% of the total thickness, was carried out (the considered geometry is represented in Figure 4-18). The parameters used for this simulation were based on the fit presented in Figure 4-12. The resulting stress/time history is presented in Figure 4-19, along with contour plots of the axial stress. These contour plots show the axial stress distribution and progressive flattening of the sample up to the second compression ramp. The agreement between experimental and predicted stress is very good for this simulation. The relative heights of the three peaks and all the equilibrium stresses are well captured. Also, the concave-up shape of the first peak and progressive change to a concave-down shape for
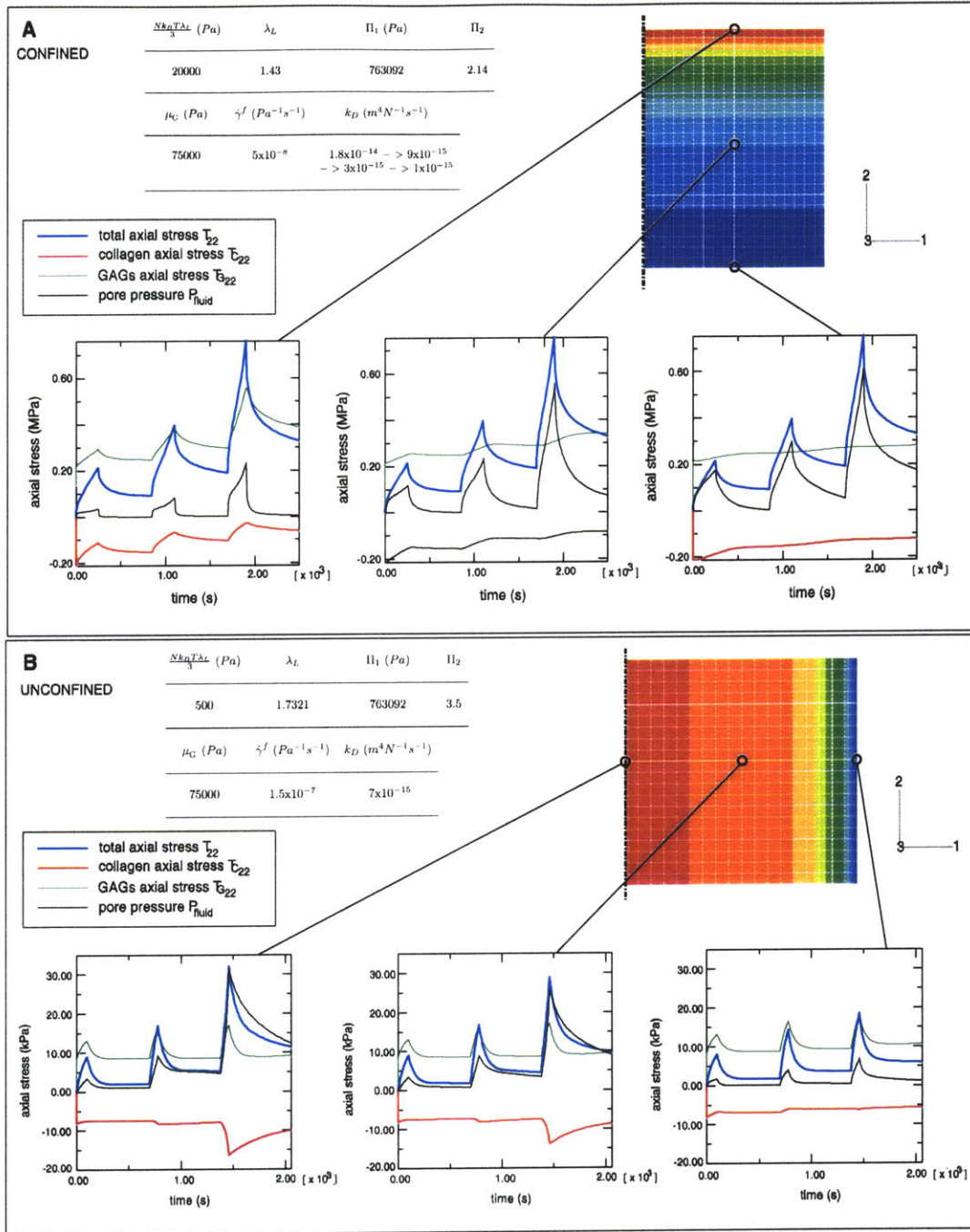
Figure 4-17: Individual contributions of the different parts of the model to the computed axial stress in confined compression (A), and unconfined compression (B).
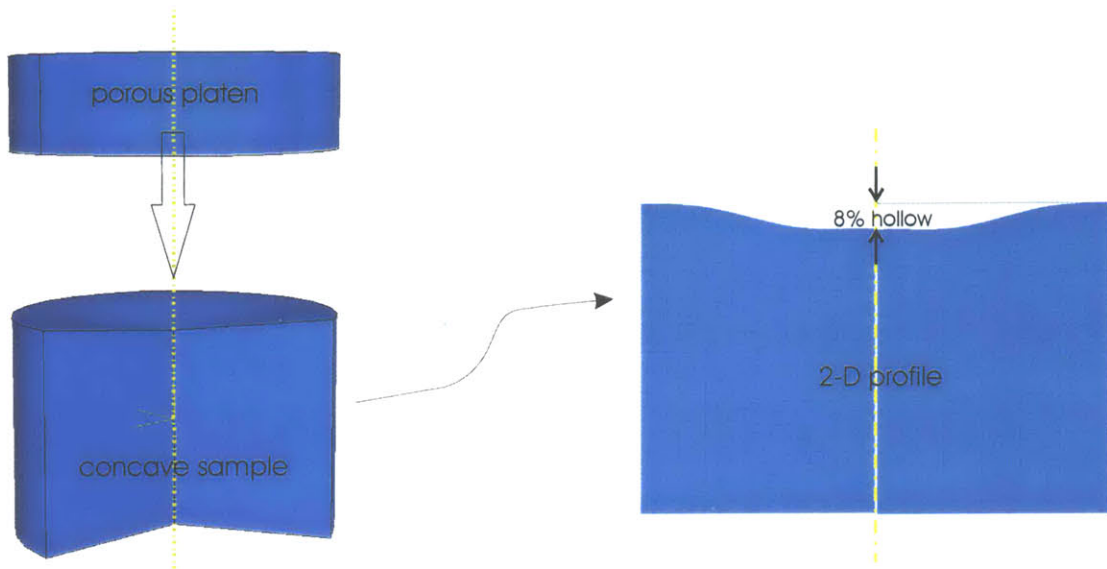
Figure 4-18: Confined sample geometry, with 8% initial central hollow.

the two subsequent peaks are successfully predicted by the model in this configuration. These results outline the importance of a carefully chosen level of preload, and well diameter. This emphasizes the need of very precise experimental settings for this mode of deformation in order to obtain relevant and repeaTable data.

4.2.4 Physical Relevance of the Constitutive Parameters

As mentioned previously, a larger amount of experimental data will be necessary to identify correlations between the biochemical characteristics of a given sample and the constitutive parameters used to fit the data obtained from its mechanical testing. Nevertheless, first conclusions can be drawn from the values used for these parameters in the simulations presented above so as their physical relevance.

- Collagen initial modulus $\frac{N k_B T \lambda_L}{3}$: the values obtained for the individual fits presented in Figure 4-12 differ quite significantly from each other, and it is difficult at this stage to draw conclusions concerning the relevance of this parameter and its re-

119
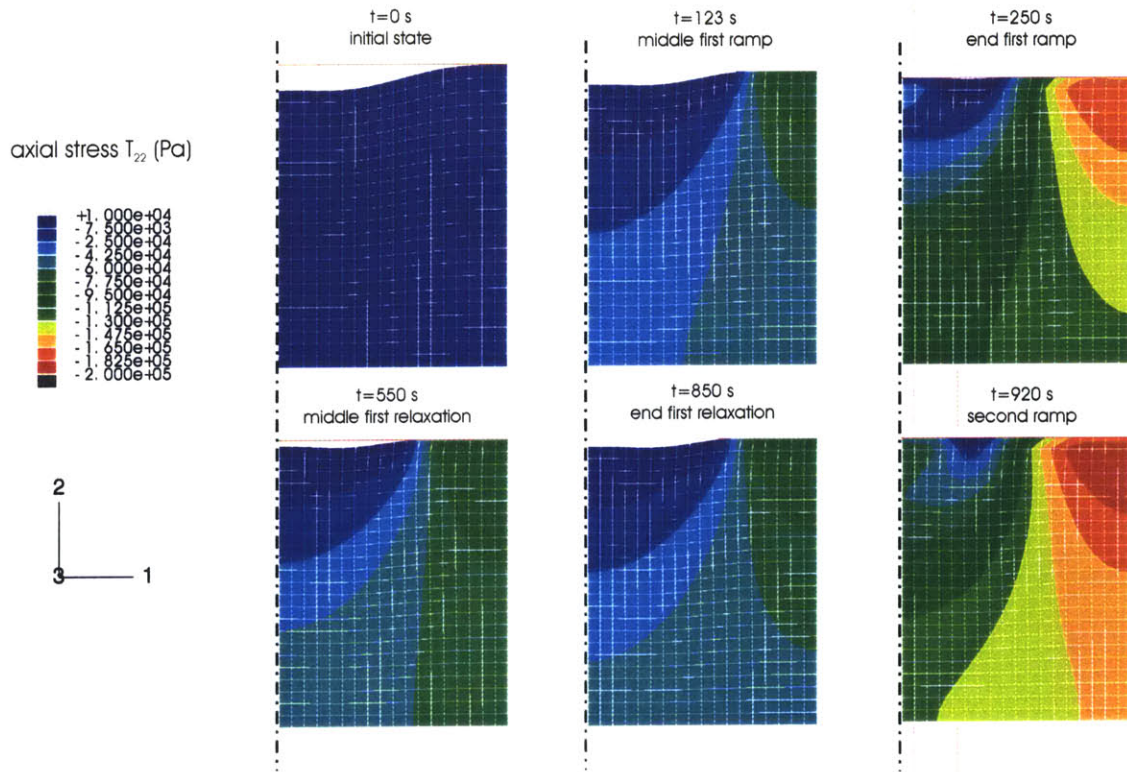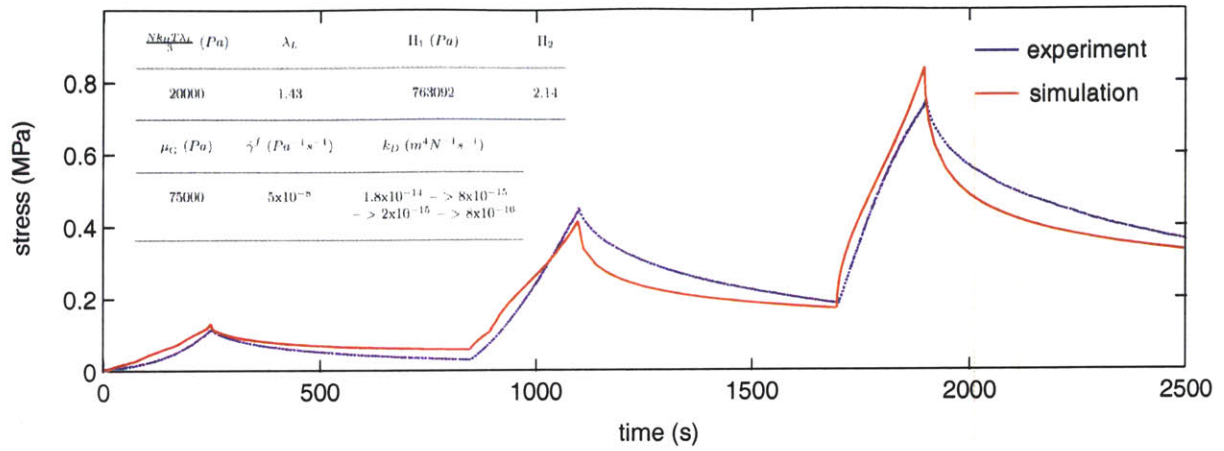
Figure 4-19: Simulation results for a non-flat sample top surface (8% maximum inflection), in confined compression. Stress-time plot and axial stress contours for the first two ramps of confined compression.

lation to the actual properties of the collagen network. This difference in the values found only reflects the large difference between the equilibrium stresses observed for the samples tested in confined and unconfined compression. Further testing of single specimens in different modes of deformation will determine whether a single value can successfully model the collagen behavior under these different testing conditions.

- Collagen locking stretch λ_L: the values found for the locking stretch in both simulations are relatively close (1.43 for the confined case versus 1.73 for the unconfined case). Furthermore, they are in the range of expected values for the maximum extensibility of individual collagen fibers, close to which the force/stretch behavior stiffens dramatically.

- The osmotic pressure coefficient Π_2: the values used for this constant correspond to reasonable osmotic pressures as can be noted on Figure 3-11. Future experiments of free swelling of cervical specimens at different bath ionic strengths should enable to better isolate the osmotic pressure response of the tissue, and provide more insight on the relevant values to use for Π_2.

- Hydraulic permeability k_D: the values used for this parameter varied between 8×10^{-16} and 1×10^{-14} $m^4 N^{-1} s^{-1}$, which is a little higher, but close to the values measured experimentally for articular cartilage, which range approximately from 1×10^{-16} to 8×10^{-16} $m^4 N^{-1} s^{-1}$ [91].

- GAGs shear modulus μ_G and shear relaxation coefficient $\dot{\gamma}^f$: specific experiments in pure shear will be needed to characterize this parameter more precisely, as its influence on the confined compression behavior is extremely limited, and it moderately affects the unconfined compression response.

- Initial collagen stretch λ_ξ: this parameter is not independent and is determined from the values of $\frac{N k_B T \lambda_L}{3}$ and λ_L characterizing the collagen properties, and Π_2

determining the initial osmotic pressure to be balanced. The values found for this parameter in the two simulations from Figure 4-12 are respectively $\lambda_\xi = 1.334$ for a locking stretch $\lambda_L = 1.43$ in the confined setting, and $\lambda_\xi = 1.67$ for a locking stretch $\lambda_L = 1.732$ in the unconfined setting. These initial stretches are high and place the collagen fibril force/stretch response in the transition zone between a relatively compliant and dramatically stiff response, as illustrated in Figure 3-8 of chapter 3. Future tensile tests will help further characterize the influence of this parameter on the tissue behavior, and its importance in helping the cervix to sustain tensile loading during gestation.

Chapter 5

Conclusions and Recommendations for Future Work

5.1 Concluding Remarks

In conclusion, a fully three-dimensional constitutive model was developed to account for the complex mechanical behavior of human cervical tissue. The model was developed based on the physical structure of the tissue extracellular matrix, which gives the tissue its mechanical properties. The individual contribution of the three major constituents (fibrillar collagen, glycosaminoglycans, and interstitial fluid) has been modeled in accordance to their known structure and intrinsic properties, and has been integrated in the model. The physical basis of the model thus enables to capture the cooperative nature of the response, and identify the contributions of each constituent. This will bring some insight into the underlying mechanisms of the tissue mechanical behavior in normal function, but more importantly should enable the identification of possible causes of failure and provide a better understanding of pathological conditions such as cervical incompetence.

The proposed model accounts for both equilibrium and transient properties of the tissue. The equilibrium properties result from the proteoglycans osmotic pressure and

the stress developed within the collagen network, while the transient effects arise from interstitial fluid flow, modeled with Darcy's law, and proteoglycans shear relaxation. The modelization used to represent the properties of the fibrillar collagen was based on its three-dimensional network properties similar to well-defined classes of polymeric materials. The osmotic properties of the glycosaminoglycans network were modeled using a theoretical expression based on a hybrid solution to the Poisson-Boltzmann equation within a unit cell modeling GAGs-electrolytes interactions, and taking into account molecular structural parameters for the GAG chains as well as their concentration within the tissue and the properties of the interstitial fluid.

The experiments conducted on human cervical samples obtained from hysterectomy specimens enabled a characterization of the tissue mechanical response in both confined and unconfined compression. Finite element simulations realized using the proposed model were able to successfully predict the observed experimental behavior in the two modes of deformation, although large differences noted between the two sets of data did not enable to model the tissue behavior with a single set of constitutive parameters. This variability is most likely due to the limited number of samples tested, and the important variability in the mechanical properties from patient to patient, and from one anatomical location to another for a single patient.

The biochemical tests realized on the samples gave results in accordance with the values found in the literature, and larger quantities of data will enable the identification of correlations between mechanical properties and biochemical structure.

5.2 Recommendations for Future Work

A number of efforts need to be made in order to improve the accuracy and reproducibility of the mechanical tests. As noted on the results presented in chapter 4, the variability in the properties measured experimentally is very important from one sample to the other, including for samples obtained from a single patient. Great care should be taken in the

preparation of the samples, and freezing them before cutting may improve the repeatability of sample geometry, critical to the tests results, especially in confined compression where the sensitivity to small shape variations is particularly large.

If the first priority is to improve test repeatability, a second short term objective should be to perform tests in different modes of deformation on samples from a same patient, and assess the ability of the model capture the experimental behavior in the different configurations tested with a single set of parameters. Biochemical testing and gathering of a larger amount of data should enable identification of relations between these parameters and the biochemical structure of each particular sample, and further validate the model. Additional assays such as collagen extractability, total collagen content measurement, and measurement of the content in certain particular subtypes of glycosaminoglycans may be considered.

Concerning interstitial fluid flow, the implementation of the Darcy's law used in the model was based on a homogeneous permeability across the tissue. A refined model should integrate variations of the permeability with the local parameters of the deformation. Experimental tests using a specially designed compression chamber will enable permeability measurements during mechanical testing, and help characterize the impact of matrix deformation on interstitial flow.

Finally, mechanical tests performed in additional modes of deformation would help to better quantify the impact of the different parameters on the tissue response under physiological conditions, where loading parameters are complex and vary with anatomical location from compressive, shear and tensile conditions. Thus, tension and shear tests might provide very valuable information on the tissue behavior, and help refine the model accordingly.

Appendix A

Numerical Implementation

Chapter 3 defined the mathematical relationships describing the constitutive behavior of the tissue in the present model. This appendix will discuss the practical details of its numerical implementation, as carried out within the UMAT (user material) subroutine of the commercial software ABAQUS 6.3. This appendix will review the time integration scheme adopted for the model. In the procedure followed by ABAQUS to update the material behavior at the integration points from time t to time $t + \Delta t$, a guess for the deformation gradient at time $t + \Delta t$ is provided to the subroutine UMAT , and the subroutine must then update the stress state, $\mathbf{T}$, as well as any internal state variables, and it must provide the material jacobian $\frac{\partial \mathbf{T}}{\partial \mathbf{E}}$ at the end of the increment. As stated in equations (3.8) and (3.9), the different components of the model act in parallel, with a common deformation gradient and a macroscopic total stress equal to the sum of their contributions. Consequently, the time integration of the different elements within the UMAT framework is uncoupled, and can be carried out sequentially to update the material state.

The first section of this appendix will describe the procedure to initialize the material state in its undeformed configuration (at time zero), focusing in particular on the calculation of the initial osmotic pressure and associated collagen isotropic stretch. The following sections will then describe the integration of state for the three components of

the rheological model:

1. The collagen network,

2. The hydrated glycosaminoglycans network,

3. The interstitial fluid flow.

Then a fifth section will be dedicated to the calculation of the material jacobian $\frac{\partial \mathbf{T}}{\partial \mathbf{E}}$.

A.1 Initial Calculations

A.1.1 Initial Osmotic Pressure

The initial osmotic pressure $\Pi_{os}(t = 0)$ is calculated according to equation (3.36):

$$\Pi_{os} = 2\mathcal{R}TC_0 \left[\cosh \left(\frac{9.1 \exp\left(-\kappa R^0 J^{\frac{1}{2}} \right)}{\sqrt{\kappa R^0} J^{\frac{1}{4}}} \right) - 1 \right], \tag{A.1}$$

where the volumetric jacobian J is equal to 1, $\Pi_1 = 2\mathcal{R}TC_0$ is evaluated according to the value of C_0 for the buffer chosen, and $\Pi_2 = \kappa R^0$ is an adjusTable parameter, proportional to the initial GAG concentration of the tissue.

A.1.2 Collagen Stretch

The initial osmotic pressure is balanced by a tensile isotropic stress in the collagen network. The following step then consists in calculating the corresponding initial isotropic stretch in the collagen network λ_ξ, defined by equation (3.19) as

$$\frac{Nk_BT\lambda_L}{3} \frac{1}{\lambda_\xi^3} \left[\frac{\beta_\xi}{\lambda_\xi} \lambda_\xi^2 - \beta_0 \right] + K_C \left(\lambda_\xi^3 - 1 \right) = \Pi_{os}(t = 0), \tag{A.2}$$

where $\beta_\xi = \mathcal{L}^{-1}\left(\frac{\lambda_\xi}{\lambda_L} \right)$, the volumetric jacobian associated with this initial swelling has been replaced by λ_ξ^3, and the principal values of the left Cauchy-Green strain $\mathbf{B}_C$ are all

127

equal to λ_ξ^2. This reduces to

$$\frac{Nk_BT\lambda_L}{3}\frac{1}{\lambda_\xi^3}\left[\beta_\xi\lambda_\xi-\beta_0\right] + K_C\left(\lambda_\xi^3 - 1\right) = \Pi_{os}(t = 0), \tag{A.3}$$

which is solved for λ_ξ using a Newton's method.

At all subsequent times, the effective deformation gradient "seen" by the collagen network is calculated as the macroscopic deformation gradient imposed on the tissue $\mathbf{F}$, multiplied by the isotropic prestretch $\mathbf{V}_\xi = \lambda_\xi\mathbf{I}$.

A.1.3   Initialization of State Variables

The following state variables are used to update the material state over time, and are initialized as:

* $\mathbf{F}_G^f(t = 0) = \mathbf{0}$: no flow in the GAGs network.
* $\dot{\mathbf{F}}_G^f(t = 0) = \mathbf{0}$: zero flow rate of deformation in the GAGs network.
* $\dot{\gamma}_G^f = 0$: zero flow shear strain rate in the GAGs network.
* $\mathbf{F}_C^f(t = 0) = \mathbf{0}$: no flow deformation in the collagen network.
* $\dot{\mathbf{F}}_C^f(t = 0) = \mathbf{0}$: zero flow rate of deformation in the collagen network.
* $\dot{\gamma}_C^f = 0$: zero flow shear strain rate in the collagen network.

A.2   Time-Integration Sequence for the Glycosaminoglycans Network

The time integration scheme for the GAGs network comprises the following steps.

A.2.1 Stress Calculation

i. The flow part of the deformation gradient $\mathbf{F}_G^f$ is updated using an explicit time-integration scheme, according to

$$\mathbf{F}_G^f(t + \Delta t) = \mathbf{F}_G^f(t) + \Delta t \dot{\mathbf{F}}_G^f(t). \tag{A.4}$$

ii. Then the elastic deformation gradient $\mathbf{F}_G^e$ is calculated from the global deformation gradient imposed on the GAGs network $\mathbf{F}_G = \mathbf{F}$, from equation (3.20)

$$\mathbf{F}_G^e(t + \Delta t) = \mathbf{F}(t + \Delta t)\mathbf{F}_G^{f-1}(t + \Delta t). \tag{A.5}$$

iii. The elastic left Cauchy-Green stretch $\mathbf{B}_G^e$ is computed as

$$\mathbf{B}_G^e(t + \Delta t) = \mathbf{F}_G^e(t + \Delta t)\mathbf{F}_G^{e\mathbf{T}}(t + \Delta t). \tag{A.6}$$

iv. The associated Henky strain $\mathbf{E}_G^e$ is given by

$$\mathbf{E}_G^e(t + \Delta t) = \frac{1}{2}\ln \mathbf{B}_G^e(t + \Delta t). \tag{A.7}$$

v. The elastic volumetric jacobian J_G^e is evaluated as

$$J_G^e(t + \Delta t) = det\mathbf{F}_G^e(t + \Delta t) = det\mathbf{F}(t + \Delta t) = J(t + \Delta t). \tag{A.8}$$

vi. The osmotic pressure $\Pi_{os}(t + \Delta t)$ is calculated using (3.36):

$$\Pi_{os}(t + \Delta t) = 2\mathcal{R}TC_0 \left[\cosh\left(\frac{A\exp\left(-\kappa R^0 J^{\frac{1}{2}}\right)}{\sqrt{\kappa R^0 J^{\frac{1}{4}}}} \right) - 1 \right]. \tag{A.9}$$

vii. The shear stress associated with $\mathbf{E}_G^e$ is then added to the pressure term using (3.37)

to obtain for the GAGs Cauchy stress the expression

$$\mathbf{T}_G(t + \Delta t) = \frac{1}{J} \left[2\mu \mathbf{E}_G^e - \frac{2\mu}{3} (tr\mathbf{E}_G^e)\mathbf{I} \right] - \Pi_{os}\mathbf{I}, \qquad (A.10)$$

where the time variable $(t + \Delta t)$ has been omitted on the right hand side to improve clarity.

A.2.2   New Rate of Flow Deformation

viii. The direction and norm of the deviatoric part of the stress are calculated according to (3.43) and (3.44):

$$\mathbf{T}_G'(t + \Delta t) = \mathbf{T}_G - \frac{1}{3}(tr\mathbf{T}_G)\mathbf{I} \qquad (A.11)$$

$$\tau(t + \Delta t) = \sqrt{\frac{1}{2}\mathbf{T}_G' : \mathbf{T}_G'} \qquad \mathbf{N}_G(t + \Delta t) = \frac{1}{\sqrt{2}\tau}\mathbf{T}_G'. \qquad (A.12)$$

ix. The value of the flow shear strain rate $\dot{\gamma}^p$ at the end of the increment is then obtained via (3.45):

$$\dot{\gamma}^f(t + \Delta t) = \dot{\gamma}_0 \tau(t + \Delta t). \qquad (A.13)$$

x. The corresponding rate of stretching $\tilde{\mathbf{D}}_G^f$ follows through (3.42):

$$\tilde{\mathbf{D}}_G^f(t + \Delta t) \;=\; \dot{\gamma}^f \mathbf{N}_G. \qquad (A.14)$$

xi. Finally, the updated value of the flow rate of deformation $\dot{\mathbf{F}}_G^f$ is calculated using (3.40) as:

$$\dot{\mathbf{F}}_G^f(t + \Delta t) = \mathbf{F}_G^{e-1}\tilde{\mathbf{D}}_G^f\mathbf{F}_G. \qquad (A.15)$$

The GAGs network is completely updated at this point.

A.3 Time-Integration Sequence for the Collagen Network

A.3.1 Stress Calculation

Time integration for the collagen network is then carried out as follows. This version of the numerical implementation includes a flow deformation term $\mathbf{F}_C^f$. This term was not used in the simulations presented in chapter 4 ($\mathbf{F}_C^f = \mathbf{I}$ at all times), but will be relevant to model cervical incompetence in future work.

i. The deformation gradient "seen" by the collagen network $\mathbf{F}_C(t + \Delta t)$ is computed from the current deformation gradient for the whole model $\mathbf{F}(t + \Delta t)$, and the initial isotropic stretch $\mathbf{V}_\xi$:

$$\mathbf{F}_C(t + \Delta t) = \mathbf{F}(t + \Delta t)\mathbf{V}_\xi = \lambda_\xi \mathbf{F}(t + \Delta t). \tag{A.16}$$

ii. The flow deformation gradient associated with the collagen network at time $t + \Delta t$ is then updated explicitly from the state variables stored at the end of the previous increment $\mathbf{F}_C^f(t)$ and $\dot{\mathbf{F}}_C^f(t)$:

$$\mathbf{F}_C^f(t + \Delta t) = \mathbf{F}_C^f(t) + \Delta t \dot{\mathbf{F}}_C^f(t). \tag{A.17}$$

iii. The elastic part of the deformation gradient $\mathbf{F}_C^e(t + \Delta t)$ is obtained as

$$\mathbf{F}_C^e(t + \Delta t) = \mathbf{F}_C(t + \Delta t)\mathbf{F}_C^{f-1}(t + \Delta t). \tag{A.18}$$

iv. The associated left Cauchy-Green strain $\mathbf{B}_C^e(t + \Delta t)$ is calculated through

$$\mathbf{B}_C^e(t + \Delta t) = \mathbf{F}_C^e(t + \Delta t)\mathbf{F}_C^{eT}(t + \Delta t). \tag{A.19}$$

131

v. The resulting chain stretch in the 8-fibril unit cell is calculated from equation (3.13):

$$\lambda_c(t + \Delta t) = \sqrt{\frac{\lambda_1^2 + \lambda_2^2 + \lambda_3^2}{3}} = \sqrt{\frac{tr\mathbf{B}_C^e(t + \Delta t)}{3}}. \tag{A.20}$$

vi. $\beta_c(t + \Delta t) = \mathcal{L}^{-1}\left(\frac{\lambda_c(t+\Delta t)}{\sqrt{n}}\right)$ and the elastic volumetric jacobian $J_C^e(t + \Delta t) = det\mathbf{F}_C^e(t + \Delta t)$ are evaluated, and the stress in the collagen network $\mathbf{T}_C(t + \Delta t)$ is finally obtained through equation (3.19):

$$\mathbf{T}_C(t + \Delta t) = \frac{Nk_BT\lambda_L}{3}\frac{1}{J_C^e}\left[\frac{\beta_c}{\lambda_c}\mathbf{B}_C^e - \beta_0\mathbf{I}\right] + K_C\left(J_C^e - 1\right)\mathbf{I}, \tag{A.21}$$

where the time variable $(t + \Delta t)$ has been omitted on the right-hand side of the equation.

A.3.2 New Flow Rate of Deformation

The time derivative of the flow deformation gradient $\dot{\mathbf{F}}_C^f$ at the end of the increment is then calculated from the current state of stress:

vii. First the norm σ_C of the Cauchy stress is evaluated as

$$\sigma_C(t + \Delta t) = \sqrt{\mathbf{T}_C : \mathbf{T}_C} = \sqrt{T_{Cij}T_{Cij}}. \tag{A.22}$$

viii. The value of the flow shear strain rate is updated as

$$\dot{\gamma}_C^f(t + \Delta t) = \dot{\gamma}_C^0\left[\sigma_C\right]^{\frac{1}{m}}. \tag{A.23}$$

ix. The corresponding rate of stretching $\tilde{\mathbf{D}}_C^f$ follows through

$$\tilde{\mathbf{D}}_C^f(t + \Delta t) = \frac{\dot{\gamma}_C^f}{\sigma_C}\mathbf{T}_C. \tag{A.24}$$

xi. Finally, the updated value of the flow rate of deformation $\dot{\mathbf{F}}_C^f$ is calculated using (3.40) as

$$\dot{\mathbf{F}}_C^f(t + \Delta t) = \mathbf{F}_C^{e-1}\tilde{\mathbf{D}}_C^f\mathbf{F}_C.$$ (A.25)

This completes time integration for the collagen network.

A.4 Numerical Treatment of the Interstitial Fluid Flow Problem

The equations governing interstitial fluid flow has been established in section 3.5. The transient fluid pressure is the solution to equation (3.54) with appropriate boundary conditions:

$$\chi_f \frac{\partial P_f}{\partial t} = k_D \nabla^2 P_f - tr\mathbf{D}.$$ (A.26)

This equation is a diffusion equation analogous to the field equation governing a heat transfer problem including a source term.

Table (A.1) establishes the correspondence between the respective variables and parameters in the two problems.

	Interstitial Flow	**Heat Transfer**
Equation	$\chi_f \frac{\partial P_f}{\partial t} = k_D \nabla^2 P_f - tr\mathbf{D}$	$\rho c \frac{\partial T}{\partial t} = k\nabla^2 T + r_{gen}$
Variable	P_f = pore fluid pressure	T = temperature
Storage modulus	χ_w = water bulk modulus	ρc where ρ = density and c = specific heat
Conductivity	k_D = Darcy's permeability	k = thermal conductivity
Source term	$-tr\mathbf{D}$ = volume source term	r_{gen} = heat source term

Table A.1: Correspondence between interstitial fluid flow and heat transfer problem.

Advantage is taken of this correspondence in the finite element implementation. The problem is treated as a coupled thermal-mechanical problem, where the coupling appears in the heat source term, which depends on the macroscopic rate of volume change $tr\mathbf{D}$.

Coupled temperature-displacement elements are used for the simulations, and the solution obtained for the temperature field can be interpreted as interstitial fluid pressure. For coupled temperature-displacement analysis, ABAQUS require that the variation of the total Cauchy stress with temperature $\frac{\partial \mathbf{T}}{\partial \theta}$, as well as the variation of the heat source term with strain $\frac{\partial r_{gen}}{\partial \mathbf{E}_t}$, be provided within the UMAT, in addition to the material Jacobian $\frac{\partial \mathbf{T}}{\partial \mathbf{E}}$.

A.5 Material Jacobian $\frac{\partial \mathbf{T}}{\partial \mathbf{E}}$ and Temperature Coupled Terms

A.5.1 UMAT Conventions and Notations

ABAQUS uses a Newton-Raphson iteration scheme to find the equilibrium solution at each time increment, and requires that the material jacobian $\frac{\partial \mathbf{T}}{\partial \mathbf{E}}$ be provided within the UMAT subroutine. The material jacobian used in ABAQUS is defined as

$$\mathbb{J} = \frac{\partial \mathbf{T}}{\partial \mathbf{E}_t}, \tag{A.27}$$

where $\mathbf{T}$ is the Cauchy stress in the material at the end of the increment, and $\mathbf{E}_t$ corresponds to the incremental strain tensor. The strain measure used by ABAQUS corresponds to the logarithmic strain, so that the incremental strain is approximately equal to

$$\mathbf{E}_t \approx \ln \mathbf{U}_t, \tag{A.28}$$

where $\mathbf{U}_t$ is the incremental right stretch tensor, which results from the polar decomposition of the relative deformation gradient between times t (beginning of the increment)

and $t + \Delta t$ (end of the increment):

$$\mathbf{F}_t \quad = \quad \mathbf{R}_t \mathbf{U}_t, \tag{A.29}$$

$$\mathbf{F}(t + \Delta t) \quad = \quad \mathbf{F}_t \mathbf{F}(t). \tag{A.30}$$

ABAQUS does not store the 9 components of the symmetric stress and strain tensors, but only the 6 independent ones, such that the following compact vectorial representations are adopted to represent $\mathbf{E}_t$ and $\mathbf{T}$:

$$\underline{e}_t = \begin{pmatrix} E_{t11} \\ E_{t22} \\ E_{t33} \\ 2E_{t12} \\ 2E_{t13} \\ 2E_{t13} \end{pmatrix} \qquad \underline{t} = \begin{pmatrix} T_{11} \\ T_{22} \\ T_{33} \\ 2T_{12} \\ 2T_{13} \\ 2T_{13} \end{pmatrix} \tag{A.31}$$

As a result of these conventions, the material jacobian required in the UMAT subroutine is provided as a (6x6) matrix $\mathbf{J}$ instead of the fourth order tensor $\mathbb{J}$ from equation (A.27), defined as

$$\mathbf{J} = \frac{\partial \underline{t}}{\partial \underline{e}_t}. \tag{A.32}$$

A.5.2   Derivation of J

The Cauchy stress in the model is evaluated from the separate contributions of the collagen network, the GAGs, and the interstitial fluid flow according to equation (3.9):

$$\mathbf{T}_{tissue} = \mathbf{T}_{C} + \mathbf{T}_{G} - P_{fluid}\mathbf{I}, \tag{A.33}$$

135

the compact representation of which is

$$\underline{t}_{tissue} = \underline{t}_{\mathrm{C}} + \underline{t}_{\mathrm{G}} - P_{fluid}\underline{i},$$ (A.34)

where $\underline{i}$ is the vector associated to the identity tensor $\underline{i}= \begin{pmatrix} 1 \\ 1 \\ 1 \\ 0 \\ 0 \\ 0 \end{pmatrix}$, and $\underline{t}_{\mathrm{C}}$ and $\underline{t}_{\mathrm{G}}$ are the

respective compact representations of $\mathbf{T}_{\mathrm{C}}$ and $\mathbf{T}_{\mathrm{G}}$.

Here the fluid pressure P_{fluid} is the pressure guess for the end of the current increment $(t + \Delta t)$, and does not depend on the current strain increment $\underline{e}_t$. The material jacobian $\mathbf{J} = \frac{\partial \underline{t}_{tissue}}{\partial \underline{e}_t}$ can therefore be calculated as the sum of the individual Jacobians for the collagen and the GAGs, while the contribution of the fluid pressure is included in the temperature part of the jacobian described in the next section. We therefore have:

$$\mathbf{J} = \frac{\partial \underline{t}}{\partial \underline{e}_t} = \frac{\partial \underline{t}_{\mathrm{C}}}{\partial \underline{e}_t} + \frac{\partial \underline{t}_{\mathrm{G}}}{\partial \underline{e}_t} = \mathbf{J}_{\mathrm{C}} + \mathbf{J}_{\mathrm{G}}.$$ (A.35)

Jacobian for the Collagen Network $\mathbf{J}_{\mathrm{C}}$

The stress for the collagen network is given by

$$\underline{t}_{\mathrm{C}} = \frac{Nk_BT\lambda_L}{3} \frac{1}{J_{\mathrm{C}}^e} \left[\frac{\beta_{\mathrm{C}}}{\lambda_{\mathrm{C}}} \underline{b}_{\mathrm{C}}^e - \beta_0\underline{i} \right],$$ (A.36)

136

where the compact representation adopted for $\mathbf{B}_C^e$ is identical to that of ABAQUS:

$$\underline{\mathbf{b}}_C^e = \begin{pmatrix} B_{C11}^e \\ B_{C22}^e \\ B_{C33}^e \\ 2B_{C12}^e \\ 2B_{C13}^e \\ 2B_{C23}^e \end{pmatrix}.$$

The calculation of $\mathbf{J}_C$ can therefore be decomposed in the following way:

$$\mathbf{J}_C = \frac{Nk_BT\lambda_L}{3}\frac{1}{J_C^e}\left[\underline{\mathbf{b}}_C^e \otimes \frac{\partial\left(\frac{\beta_c}{\lambda_c}\right)}{\partial\underline{e}_t} + \frac{\beta_c}{\lambda_c}\frac{\partial\underline{\mathbf{b}}_C^e}{\partial\underline{e}_t}\right] - \frac{1}{J_C^e}\mathbf{t}_C \otimes \frac{\partial J_C^e}{\partial\underline{e}_t}, \qquad (A.37)$$

where we introduce the following intermediate variables:

$$\chi = \frac{d\left(\frac{\beta_c}{\lambda_c}\right)}{d\lambda_c} \quad ; \quad \underline{z} = \frac{\partial\lambda_c}{\partial\underline{\mathbf{b}}_C^e} \quad ; \quad \mathbf{H} = \frac{\partial\underline{\mathbf{b}}_C^e}{\partial\underline{e}_t}$$

$$\frac{\partial\left(\frac{\beta_c}{\lambda_c}\right)}{\partial\underline{e}_t} = \frac{d\left(\frac{\beta_c}{\lambda_c}\right)}{d\lambda_c}\frac{\partial\lambda_c}{\partial\underline{\mathbf{b}}_C^e}\frac{\partial\underline{\mathbf{b}}_C^e}{\partial\underline{e}_t} = y\underline{z}\mathbf{H} \quad ; \quad \underline{q} = \frac{\partial J_C^e}{\partial\underline{e}_t}$$

- $\chi = \frac{d\left(\frac{\beta_c}{\lambda_c}\right)}{d\lambda_c}$

We have $\beta_c = \mathcal{L}^{-1}\left(\frac{\lambda_c}{\sqrt{n}}\right) = \mathcal{L}^{-1}\left(\frac{\lambda_c}{\lambda_L}\right)$, which gives

$$\frac{d\beta_c}{d\lambda_c} = \frac{1}{\lambda_L\mathcal{L}'(\beta_c)}, \qquad (A.38)$$

where $\mathcal{L}'(x)$ is the derivative of the Langevin function $\mathcal{L}(x) = \coth x - \frac{1}{x}$. We have

$$\mathcal{L}'(\beta_c) = -\frac{1}{\sinh^2(\beta_c)} + \frac{1}{\beta_c^2}, \qquad (A.39)$$

137

giving

$$\frac{d\beta_c}{d\lambda_c} = \frac{1}{\lambda_L}\left(\frac{1}{\beta_c^2} - \frac{1}{\sinh^2(\beta_c)}\right).$$ (A.40)

Finally,

$$\chi = \frac{1}{\lambda_c}\frac{d\beta_c}{d\lambda_c} - \frac{\beta_c}{\lambda_c^2} = \frac{1}{\lambda_L\lambda_c}\left(\frac{1}{\beta_c^2} - \frac{1}{\sinh^2(\beta_c)} - \beta_c\frac{\lambda_L}{\lambda_c}\right).$$ (A.41)

- $\underline{z} = \frac{\partial\lambda_c}{\partial\underline{b}_C^e}$

Equation (3.13) defines the collagen fibril stretch λ_c as

$$\lambda_c = \sqrt{\frac{tr\mathbf{B}_C^e}{3}} = \sqrt{\frac{b_{C1}^e + b_{C2}^e + b_{C3}^e}{3}}.$$

The vector $\underline{z}$ is thus easily given by

$$\underline{z} = \begin{pmatrix} \frac{1}{6\lambda_c} & \frac{1}{6\lambda_c} & \frac{1}{6\lambda_c} & 0 & 0 & 0 \end{pmatrix}.$$ (A.42)

- $\mathbf{H} = \frac{\partial\underline{b}_C^e}{\partial\underline{e}_t}$

We have

$$\mathbf{B}_C^e(t+\Delta t) = \mathbf{F}_C^e(t+\Delta t)\mathbf{F}_C^{eT}(t+\Delta t) = \mathbf{F}_C(t+\Delta t)\mathbf{F}_C^{f-1}(t+\Delta t)\mathbf{F}_C^{f-T}(t+\Delta t)\mathbf{F}_C^T(t+\Delta t).$$ (A.43)

The deformation gradient at the end of the increment (time $t + \Delta t$) is related to the deformation gradient at the beginning of the increment through

$$\mathbf{F}_C(t+\Delta t) = \lambda_\xi\mathbf{F}(t+\Delta t) = \lambda_\xi\mathbf{F}_t\mathbf{F}(t) = \mathbf{F}_t\mathbf{F}_C(t),$$ (A.44)

where $\mathbf{F}_t$ is the global incremental deformation gradient. The polar decomposition of $\mathbf{F}_t$ in incremental rotation and stretch tensors $\mathbf{F}_t = \mathbf{R}_t\mathbf{U}_t$ combined with (A.43) and (A.44) gives the following expression for $\mathbf{B}_C^e$:

$$\mathbf{B}_C^e(t+\Delta t) = \mathbf{R}_t\mathbf{U}_t\mathbf{F}_C(t)\mathbf{F}_C^{f-1}(t+\Delta t)\mathbf{F}_C^{f-T}(t+\Delta t)\mathbf{F}_C^T(t)\mathbf{U}_t\mathbf{R}_t^T.$$ (A.45)

The explicit integration scheme used for the plastic deformation gradient as explained in section A.3.1 (equation (A.17)) makes it independent of the incremental stretch. The infinitesimal variation in the elastic left Cauchy-Green stretch $d\mathbf{B}_C^e$ is thus related to the infinitesimal variation in the incremental stretch $d\mathbf{U}_t$ through

$$
\begin{aligned}
d\mathbf{B}_C^e &= \mathbf{R}_t d\mathbf{U}_t \mathbf{F}_C(t) \mathbf{F}_C^{f-1}(t + \Delta t) \mathbf{F}_C^{f-\mathbf{T}}(t + \Delta t) \mathbf{F}_C^{\mathbf{T}}(t) \mathbf{U}_t \mathbf{R}_t^{\mathbf{T}} \\
&\quad + \mathbf{R}_t \mathbf{U}_t \mathbf{F}_C(t) \mathbf{F}_C^{f-1}(t + \Delta t) \mathbf{F}_C^{f-\mathbf{T}}(t + \Delta t) \mathbf{F}_C^{\mathbf{T}}(t) d\mathbf{U}_t \mathbf{R}_t^{\mathbf{T}}.
\end{aligned}
\tag{A.46}
$$

The accuracy of the jacobian $\mathbf{J}$ only influences the speed of convergence to the solution, however it does not affect the solution itself, and approximations will be made here to simplify the calculations. Replacing the incremental rotation tensor $\mathbf{R}_t$ by the identity tensor, and the deformation gradient $\mathbf{F}_C(t)$ by its value at the end of the increment $\mathbf{F}_C(t + \Delta t)$, we obtain the following first order approximation:

$$
d\mathbf{B}_C^e = d\mathbf{U}_t \mathbf{B}_C^e(t + \Delta t) + \mathbf{B}_C^e(t + \Delta t) d\mathbf{U}_t,
\tag{A.47}
$$

which should remain very satisfactory for reasonably small time steps.

The incremental stretch is related to the incremental strain $\mathbf{E}_t$ via $\mathbf{E}_t \approx \ln \mathbf{U}_t$, which reduces to

$$
\mathbf{E}_t \approx \mathbf{U}_t - \mathbf{I}
\tag{A.48}
$$

as a first order approximation, leading to

$$
d\mathbf{E}_t \approx d\mathbf{U}_t.
\tag{A.49}
$$

This transforms equation (A.47) into

$$
d\mathbf{B}_C^e \approx d\mathbf{E}_t \mathbf{B}_C^e + \mathbf{B}_C^e d\mathbf{E}_t,
\tag{A.50}
$$

from which the full fourth order form $\mathbb{H} = \frac{\partial \mathbf{B}_C^e}{\partial \mathbf{E}_t}$ of tensor $\mathbf{H}$ can easily be derived. Equation

(A.50) written in components yields

$$dB^e_{Cij} \approx dE_{tip}B^e_{Cpj} + B^e_{Cip}dE_{tpj} = dE_{tpj}\left(\delta_{ik}\delta_{pl}B^e_{Ckj} + \delta_{pk}\delta_{jl}B^e_{Cik}\right) = dE_{tkl}\left(\delta_{pl}B^e_{Cij} + \delta_{jl}B^e_{Cip}\right),$$

(A.51)

and $\mathbb{H}$ is given by

$$H_{ijkl} = \frac{\partial B^e_{Cij}}{\partial E_{tkl}} \approx \delta_{pl}B^e_{Cij} + \delta_{jl}B^e_{Cip}.$$

(A.52)

The symmetrization of this expression using the compact representations finally gives

$$\mathbf{H} = \begin{pmatrix} 2b^e_{C1} & 0 & 0 & \frac{1}{2}b^e_{C4} & \frac{1}{2}b^e_{C5} & 0 \\ 0 & 2b^e_{C2} & 0 & \frac{1}{2}b^e_{C4} & 0 & \frac{1}{2}b^e_{C6} \\ 0 & 0 & 2b^e_{C3} & 0 & \frac{1}{2}b^e_{C5} & \frac{1}{2}b^e_{C6} \\ b^e_{C4} & b^e_{C4} & 0 & \frac{1}{2}\left(b^e_{C1}+b^e_{C2}\right) & \frac{1}{2}b^e_{C6} & \frac{1}{2}b^e_{C5} \\ b^e_{C5} & 0 & b^e_{C5} & \frac{1}{2}b^e_{C6} & \frac{1}{2}\left(b^e_{C1}+b^e_{C3}\right) & \frac{1}{2}b^e_{C4} \\ 0 & b^e_{C6} & b^e_{C6} & \frac{1}{2}b^e_{C5} & \frac{1}{2}b^e_{C4} & \frac{1}{2}\left(b^e_{C2}+b^e_{C3}\right) \end{pmatrix}.$$

(A.53)

- $\underline{q} = \frac{\partial J^e_C}{\partial \underline{e}_t}$

We have

$$J^e_C = det\mathbf{F}^e_C = det\mathbf{F}_C(t+\Delta t)det\mathbf{F}^{f-1}_C(t+\Delta t),$$

(A.54)

where $det\mathbf{F}_C(t+\Delta t)$ can be further decomposed into $det\mathbf{F}_C(t+\Delta t) = det\mathbf{U}_t det\mathbf{F}_C(t)$ as $det\mathbf{R}_t = 1$. The derivative of the determinant of the tensor $\mathbf{U}_t$ with respect to it components is given by

$$\frac{\partial det\mathbf{U}_t}{\partial \mathbf{U}_t} = \left(det\mathbf{U}_t\right)\mathbf{U}^{-\mathbf{T}}_t.$$

(A.55)

Combined with (A.54), this gives

$$\frac{\partial J^e_C}{\partial \mathbf{U}_t} = J^e_C\mathbf{U}^{-\mathbf{T}}_t,$$

(A.56)

140

so that

$$\frac{\partial J_C^e}{\partial \mathbf{E}_t} = \frac{\partial J_C^e}{\partial \mathbf{U}_t}\frac{\partial \mathbf{U}_t}{\partial \mathbf{E}_t} \approx J_C^e \mathbf{U}_t^{-\mathbf{T}}, \tag{A.57}$$

using once again the first order approximation $\frac{\partial \mathbf{U}_t}{\partial \mathbf{E}_t} \approx \mathbb{I}$. Further simplifying equation (A.57) by approximating $\mathbf{U}_t$ with the identity $\mathbf{I}$, in order to avoid the polar decomposition of $\mathbf{F}_t$, we obtain

$$\frac{\partial J_C^e}{\partial \mathbf{E}_t} \approx J_C^e \mathbf{I}, \tag{A.58}$$

which, in compact representation, reduces to

$$\underline{\mathbf{q}} = \frac{\partial J_C^e}{\partial \underline{\mathbf{e}}_t} \approx \begin{pmatrix} J_C^e & J_C^e & J_C^e & 0 & 0 & 0 \end{pmatrix}. \tag{A.59}$$

This completes the calculations for the collagen jacobian $\mathbf{J}_C$.

Jacobian for the GAGs Network $\mathbf{J}_G$

The stress for the GAGs network is given by

$$\underline{\mathbf{t}}_G = \underbrace{\frac{1}{J}\left[2\mu\underline{\mathbf{e}}_G^e - \frac{2\mu}{3}\left(tr\mathbf{E}_G^e\right)\underline{\mathbf{i}}\right]}_{\underline{\mathbf{t}}_G^{shear}} - \Pi_{os}(J)\underline{\mathbf{i}}, \tag{A.60}$$

where the same conventions have been kept for the compact representations, and the elastic strain tensor $\mathbf{E}_G^e$ is defined by

$$\mathbf{E}_G^e = \ln \mathbf{V}_G^e = \frac{1}{2}\ln \mathbf{B}_G^e = \frac{1}{2}\ln \mathbf{F}_G^e \mathbf{F}_G^{e\mathbf{T}}. \tag{A.61}$$

The jacobian associated with the GAGs part of the model is consequently composed of two contributions: the elastic shear response and the osmotic pressure. We have

$$\mathbf{J}_G = \mathbf{J}_G^e + \mathbf{J}_G^{os}. \tag{A.62}$$

• Shear response

141

For small elastic rotations ($\mathbf{R}_G^e \approx \mathbf{I}$), the term $\mathbf{J}_G^e$ is well approximated by the elastic Jacobian $\frac{\partial \underline{t}_G^{shear}}{\partial \underline{e}_G^e}$, so that:

$$\mathbf{J}_G^e \approx \frac{\partial \underline{t}_G^{shear}}{\partial \underline{e}_G^e} = \begin{pmatrix} \frac{4\mu}{3} & -\frac{2\mu}{3} & -\frac{2\mu}{3} & 0 & 0 & 0 \\ -\frac{2\mu}{3} & \frac{4\mu}{3} & -\frac{2\mu}{3} & 0 & 0 & 0 \\ -\frac{2\mu}{3} & -\frac{2\mu}{3} & \frac{4\mu}{3} & 0 & 0 & 0 \\ 0 & 0 & 0 & 2\mu & 0 & 0 \\ 0 & 0 & 0 & 0 & 2\mu & 0 \\ 0 & 0 & 0 & 0 & 0 & 2\mu \end{pmatrix}. \tag{A.63}$$

• Osmotic pressure

The osmotic pressure contribution to the stress only depends on the global volumetric jacobian, and is given by

$$\underline{t}_G^{os}(J) = -\Pi_{os}(J)\underline{i} = -2\mathcal{R}TC_0 \left[\cosh\left(\frac{A\exp\left(-\kappa R^0 J^{1/2}\right)}{\sqrt{\kappa R^0 J^{1/4}}} \right) - 1 \right] \underline{i}, \tag{A.64}$$

which will be rewritten as

$$\underline{t}_G^{os}(J) = -\Pi_1 \left[\cosh\left(\frac{A\exp{-\alpha(J)}}{\sqrt{\alpha(J)}} \right) - 1 \right] \underline{i}, \tag{A.65}$$

where the function $\alpha(J) = \kappa R^0 \sqrt{J} = \Pi_2 \sqrt{J}$ has been introduced to simplify the expression.

The corresponding contribution to the material jacobian is expressed as

$$\mathbf{J}_G^{os} = -\frac{\partial \Pi_{os}}{\partial J} \underline{i} \otimes \frac{\partial J}{\partial \underline{e}_t}, \tag{A.66}$$

where the derivative of J with respect to the incremental strain $\underline{e}_t$ can be obtained following the same approach used to obtain the expression for $\mathbf{q}$ in the collagen

142

network (A.59):

$$\frac{\partial J}{\partial \underline{\epsilon}_t} \approx \begin{pmatrix} J & J & J & 0 & 0 & 0 \end{pmatrix}.$$ (A.67)

Finally, the derivative $\frac{\partial \Pi_{os}}{\partial J}$ is calculated as

$$\frac{\partial \Pi_{os}}{\partial J} = -\frac{\Pi_1 A}{2J} \left[\sqrt{\alpha(J)} + \frac{1}{2\sqrt{\alpha(J)}} \right] \exp -\alpha(J) \sinh \left(\frac{A \exp -\alpha(J)}{\sqrt{\alpha(J)}} \right).$$ (A.68)

This completes the calculations for the GAGs jacobian $\mathbf{J_G}$.

A.5.3 Temperature Coupling Terms

Temperature Dependence of the Cauchy Stress

The temperature is equivalent to the interstitial fluid pressure in this coupled temperature-displacement analysis, and its contribution to the total Cauchy stress in the tissue is:

$$\underline{t}_{fluid} = -P_{fluid}\underline{i} = -\theta\underline{i}.$$ (A.69)

The corresponding Jacobian $\underline{j}_\theta = \frac{\partial \underline{t}}{\partial \theta}$ is simply given by

$$\underline{j}_\theta = \begin{pmatrix} -1 & -1 & -1 & 0 & 0 & 0 \end{pmatrix}.$$ (A.70)

Strain Dependence of the Heat Source Term

In this coupled analysis, the temperature affects the stress, but the temperature field is in return dependent on the state of the deformation through the heat source term r_{gen}, defined in Table (A.1) as

$$r_{gen} = -tr\mathbf{D} = -\frac{\dot{J}}{J}.$$ (A.71)

The source term is approximated as

$$r_{gen} = -\frac{det\mathbf{F}(t + \Delta t) - det\mathbf{F}(t)}{det\mathbf{F}(t)\Delta t},$$ (A.72)

143

where Δt is the fixed time increment. Substituting $det\mathbf{F}(t + \Delta t) = det\mathbf{F}(t)det\mathbf{U}_t$, this expression simplifies to

$$r_{gen} = \frac{1 - det\mathbf{U}_t}{\Delta t}. \tag{A.73}$$

Using again the same approach followed for the evaluation of $\underline{q}$ (A.59), we obtain

$$\frac{\partial det\mathbf{U}_t}{\partial \underline{e}_t} = \frac{1}{det\mathbf{F}(t)}\frac{\partial J}{\partial \underline{e}_t} \approx \frac{J}{det\mathbf{F}(t)}\underline{i} = det\mathbf{U}_t\underline{i}. \tag{A.74}$$

Finally, combining equations (A.73) and (A.74), $\frac{\partial r_{gen}}{\partial \underline{e}_t}$ is given by

$$\frac{\partial r_{gen}}{\partial \underline{e}_t} = \frac{-det\mathbf{U}_t}{\Delta t}\underline{i} = \left(r_{gen} - \frac{1}{\Delta t}\right)\underline{i}. \tag{A.75}$$

This completes the calculations for the coupled temperature problem.

Appendix B

Biochemical Protocols

B.1 Collagen Assay

B.1.1 Protocol

The collagen content was assessed by measuring the hydroxyproline concentration in the tissue samples after proteinase K and hydrochloric acid digestion, according to the following protocol. The small tissue cylinders to be tested were freeze-dried for 24 hours after wet weight was recorded. Dry weight was then recorded, and the samples were dissected into small pieces using a scalpel blade. Small amounts between 3 and 10 mg approximately were taken and subjected to the following steps:

- digestion in 1 mL of proteinase K solution (3 mg/mL) for 48 hours in a 60°C bath.

- 100 μL were taken and diluted to 1 mL by adding 900 μL of 6N HCl solution, and transferred in Pyrex tubes with Teflon coated caps to resist to oven temperature.

- The tubes containing 1 mL each were left in the oven during 24 hours for digestion at a temperature of 118°C.

- The hydrolyzed samples were allowed to cool down to room temperature and vortexed to collect liquid drops on the sides.

- Under the fume hood, 1-2 of methyl red indicator were added, and the pH was neutralized by adding successively to each tube 2 mL of 2.5 M NaOH solution followed by 0.5 mL of 6N HCl, and a few drops of 0.5M NaOH for final adjustment.

- Samples were diluted up to a final volume of 15 mL by adding deionized water, and 1 mL was taken from each sample and deposited in a disposable glass tube.

- Standard solutions of known hydroxyproline concentration were prepared. 1 mL of each standard solution was taken. The concentrations of the standards are given in Table B.1.

- Samples and standards were both subjected to the remaining steps.

- Under the fume hood, 0.5 mL of Chloramine-T (composition given below) were added to each tube followed by vortexing. Caps were placed to prevent evaporation, and the samples were left 20 minutes for reaction at room temperature.

- Then, 0.5 mL of pDAB solution were added to each tube while vortexing until no visible milky white precipitate was visible.

- Caps were replaced and the tubes were transferred in a 60°C fluid bath and left there 30 minutes for incubation.

- The samples were placed in a tub of cool water for approximately 5 minutes to bring them down to room temperature.

- 200 μL of each sample and standard were deposited on a microplate for light absorption measurement.

- Absorption at a wavelength $\lambda = 560$ nm was read using an appropriate spectrophotometer.

A standard curve (best linear fit) was constructed from the standard solutions, relating hydroxyproline concentration to absorption values. The hydroxyproline concentrations of

the samples were deduced, and hydroxyproline concentration in mg/dry weight of tissue was obtained after multiplication by the appropriate dilution factors, and division by the initial sample weight.

The reported collagen concentrations were obtained according to the formula:

$$[collagen] = [hydroxyproline] * \frac{100}{14}.$$

B.1.2 Solutions Used

(i) Chloramine-T solution: 0.705 g Chloramine-T, 40 mL of below pH 6 buffer solution, 5 mL Isopropyl Alcohol.

(ii) pDAB solution (p-Dimethylaminobenzaldehyde): 7.5 g pDAB, 30 mL Isopropyl Alcohol.

(iii) pH 6 buffer solution: 17 g NaOH, 25 g Citric Acid Monohydrate, 36.17 g Na Acetate Anhydrate, 6 mL Glacial Acetic Acid, 150 mL Isopropyl Alcohol, 600 mL deionized water, 5 drops Toluene.

(iv) Hydroxyproline standard solutions in deionized water at the concentrations given in Table B.1.

Standard #	1	2	3	4	5	6	7
[OH-proline] (μg/mL)	0.0	0.5	1.0	2.0	3.0	4.0	5.0

Table B.1: Hydroxyproline standard solutions concentrations.

B.2 Glycosaminoglycans Assay

Total GAGs content was measured on the samples by DMB-dye binding assay, after digestion in proteinase K as described in the collagen assay protocol (48 hours at 60°C in 1 mL of 3mg/mL proteinase K solution), according to the following steps:

- 7 standard solutions of chondroitin 6-sulfate in PBE were prepared. The concentrations are given in Table B.2.

- 20 μL of each standard and digested sample were transferred into a 96-well microplate, and 200 μL of DMB-dye solution were added to each well.

- Absorption at a wavelength $\lambda = 520$ nm was measured.

A standard curve (best second order polynomial fit) was constructed from the standard solutions, relating GAGs concentration to absorption values.

Standard #	1	2	3	4	5	6	7
[Chondroitin 6-sulfate] (μg/mL)	100	50	25	12.5	6.25	3.125	0.0

Table B.2: GAGs standard solutions concentrations.

Bibliography

[1] Creasy R.K., *Preterm Labor and Delivery*, in Maternal-Fetal Medicine: Principles and Practice, 3rd ed. Philadelphia, W.B. Saunders, (1994), 494-520.

[2] Craigo S., *Cervical Incompetence and Preterm Delivery*, New Engl. J. of Med. **334(9)**, (1996), 595-596.

[3] Wood N.S., Marlow N. et al, *Neurologic and Developmental Disability after Extremely Preterm Birth*, N. Engl. J. Med. **343(6)**, (2000), 378-384.

[4] Jewelewicz R., *Incompetent Cervix: Pathogenesis, Diagnosis and Treatment*, Seminars in Perinatology **15(2)**, (1991), 156-161.

[5] Edozien L.C., *The Incompetent Cervix - A Review*, Br J Clin Pract **46(4)**, (1992), 264-7.

[6] Iams J.D., *Cervical Incompetence*, in Maternal-Fetal Medicine: Principles and Practice, 4th ed. Philadelphia, W.B. Saunders, (1999), 445-460.

[7] Cousins L., *Cervical Incompetence, 1980: a Time for Re-appraisal*, Clin. Obstet. Gynaecol. **23**, (1980), 467-477.

[8] Iams J.D., Johnson F.F. et al, *Cervical Competence as a Continuum: A Study of Ultrasonographic Cervical Length and Obstetric Performance*, Am. J. Obstet. Gynecol. **172**, (1995), 1097-106.

[9] Iams J.D., Goldenberg R.L., Meis P.J. et al, *The Length of the Cervix and the Risk of Spontaneous Premature Delivery*, N. Engl. J. Med. **334(9)**, (1996), 567-572.

[10] Gabbe S.G., Niebyl J.R. and Simpson J.L., *Abnormal Cervical Competence*, in Obstetrics: Normal and Problem Pregnancies, 3rd ed., Churchill Livingstone, (1996), 785-792.

[11] Buckingham J.C., Buethe RA et al, *Collagen-Muscle Ratio in Clinically Normal and Clinically Incompetent Cervices*, Am. J. Obstet. Gynecol. **91**, (1965), 231-237.

[12] Rechberger T., Uldbjerg N. et al, *Connective Tissue Changes in the Cervix During Normal Pregnancy and Pregnancy Complicated by Cervical Incompetence*, Obstet. Gynecol. **71**, (1988), 563-567.

[13] Petersen K.L., Uldbjerg N., *Cervical Collagen in Non-Pregnant Women with Previous Cervical Incompetence*, Eur. J. Obstet. Gynecol. and Reprod. Biol. **67**, (1996), 41-45.

[14] Shearman A.I., *Hormonal Therapy for Control of the Incompetent Cervical Os*, Obstet. Gynecol. **28**, (1966), 198-205.

[15] Shirodkar V.N., *A New Method of Operative Treatment for Habitual Abortions in the Second Trimester of Pregnancy*, Antiseptic **52**, (1955), 229-235.

[16] McDonald I.A., *Suture of the Cervix for IneviTable Miscarriage*, J. Obstet. Gynecol. Br. Emp. **64**, (1957), 346-350.

[17] Novy M.J., *Transabdominal Cervicoisthmic Cerclage for the Management of Repetitive Abortion and Premature Delivery*, Am. J. Obstet. Gynecol. **143**, (1982), 44-54.

[18] Novy M.J., *Transabdominal Cervicoisthmic Cerclage: a Reappraisal 25 Years After its Introduction*, Am. J. Obstet. Gynecol. **164**, (1991), 1635-41.

[19] Craig S., Fliegner J.R., *Treatment of Cervical Incompetence by Transabdominal Cervicoisthmic Cerclage*, Aust. N. Z. J. Obstet. Gynaecol. **37**, (1997), 407-11.

[20] Baden W.F. and Baden E.E., *Cervical Incompetence: Current Therapy*, Am. J. Obstet. Gynecol. **79**, (1960), 545-552.

[21] Lazar P., Servent B., Dreyfus J., Gueguen S. and Papiernik E., *Comparison of Two Successive Policies of Cervical Cerclage for Prevention of Preterm Birth*, Eur. J. Obstet. Gynecol. Reprod. Biol. **9**, (1979), 307-312.

[22] Ger J.O., Rogo K.O. and Sinei S.K., *Cervical Incompetence: Assessment of a Scoring System for Patient Selection for Cervical Cerclage*, Int. J. Gynecol. Obstet. **34**, (1991), 325-329.

[23] Althuisius S.M., Dekker G.A. et al, *Final Results of the Cervical Incompetence Prevention Randomized Cerclage Trial (CIPRACT): Therapeutic Cerclage with Bed Rest Versus Bed Rest Alone*, Am. J. Obstet. Gynecol. **185**, (2001), 1106-12.

[24] Rust O.A., Atlas R.O. et al, *Revisiting the Short cervix Detected by Transvaginal Ultrasound in the Second Trimester: Why Cerclage Therapy May Not Help*, Am. J. Obstet. Gynecol. **185**, (2001), 1098-1105.

[25] Balde M.D., Stolz W., Unteregger B. and Bastert G., *L'echographie Transvaginale. Un Apport dans le Diagnostic de la Beance du Col Uterin*, J. Gynecol Obstet. Biol. Reprod. **17**, (1988), 629-633.

[26] Andersen F.H., Nugent C.E., Wanty S.D. and Hayashi R.H., *Prediction of Risk for Preterm Delivery by Ultrasonographic Measurement of Cervical Length*, Am. J. Obstet. Gynecol. **163**, (1990), 859-867.

[27] Joffe G.M., Del Valle G.O., Izquierdo L.A. et al, *Diagnosis of Cervical Change in Pregnancy by Means of Transvaginal Ultrasonography*, Am. J. Obstet. Gynecol. **166**, (1992), 896-900.

[28] Wong G. and Levine D., *Sonographic Assessment of the Cervix in Pregnancy*, Seminars in Ultrasound, CT, and MRI **19**, (1998), 370-380.

[29] Fox R., James M., Tuohy J. and Wardle P., *Transvaginal Ultrasound in the Management of Women with Suspected Cervical Incompetence*, Br. J. Obstet. Gynaecol. **103**, (1996), 921-924.

[30] Pasquale Rocco B. and Garrone C., *Can Examination of the Cervix Provide Useful Information for Prediction of Cervical Incompetence and Following Preterm Labour ?*, Aust. NZ J. Obstet. Gynaecol. **39**, (1999), 296-300.

[31] Nzeh D.A. and Adetoro O.O., *Sonographic Assessment of the Incompetent Cervix in Pregnancy*, Int. J. Gynecol. Obstet. **37**, (1992), 179-184.

[32] Guzman E.R., Mellon C., Vintzileos A.M. et al, *Longitudinal Assessment of Endocervical Canal Length Between 15 and 24 Weeks' Gestation in Women at Risk for Pregnancy Loss or Preterm Birth*, Obstet. Gynecol. **92**, (1998), 31-37.

[33] Zilianti M., Azuaga A., Calderon F. et al, *Monitoring the Effacement of the Uterine Cervix by Transperineal Sonography: A New Perspective*, J. Ultrasound Med. **14**, (1995), 719-724.

[34] Hoesli I.M., Surbek D.V., Tercanli S. and Holzgreve W., *Three Dimensional Volume Measurement of the Cervix During Pregnancy Compared to Conventional 2D-Sonography*, Int. J. Gynecol. Obstet. **64**, (1999), 115-119.

[35] Hricak H., Chang Y.C.F., Cann C.E. and Parer J.T., *Cervical Incompetence: Preliminary Evaluation with MR Imaging*, Radiology **174**, (1990), 821-826.

[36] Maldjian C., Adam R., Pelosi M. and Pelosi III M., *MRI Appearance of Cervical Incompetence in a Pregnant Patient*, Magnetic Resonance Imaging **17**, (1999), 1399-1402.

[37] Wong G., Levine D. and Ludmir J., *Maternal Postural Challenge as a Functional Test for Cervical Incompetence*, J. Ultrasound Med. **16**, (1997), 169-175.

[38] Guzman E.R., Pisatowski D.M., Vintzileos A.M. et al, *A Comparison of Ultrasonographically Detected Cervical Changes in Response to Transfundal Pressure, Coughing, and Standing in Predicting Cervical Incompetence*, Am. J. Obstet. Gynecol. **177**, (1997), 660-665.

[39] Guzman E.R., Vintzileos A.M., McLean D.A. et al, *The Natural History of a Positive Response to Transfundal Pressure in Women at Risk for Cervical Incompetence*, Am. J. Obstet. Gynecol. **176**, (1997), 634-638.

[40] Zlatnik F.J. and Burmeister L.F., *Interval Evaluation of the Cervix for Predicting Pregnancy Outcome and Diagnosing Cervical Incompetence*, J. Reprod. Med. **38**, (1993), 365-369.

[41] Bateman J.F., Lamandé S.R. and Ramshaw J.A.M., *Collagen Superfamily*, in Extracellular Matrix, Volume **2**, Molecular Components and Interactions, Ed. Comper W.D., OPA, (1996), 21-45.

[42] Gould B.S., *Treatise on collagen*, Academic Press, (1968).

[43] Kokenyesi R., *Collagens and Proteoglycans*, Chapter 2 in The extracellular Matrix of the Uterus, Cervix and Fetal Membranes: Synthesis, Degradation and Hormonal Regulation, Eds Leppert P.C. and Woessner J.F., Perinatology Press, (1991).

[44] Nagase H., Matrix Metalloproteinases 1, 2 and 3: Substrate Specificities and Activation Mechanisms, Chapter 3 in The extracellular Matrix of the Uterus, Cervix and Fetal Membranes: Synthesis, Degradation and Hormonal Regulation, Eds Leppert P.C. and Woessner J.F., Perinatology Press, (1991).

[45] Wight T.N., Heinegård D.K. and Hascall V.C., *Proteoglycans: Structure and Function*, in Chapter 2 of Cell Biology of Extracellular Matrix, 2nd edition, Plenum Press, Ed. Hay E.D., (1991), 45-63.

[46] Hascall T.N., Heinegård D.K. and Wight T.N., *Proteoglycans: Metabolism and Pathology*, in Chapter 5 of Cell Biology of Extracellular Matrix, 2nd edition, Plenum Press, Ed. Hay E.D., (1991), 149-160.

[47] Leppert P.C. and Yu S.H., *Elastin and Collagen in the Human Uterus and Cervix: Biochemical and Histological Correlation*, Chapter 5 in The extracellular Matrix of the Uterus, Cervix and Fetal Membranes: Synthesis, Degradation and Hormonal Regulation, Eds Leppert P.C. and Woessner J.F., Perinatology Press, (1991).

[48] Rorie D.K. and Newton M., *Histologic and Chemical Studies of the Smooth Muscle in the Human Cervix and Uterus*, Am. J. Obstet. Gynecol. **99**, (1967), 466-469.

[49] Danforth D.N., *The Distribution and Functional Significance of the Cervical Musculature*, Am. J. Obstet. Gynecol. **65**, (1954), 1261-1270.

[50] Schwalm H. and Dubrauszky V., *The Structure of the Musculature of the Human Uterus-Muscle and Connective Tissue*, Am. J. Obstet. Gynecol. **94**, (1966), 391-404.

[51] Miramoto T., Arai K., Hirakaa S. and Nagai Y., *Immunohistochemical Studies on Collagen Types in the Uterine Cervix in Pregnant and Non-Pregnant States*, Am. J. Obstet. Gynecol. **156**, (1982), 138-144.

[52] Mecham R.P., Heuser J.E., *The Elastic Fiber*, in Chapter 3 of Cell Biology of Extracellular Matrix, 2nd edition, Plenum Press, Ed. Hay E.D., (1991), 79-87.

[53] Leppert P.C., Keller S., Cerreta J. et al, *The Content in Elastin in the Uterine Cervix*, Arch. Biochem. Biophys. **1**, (1983), 53-58.

[54] Leppert P.C., Yu S.Y., Keller S., Cereta J. and Mandl I., *Decreased Elastic Fibers and Desmosine Content in the Incompetent Cervix*, Am. J. Obstet. Gynecol. **157**, (1987), 1134-39.

[55] Hoeve C.A.J. and Flory P.J., *The Elastic Properties of Elastin*, Biopolymers **13**, (1974), 677-686.

[56] Hay E.D., *Extracellular Matrix*, J. Cell Biol. **91**, (1981), 205s-223s.

[57] Leppert P.C. and Yu S.Y., *Three Dimensional Strutures of Uterine Elastic Fibers: Scanning Electron Microscopic Studies*, Conn. Tissue Res. **27**, (1991), 15-31.

[58] Kleissl H.P., van der Rest M., Naftolin F. et al, *Collagen Changes in the Human Uterine Cervix at Parturition*, Am. J. Obstet. Gynecol. **130**, (1978), 748-753.

[59] Ito A., Mori Y. and Hirakawa S., *Purification and Characterization of an Acid Proteinase from Human Uterine Cervix*, Chem. Pharm. Bull. **27**, (1979), 969-973.

[60] Comper W.D. and Laurent T.C., *Physiological Function of Connective Tissue Polysaccharides*, Physiol. Rev. **58**, (1978), 255-315.

[61] Uldbjerg W., Malmström A., Ekman G., Sheehan J., Ulmsten U. and Wingerup L., *Isolation and Characterization of Dermatan Sulphate Proteoglycan from Human Uterine Cervix*, Biochem. J. **209**, (1983), 497-503.

[62] von Maillot K., Stuhlsatz H.W., Mohanaradhakrishan V. and Greiling H., *Changes in the Glycosaminoglycans Distribution Pattern in the Human Cervix During Pregnancy and Labour*, Am. J. Obstet. Gynecol. **135**, (1979), 503-506.

[63] Rath W., Osmers R., Szeverenyi M., Stuhlsatz H.W. and Kuhn W., *Changes of Glycosaminoglycans in Cervical Connective Tissue During Pregnancy and Parturition*, Chapter 10 in The extracellular Matrix of the Uterus, Cervix and Fetal Membranes: Synthesis, Degradation and Hormonal Regulation, Eds Leppert P.C. and Woessner J.F., Perinatology Press, (1991).

[64] Leppert P.C., *Cervical Softening, Effacement, and Dilatation: A Complex Biochemical Cascade*, Journal of Maternal-Fetal Medicine **1**, (1992), 213-223.

[65] Ekman G., Almström H., Granström L., Malmström A., Norman M. and Woessner Jr J.F., *Connective Tissue in Human Cervical Ripening*, Chapter 8 in The extracellular Matrix of the Uterus, Cervix and Fetal Membranes: Synthesis, Degradation and Hormonal Regulation, Eds Leppert P.C. and Woessner J.F., Perinatology Press, (1991).

[66] Kitamura K., Ito A., Mori Y. and Hirakawa S., *Glycosaminoglycans of Human Uterine Cervix: Heparan Sulfate Increases with Reference to Cervical Ripening*, Biochem. Med. **23**, (1980), 159-166.

[67] Cabrol D., Breton M., Berrou E., Visser A., Sureau C. and Picard J., *Variations in the Distribution of Glycosaminoglycans in the Uterine Cervix of the Pregnant Woman*, Eur. J. Gynecol. Reprod. Biol. **10**, (1980), 281-287.

[68] Shimizu T., *Correlation of Human Cervical Ripening and Glyconjugates (Glycosaminoglycans and Glycoproteins)*, Acta Obstet. Gynaecol. Jpn **32**, (1980), 1967-1976.

[69] Conrad J.T., Tokarz R.D. and Williford J.F., *Anatomic Site and Stretch Modulus in the Human Cervix*, in Dilatation of the Uterine Cervix, Ed. Naftolin F. and Stubblefield P.G., Raven Press, New York, (1980), 255-264.

[70] Petersen L.K., Oxlund H., Uldbjerg N. and Forman A., *In Vitro Analysis of Muscular Contractile Ability and Passive Biomechanical Properties of Uterine Cervical Samples From Nonpregnant Women*, Obstet. Gynecol. **77**, (1991), 772-776.

[71] Aspden R.M., *The Theory of Fibre-Reinforced Composite Materials Applied to Changes in the Mechanical Properties of the Cervix During Pregnancy*, J. Theor. Biol. **130**, (1988), 213-221.

[72] Aspden R.M., *Collagen Organisation in the Cervix and its Relation to Mechanical Function*, Coll. Relat. Res. **8**, (1988), 103-12.

[73] Yu S.H. and Leppert P.C., *The Collagenous Tissues of the Cervix During Pregnancy and Delivery*, Chapter 6 in The extracellular Matrix of the Uterus, Cervix and Fetal Membranes: Synthesis, Degradation and Hormonal Regulation, Eds Leppert P.C. and Woessner J.F., Perinatology Press, (1991).

[74] Shimizu T., Endo M. and Yosizawa Z., *Glycoconjugates (Glycosaminoglycans and Glycoproteins) and Glycogen in the Human Cervix Uteri*, Tohoku J. Exp. Med. **131**, (1980), 289-299.

[75] Boyce M.C., Arruda E.M., *Constitutive Models of Rubber Elasticity: A Review*, Rubber Chem. Tech. **73**, (2000), 504-523.

[76] Roeder B.A., Kobini K., Sturgis J.E., Robinson J.P. and Voytik-Harbin S.L., *Micromechanics of Extracellular Matrix: Three-Dimensional Microstructure under Load*, in Proceedings: 2001 ASME International Mechanical Engineering Congress and Exposition, (2001).

[77] Yannas I.V., Comninou M., *Dependence of Stress-Strain Nonlinearity of Connective Tissues on the Geometry of Collagen Fibers*, J. Biomechanics **9**, (1976), 427-433.

[78] Treloar L.R.G., *The Physics of Rubber Elasticity*, Oxford University Press, (1975).

[79] Kuhn W. and Grühn F., *Beziehungen zwischen elastischen Konstanten und Dehnungsdoppelbrechung hochelastischer Stoffe*, Kolloid-Z. **101**, (1942), 248-271.

[80] Arruda E.M., Boyce M.C., *A Three-Dimensional Constitutive Model for the Large Stretch Behavior of Rubber Elastic Materials*, J. Mech. Phys. Solids **41**, (1993), 389-412.

[81] Socrate S., Boyce M.C., *Large Strain Constitutive Behavior of Articular Cartilage: An Investigation of Collagen-Proteoglycans Interactions*, in Proceedings: Plasticity

'02, Plasticity, Damage and Fracture at Macro, Micro and Nano Scales, Ed. Khan A.S., Lopez Pamies O., (2002), 156-161.

[82] Bischoff J.E., Arruda E.M., *Finite Element Modeling of Human Skin Using an Isotropic, Nonlinear Elastic Constitutive Model*, J. Biomechanics **33**, (2002), 645-652.

[83] Basser P.J., Schneiderman R, Bank R.A., Wachtel E. and Maroudas A., *Mechanical Properties of the Collagen Network in Human Articular Cartilage as Measured by Osmotic Stress Technique*, Archives of Biochemistry and Biophysics **351**, (1998), 207-219.

[84] Maroudas A., Evans H., Almeida L., Ann. Rheum. Dis. **32**, (1973), 1-9.

[85] Mow V.C., Lai W.M., *Mechanics of Animal Joints*, Ann. Rev. Fluid Mech. **11**, (1979), 247-288.

[86] Broom N.D., Poole C.A., *Articular Cartilage Collagen and Proteoglycans*, Arthritis and Rheumatism **26**, (1983), 1111-19.

[87] Eisenberg S.R., Grodzinsky A.J., *Swelling of Articular cartilage and Other Connective Tissues: Electromechanical Forces*, J. Orthop. Res. **3**, (1985), 148-159.

[88] Khalsa S., Eisenberg S.R., *Compressive Behavior of Articular Cartilage is not Completely Explained by Proteoglycan Osmotic Pressure*, J. Biomechanics **30**, (1997), 589-594.

[89] Yu S.Y., Tozzi C.A., Babiarz J., Leppert P.C., *Collagen Changes in Rat Cervix in Pregnancy. Polarized Light Microscopic and Electron Microscopic Studies*, Proc. Soc. Exp. Biol. Med. **209**, (1995), 360-368.

[90] Buschmann M.D., Grodzinsky A.J., *A Molecular Model of Proteoglycan-Associated Electrostatic Forces in Cartilage Mechanics*, J. Biomech. Eng. **117**, (1995), 179-191.

[91] Kovach I.S., *A Molecular Theory of Cartilage Viscoelasticity*, Biophysical Chemistry **59**, (1996), 61-73.

[92] Boyce M.C., Socrate S., Llana P.G., *Constitutive Model for the Finite Deformation Stress-Strain Behavior of Poly(Ethylene Terephtalate) Above the Glass Transition*, Polymer **41**, (2000), 2183-2201.

[93] Maroudas A., *Physico-Chemical Properties of Articular Cartilage*, in Adult Articular Cartilage, Ed. Freeman M.A.R., 2nd edition, Pitman, Tunbridge Wells, England, (1979), 215-290.

[94] Ehrlich S., Wolff N., Schneiderman R., Maroudas A., Parker K.H. and Winlova C.P., *The Osmotic Pressure of Chondroitin Sulphate Solutions: Experimental Measurements and Theoretical Analysis*, Biorheology **35**, (1998), 383-397.

[95] Katchalsky A., Alexandrowicz Z. and Kedem O., *Chemical Physics of Ionic Solutions*, Wiley, New York, 1964.

[96] Maroudas A. and Bannon C., *Measurements of Swelling Pressure in Cartilage and Comparison with the Osmotic Pressure of Constituent Proteoglycans*, Biorheology **18**, (1981), 619-632.

[97] Jin M. and Grodzinsky A.J., *Effect of Electrostatic Interactions between Glycosaminoglycans on the Shear Stiffness of Cartilage: A Molecular Model and Experiments*, Macromolecules **34**, (2001), 8330-39.

[98] Darcy H., *Les Fontaines Publiques de la Ville de Dijon*, Dalmont, Paris, 1856.